GRADUATE AERONAUTICAL LABORATORIES
CALIFORNIA INSTITUTE OF TECHNOLOGY

Mixing and Isosurface Geometry in Turbulent Transverse Jets

Jerry Wei-Jen Shan

5 January 2001

Firestone Flight Sciences Laboratory

Guggenheim Aeronautical Laboratory

Karman Laboratory of Fluid Mechanics and Jet Propulsion

Pasadena

Mixing and Isosurface Geometry in Turbulent Transverse Jets

Jerry Wei-Jen Shan

Graduate Aeronautical Laboratories
California Institute of Technology
Pasadena, California 91125

5 January 2001

Thesis submitted in partial fulfillment of requirements for the degree of
Doctor of Philosophy in Aeronautics

Abstract

Mixing and the geometry of jet-fluid-concentration level sets in turbulent transverse jets were experimentally studied. Jet-fluid concentration fields were measured with laser-induced fluorescence and digital imaging techniques for transverse jets in the jet Reynolds number range $1.0 \times 10^3 \leq Re_j \leq 20 \times 10^3$. The scalar field is assessed in terms of classical measures, such as two-dimensional power spectra, as well as probability-density functions (PDFs). Enhanced scalar mixing with increasing Reynolds number is found in the evolution of PDFs of jet-fluid concentration. In the far field of the transverse jet, the scalar PDF evolves from a monotonically-decreasing function to a strongly-peaked distribution with increasing Reynolds number. Turbulent mixing is found to be flow dependent, based on differences between PDFs of scalar fields in transverse jets and axisymmetric, turbulent jets. The distribution of scalar increments is studied for separations of varying distance and direction using a novel technique for whole-field measurement of scalar increments. Probability-density functions of scalar increments are found to trend toward exponential-tailed distributions with decreasing separation distances. The scalar field is anisotropic with decreasing scale, as seen in the two-dimensional power spectra, directional scalar microscales, and in directional PDFs of scalar increments.

The geometric complexity of level-sets (iso-concentration contours) in turbulent mixing is assessed within the framework of fractal geometry. Generalized coverage statistics are introduced for anisotropic, non-self-similar geometries. This generalized coverage counting involves covering with parallelepipeds of varying size and aspect ratio. A scale-dependent measure, β, of the anisotropy of a set is also introduced. It is shown that β transforms the coverage count, $N(\lambda_1, \lambda_2)$, to isotropy through a scale-dependent normalization of the coordinates. Level sets of jet-fluid concentration in the transverse jet are found to be anisotropic at both large and small scales. The small-scale anisotropy is attributed to vertically-oriented extensional strain caused by a counter-rotating vortex pair, and the large-scale anisotropy is associated with the horizontally-elongated shape of the cross-section of the transverse jet. For the special case of isotropic box-counting, the scale-dependent coverage dimension is found to vary from unity, at the smallest length scales, to 2, at the largest length scales, indicating that the isosurfaces produced by turbulent mixing are more complex than can be described by power-law fractals.

Acknowledgments

I thank my advisor, Prof. Paul Dimotakis, for his help and encouragement. I am deeply grateful to him for his many creative suggestions, and for instilling some of his own passion for science and desire for excellence. He and his wife, Susan, together created a stimulating and supportive environment to work in.

I am also indebted to the other members of my committee, Profs. Morteza Gharib, Hans Hornung, and Anthony Leonard for their careful reading of this thesis. Their suggestions and comments improved the work substantially.

The assistance of Dr. Dan Lang with digital imaging, electronics, and computer matters was invaluable. This work would not have been possible without his genius. The assistance of Santiago Lombeyda of CACR with three-dimensional visualization is gratefully acknowledged. Pavel Svitek and Earl Dahl also gave valuable technical assistance, and made helped make the work fun.

I thank my friends and colleagues in GALCIT, especially Jimmy Fung and Drs. Han Park, Paul Krueger, David Jeon, and Michael Ol, for making my studies rewarding and enjoyable. I also thank Dr. Peter Park, Isaac Chenchiah, Smith Nielsen, Jim Harrington, the Kuas, the Copelands, and the rest of my friends in CCF Grad Group, for enriching my life with their faith and encouragement. And I thank Lucia Kuhns for her friendship and love.

This thesis is dedicated to my parents for their constant love and support.

The research described here was funded by the Air Force Office of Scientific Research, and a National Defense Science and Engineering Graduate Fellowship. Their support is gratefully acknowledged.

Contents

CHAPTER 1

Introduction

The turbulent jet discharging into a crossflow, or transverse jet, is a turbulent free-shear flow of both fundamental significance as well as environmental and technological application. Thermal plumes generated near ground level by volcanoes, thunderstorms, or forest fires can often rise to heights in the atmosphere where significant crossflow exists. Plumes emitted from smokestacks into a crosswind are perhaps the most familiar instances of transverse jets. However, transverse jets also arise in situations as diverse as effluent discharge into rivers from sewage treatment plants, VTOL/STOL aerodynamics, steering jets, blade-and-endwall cooling in gas-turbines, and potentially, fuel injection in high-speed airbreathing propulsion devices, such as SCRAMJETS (Mathur *et al.* 1999). Buoyancy is important to varying degree in many of the transverse jets discussed; however, buoyancy-driven transverse jets are similar in structure, and appear to share many characteristics with, momentum-driven transverse jets.

Early studies of transverse jets focused on jet trajectories, mean velocity fields, and cross-sectional shapes (Keffer and Baines 1963, Kamotani and Greber 1972, Chassaing *et al.* 1974). The existence of a persistent counter-rotating vortex pair in the far field of the transverse jet was noted in numerous experiments (Keffer and Baines 1963, Fearn and Weston 1974). Broadwell and Breidenthal (1984) modeled the counter-rotating vortex pair as a global consequence of the normal momentum imparted by the jet to the freestream. Karagozian (1986) studied the vorticity associated with a transverse jet, and modeled jet trajectories, mean vortex-pair strength, and reaction lengths. Periodic motion in the wake of the transverse jet was noted by Gordier (1959), McAllister (1968), and Reilly (1968). Characteristic Strouhal frequencies were measured by McMahon *et al.* (1971) and Moussa *et al.* (1977). Vortices in the wake of a turbulent jet issuing transversely to a freestream

were first visualized by Kuzo and Roshko (1984). Fric and Roshko (1994) studied the origin and formation of wake vortices, and their work generated renewed interest in the structure and dynamics of vorticity in transverse jets (Kelso and Smits 1995, Morton and Ibbetson 1996, Kelso *et al.* 1996). Kuzo (1996) reported that, under certain conditions, the mean flow state in the far field of the transverse jet is not a symmetric vortex pair, but unsteady and asymmetric with possible tertiary vortices. A comprehensive review of jet-in-crossflow research was presented by Margason (1993).

Mean scalar fields in transverse jets have been experimentally measured by Andreopoulos and Rodi (1984) and Niederhaus *et al.* (1997). Large-eddy simulations were conducted by Yuan *et al.* (1999), among others. Three-dimensional vortex elements were used by Cortelezzi and Karagozian (2001) to compute the formation of the counter-rotating vortex pair in the near field of transverse jets. The vortex interaction region, mean trajectories and concentration decay, and overall structural features of mixing were studied by Smith and Mungal (1998). Yet, as noted by Niederhaus *et al.* (1997), "...the vast majority of the published work [on transverse jets] has focused on issues concerning the velocity field. Remarkably, there is a scarcity of research directed toward scalar transport or mixing, even though the majority of applications require knowledge of the transport of either mass or heat."

The geometry of the isosurfaces of the scalar fields in turbulence is important for many applications. In the case of non-premixed combustion, for instance, the rate of chemical reaction depends on the area of the instantaneous stoichiometric surface, an isosurface of fuel-to-air ratio. The isosurfaces produced by turbulent mixing have long been proposed to be candidates for description by a fractal geometry (Mandelbrot 1975). A generalized fractal geometry that is allowed to depend on the scale of observation was introduced by Takayasu (1982). Independently, Miller and Dimotakis (1991), on the basis of their experiments, and Dimotakis (1991), on the basis of scaling arguments, introduced a scale-dependent geometry in the context of fluid turbulence. Dimotakis (1991) gave scaling arguments regarding the dimensional inconsistency of constant (power-law) fractal dimensions in nature. Catrakis and Dimotakis (1996) also found scale-dependent coverage dimensions, $D_2(\lambda)$), *i.e.*, the geometric complexity of the isosurfaces in turbulent axisymmetric

jets is greater than can be described by a power-law fractal. They also established a connection between the scale-dependent fractal geometry, and the distribution of spatial (largest empty-box) scales in the flow.

Experiments are described here on the mixing and isosurface geometry of transverse jets as a function of Reynolds number. Details of the experiment and imaging procedure, and sample image data, are given in Ch. 2. A local, circulation-based Reynolds number is introduced, and viscous-dissipation and scalar-diffusion scales are estimated. In Ch. 3, classical measures of turbulent jets, such as trajectories, concentration decay, and power spectra, are presented for the transverse jet. Chapters 4 and 5 describe the scalar field, and scalar-difference field, respectively. The scalar field of the transverse jet, and Reynolds-number effects on turbulent mixing, is described in Ch. 4 in terms of probability-density functions (PDFs) of jet-fluid concentration. Comparison is made between mixing in transverse jets, and turbulent jets discharging into a quiescent reservoir. In Ch. 5, a technique for whole-field measurements of scalar increments is introduced, and PDFs of scalar increments are computed in the far field of the transverse jet. Whole-field measurements are made of the PDFs of scalar concentration differences,

$$\Delta_{\mathbf{r}} C \equiv C(\mathbf{x}+\mathbf{r},t) - C(\mathbf{x},t)\,, \tag{1.1}$$

as a function of the separation distance, $\mathbf{r}$, and jet-exit Reynolds number. Direction-dependent scalar microscales are considered, and the scalar-field anisotropy is quantified as a function of Reynolds number. An explanation for the observed anisotropy of the scalar field in transverse jets is proposed.

The geometry of level sets of jet-fluid concentration in the transverse jet is also assessed. Chapter 6 reviews fractal geometry, and introduces a generalization of fractal geometry that is applicable to anisotropic sets. The ideas involved in this generalization are illustrated using two simple examples of a rectangular perimeter, and a Sierpinski carpet. A scale-dependent measure of anisotropy is introduced as the normalization required to transform the coverage count to isotropy. In Ch. 7, the generalized coverage count, and scale-dependent anisotropy, of transverse-jet isosurfaces, are computed for varying concentration thresholds and two different Reynolds numbers. The special case of isotropic (box-counting) coverage statistics

is considered for the transverse-jet data, and comparisons are made to previous investigations of turbulent, axisymmetric jets.

CHAPTER 2

Experiments and imaging technique

This chapter details experiments on turbulent mixing and the isosurface geometry of jets in crossflow (transverse jets). The transverse-jet facility in the GALCIT Free-surface Water Tunnel (FSWT) is described, along with laser-induced fluorescence (LIF) and digital-imaging techniques that enabled quantitative measurements of jet-fluid concentration fields for liquid-phase transverse jets. Concentration measurements were made in planes perpendicular and parallel to the freestream, for jet Reynolds numbers $1.0 \times 10^3 \leq Re_\mathrm{j} \equiv d_\mathrm{j} U_\mathrm{j}/\nu \leq 20 \times 10^3$, where d_j is the jet-nozzle diameter, U_j is the exit velocity of the jet, and ν is the kinematic viscosity. The calibration procedure used to normalize LIF images into scalar concentration data is described. Examples of scalar concentration fields are given for two different jet-to-freestream velocity ratios, and the differences are discussed. Three-dimensional visualizations of the jet-fluid-concentration isosurface for low Reynolds numbers are shown. An assessment is made of the local, circulation-based Reynolds number, $Re_\Gamma \equiv \Gamma/\nu$, as a function of the jet-exit Reynolds number $Re_\mathrm{j} \equiv d_\mathrm{j} U_\mathrm{j}/\nu$. The Kolmogorov and scalar diffusion scales for the flow conditions are estimated and compared to the imaging resolution.

2.1 Experimental facility

Experiments on turbulent mixing and isosurface geometry in liquid-phase transverse jets were conducted in the GALCIT Free Surface Water Tunnel (FSWT) using laser-induced fluorescence (LIF) and digital-imaging techniques. The FSWT is a closed-circuit facility with a 20 in (0.508 m) wide by 30 in (0.762 m) deep test section. For these experiments, the FSWT was operated as a water channel with a square cross-section by maintaining the water level at a depth of 20 in (0.508 m) and fitting a surface plate flush to the top of the water surface (Fig. 2.1). Jet flow transverse to the freestream was established by air-pressurizing an inverted, liquid-filled plenum and injecting downward into the test section, through a nozzle in the surface plate. Water in the plenum was seeded with a fluorescent dye, rhodamine-6G chloride, at molar concentrations between 1.4×10^{-6} and 1.4×10^{-5}. Tunnel water, which was left unseeded, did not fluoresce under laser illumination. The non-dimensional ratio of kinematic viscosity, ν, to scalar diffusivity, $\mathcal{D}$, is the Schmidt number, $Sc \equiv \nu/\mathcal{D}$. Rhodamine-6G, dissolved in water, is estimated to have a Schmidt number $Sc \simeq 8.4 \times 10^3$ (Axelrod *et al.* 1976, Walker 1987). At this high Schmidt number, the scalar diffuses much more slowly than the vorticity, and the dye, once it enters a vortex, would continue to mark the core of the vortices. The scalar field for $Sc > 1$ may have length scales smaller than the smallest length scales of the vorticity field, as discussed in Sec. 2.5.

The laser-excitation and fluorescence-emission peaks of rhodamine-6G, when dissolved in water, are at $\lambda = 526\,\text{nm}$ and $\lambda = 555\,\text{nm}$, respectively (Pringsheim 1949). The output from a frequency-doubled, Q-switched Nd:Yag laser (Continuum YG661) was passed through a series of cylindrical lenses, which expanded the beam into a sheet, while focusing it to a waist at the center of the imaged field of view. The thickness of the laser sheet was less than 1 mm throughout the field of view of the camera. Figure 2.1 shows a schematic of the experimental facility and imaging configuration for acquiring streamwise sections of the scalar-concentration field on the centerline of the transverse jet. Transverse slices of the jet scalar field were also measured at a downstream location $x/d_\text{j} = 50$, where $d_\text{j} = 7.62\,\text{mm}$ is the jet diameter, by inserting an elliptically-shaped, flat mirror in the water at 45° to the freestream. The CCD camera was mounted on top of the water channel, and looked

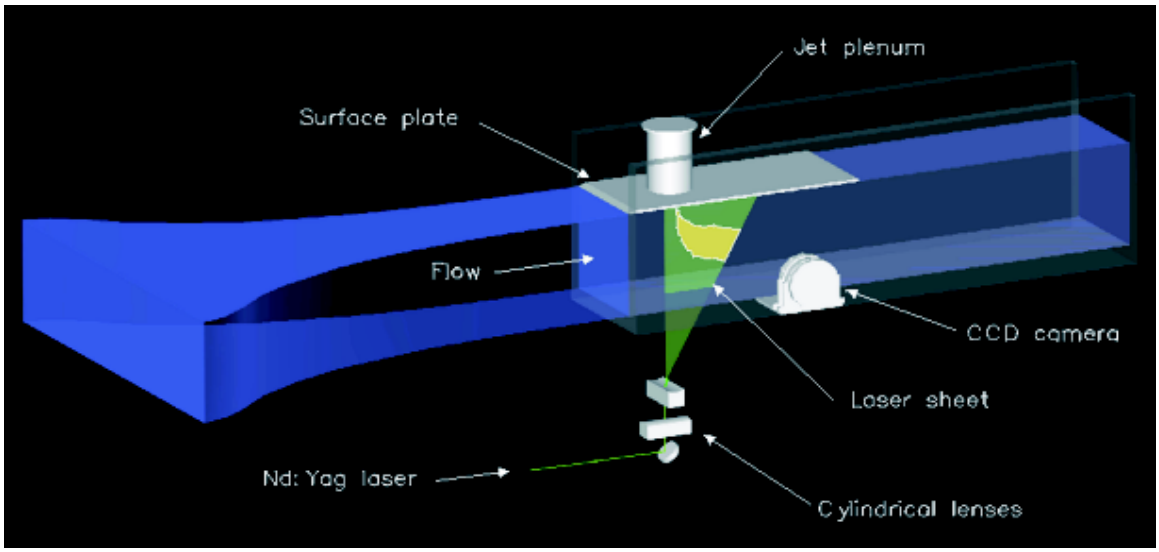

FIG. 2.1 Experimental facility and imaging configuration for acquiring streamwise sections of transverse jet.

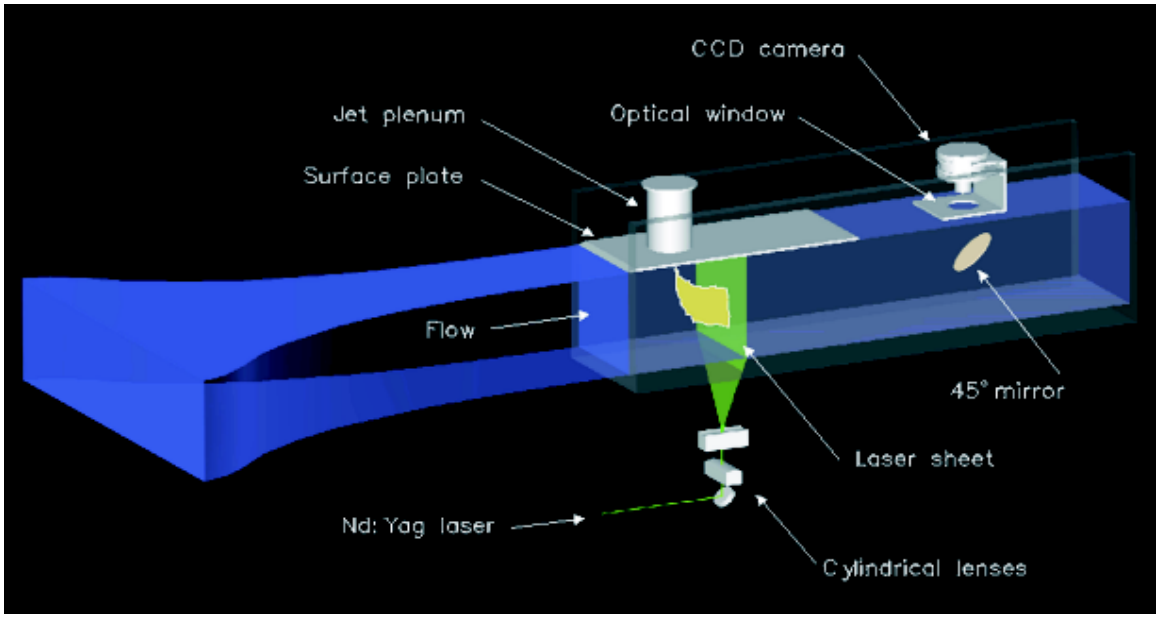

FIG. 2.2 Experimental facility and imaging configuration for acquiring transverse sections of transverse jet, measured at downstream location $x/d = 50$.

down on the mirror through an optical window at the water surface (Fig. 2.2).

2.2 Jet-fluid concentration measurements

LIF images of the scalar (jet-fluid) concentration field were recorded at 10 frames/second with a custom, 12-bit/pixel, (1024×1024)-pixel digital-imaging system, dubbed the "Cassini camera." The camera, designed and built by D. Lang, in collaboration with S. A. Collins and M. Wadsworth of the Jet Propulsion Laboratory, utilizes a low-noise, high dynamic-range CCD sensor developed for NASA's Cassini spacecraft. Contiguous time-sequences of 254 images were recorded for streamwise sections of the jet, and 508 images for transverse sections. All data were recorded in a darkened laboratory to minimize noise from ambient light. A Kodak #21 optical low-pass filter was used to block residual (excitation) laser light. The jet-fluid concentration field, referenced to a known concentration, was computed by calibrating the raw fluorescence image data with 32 ensemble-averaged, uniform-concentration images and 32 ensemble-averaged, background-illumination images,

$$\frac{c(x_1, x_2, t)}{c_{\text{ref}}} \;=\; \frac{I_{\text{raw}}(x_1, x_2, t) - \langle\, I_{\text{back}}(x_1, x_2) \,\rangle}{\langle\, I_{\text{ref}}(x_1, x_2) \,\rangle - \langle\, I_{\text{back}}(x_1, x_2) \,\rangle} \;\; . \tag{2.1a}$$

For streamwise (vertical, plane-of-symmetry) slices of the transverse jet, the coordinates x_1, x_2 denote the streamwise, x, and vertical, y, directions, respectively (Figs. 2.3 - 2.6). For transverse slices of the transverse jet, x_1, x_2 denote the horizontal (spanwise), z, and vertical, y, directions, respectively (Figs. 2.7 - 2.10). The origin of the coordinate system is taken to be the jet-nozzle exit in all cases. $X - Y - Z$ form a right-handed coordinate system, with x pointing in the direction of jet injection (downward), y aligned with the freestream flow, and z directed in the spanwise direction.

The background images, $I_{\text{back}}(x_1, x_2)$, were recorded shortly before each run, with the laser firing and the optical low-pass filter on the camera lens, but without the (fluorescent-dye seeded) jet running. The reference images, $I_{\text{ref}}(x_1, x_2)$, were recorded after each run by immersing a transparent Lucite container filled with well-mixed fluorescent dye of known concentration, c_{ref}, in the test section. This procedure provides a pixel-by-pixel calibration that normalizes the collective effects of CCD-pixel sensitivity variation, laser-illumination nonuniformity, and the imaging-system optical transfer function. The imaged jet-fluid concentration was

then referenced to the jet-plenum dye concentration, c_0, by scaling all values with $c_{\rm ref}/c_0$ to yield the normalized jet-fluid-concentration scalar values, C, *i.e.*,

$$0.0 \;\leq\; C(x_1, x_2, t) \equiv \frac{c(x_1, x_2, t)}{c_0} = \frac{c(x_1, x_2, t)}{c_{\rm ref}} \, \frac{c_{\rm ref}}{c_0} \;\leq\; 1.0 \;\; . \tag{2.1b}$$

The jet-plenum dye concentration, c_0, and the reference concentration, $c_{\rm ref}$, are known when the dye solutions are mixed. For streamwise sections of the jet, shot-to-shot variations in the output power of the pulsed laser were normalized by measuring the fluorescence-intensity fluctuations at the jet-exit (c_0 is constant during the course of an experiment, and the jet exit is visible in the streamwise images). For transverse sections, the jet exit is not visible in the images, so a fiber-optic probe was used to collect a small fraction of the laser output and direct the illumination to a test tube filled with a rhodamine-6G solution. The intensity fluctuations of this fluorescent sample were imaged in an unused corner of the CCD array, and shot-to-shot laser-power variations were normalized with this measurement.

2.3 Jet Reynolds numbers and velocity ratios

The experiments were conducted at jet Reynolds numbers of $Re_{\rm j} \equiv U_{\rm j}\, d_{\rm j}/\nu =$ 1.0, 2.0, 5.0, 10, and 20×10^3. $U_{\rm j}$ is the mean jet-exit velocity, $d_{\rm j}$ is the jet-nozzle diameter, and ν is the kinematic viscosity. The jet-to-freestream velocity ratio, $V_{\rm r} \equiv U_{\rm j}/U_\infty$, was 10.1. Examples of the calibrated and normalized scalar-field data for streamwise sections of the transverse jet are shown in Fig. 2.3 for $Re_{\rm j} = 1.0 \times 10^3$ and Fig. 2.4 for $Re_{\rm j} = 10 \times 10^3$.

Examples of transverse sections of the jet at the downstream location $x/d_{\rm j} = 50$ are shown in Figs. 2.7 and 2.8. The images are of the $V_{\rm r} \simeq 10.1$ jet for $Re_{\rm j} = 1.0 \times 10^3$ and 10×10^3.

For comparison, examples of streamwise slices (plane of symmetry) of the transverse jet for $V_{\rm r} \simeq 32.3$ are depicted in Figs. 2.5 and 2.6. Thin vertical "fingers" of dye are seen to extend from the body of the jet toward the wall through which the jet was injected. Jet fluid, in the form of these "fingers", is also seen in transverse

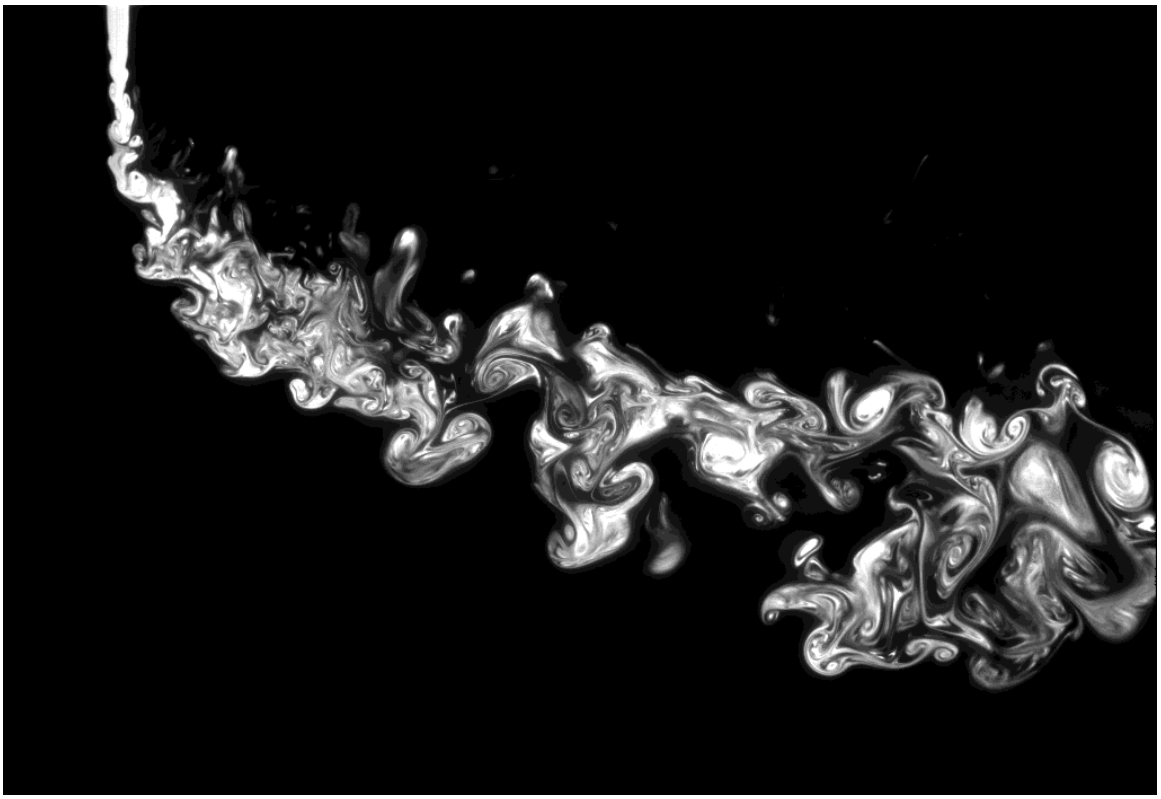

FIG. 2.3 Jet-fluid concentration in a streamwise slice (plane of symmetry) of the transverse jet for $Re_{\rm j} = 1.0 \times 10^3$. $V_{\rm r} \simeq 10.1$. Image data scaled by $x^{1/2}$ to compensate for downstream decay (for display purposes only).

sections of the high-velocity-ratio jet (Figs. 2.9 and 2.10). This suggests that it may be possible for jet shear-layer vorticity to be transported into the wake of the transverse jet at high velocity ratios. Jet fluid is not seen in the wake region of the transverse jet for $V_{\rm r} \leq 10$ (Fric and Roshko 1994).

The field of view spans 53×53 jet-exit diameters for the streamwise sections displayed in Figs. 2.3 and 2.4. The pixel resolution is $\lambda_{\rm p} = 392\,\mu$m, and the jet diameter was $d_{\rm j} = 19\lambda_{\rm p}$. The field of view for the transverse sections of the jet (Figs. 2.7 and 2.8) is 31×31 jet-exit diameters at a pixel resolution of $\lambda_{\rm p} = 230\,\mu$m. In the transverse views, $d_{\rm j} = 33\lambda_{\rm p}$.

The high-velocity-ratio images (Figs. 2.5, 2.6, 2.9, 2.10) are provided for comparison with the low-velocity ratio cases. All subsequent analysis is performed on $V_{\rm r} \simeq 10.1$ jets (Figs. 2.3, 2.4, 2.7, 2.8).

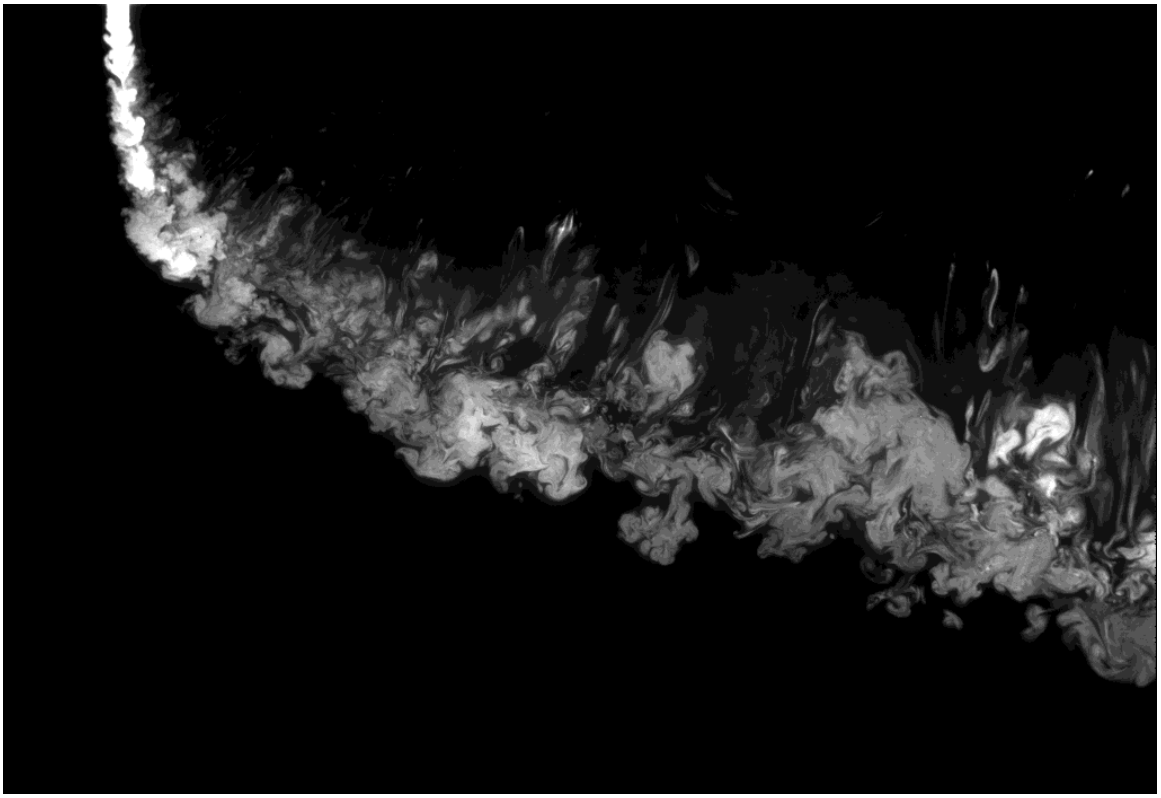

FIG. 2.4 Jet-fluid concentration in a streamwise slice (plane of symmetry) of the transverse jet for $Re_{\rm j} = 10 \times 10^3$. $V_{\rm r} \simeq 10.1$. Image data scaled by $x^{1/2}$ to compensate for downstream decay (for display purposes only).

2.4 Jet-fluid-concentration level set

From the measured scalar field, $C(\mathbf{x}, t)$, level sets of jet-fluid-concentration, $C(\mathbf{x}, t) = C_{\rm iso}$, can be extracted. These isolines (in two-dimensions), or isosurfaces (in three-dimensions), are geometrically complex, and important to chemical reaction rates, and for fluid mixing on the molecular scale (Ch. 1). Experimentally-measured data, consisting of time sequences of two-dimensional images, may be assembled into three-dimensional space-time measurements of the scalar field. Under certain conditions, this space-time measurement is an approximation of the three-dimensional spatial structure of the scalar field. These assumptions, and the details of the three-dimensional visualization, are discussed in Appendix B.

A space-time visualization of the jet-fluid concentration level set is shown in Fig. 2.11 for the $Re_{\rm j} \simeq 1.0 \times 10^3$, $V_{\rm r} = 10.1$, transverse jet. The isosurface visualiza-

FIG. 2.5 Jet-fluid concentration in a streamwise slice of the jet for $Re_j = 1.0 \times 10^3$ and $V_r \simeq 32.3$ (*cf.* Fig. 2.3). Image data scaled by $x^{1/2}$ to compensate for downstream decay (for display purposes only).

tion were computed in collaboration with Santiago Lombeyda of Caltech's CACR. An isosurface of jet-fluid concentration is highlighted by choosing a small range of jet-fluid concentrations to be reflecting in the volume visualization. The structure of the transverse jet is seen to be dominated by kidney-shaped, counter-rotating vortices in Fig. 2.11. At this low Reynolds number, we find two large, counter-rotating vortices, and a smaller, tertiary vortex. The rotation of this tertiary vortex is ev-

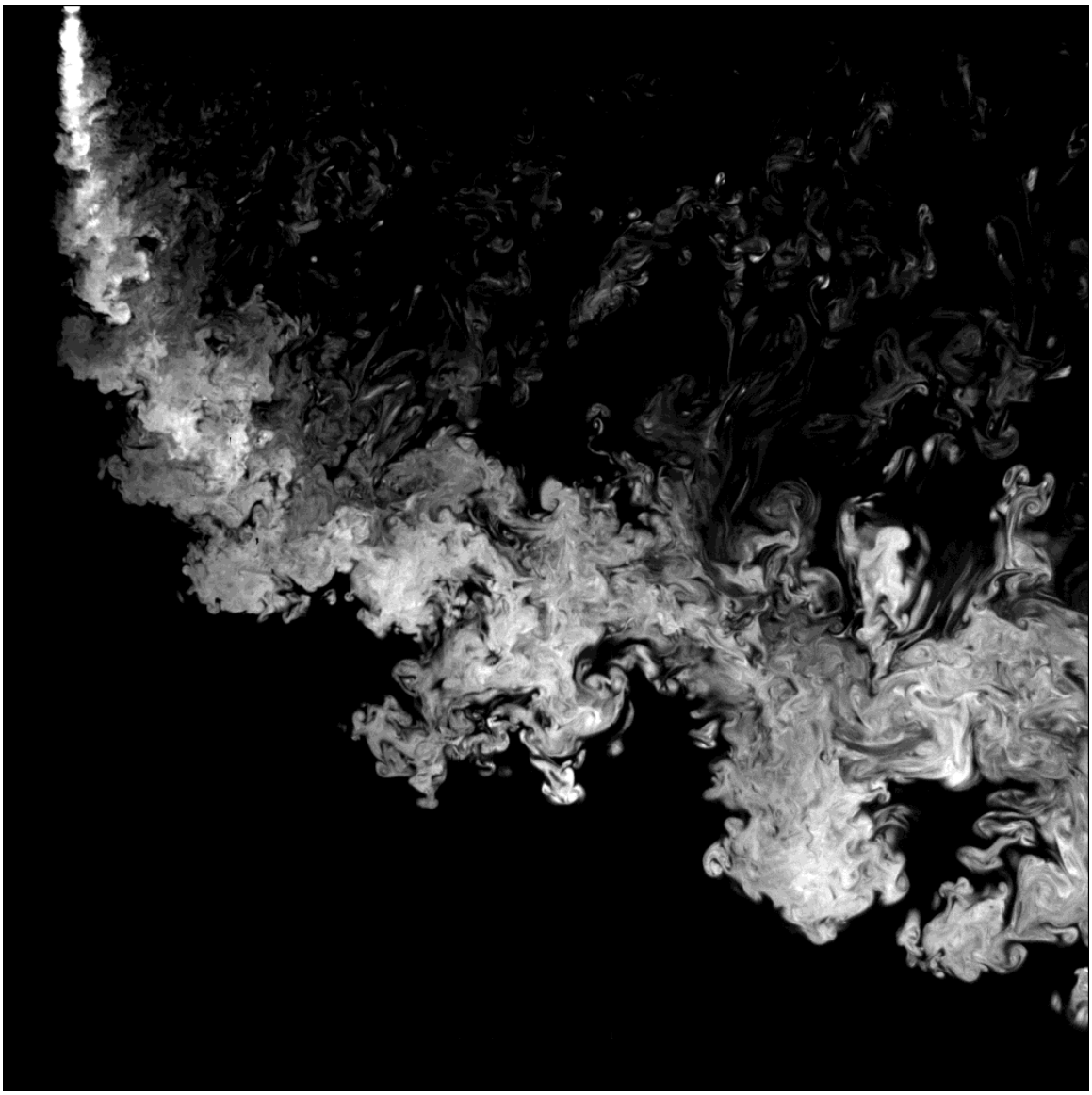

FIG. 2.6 Jet-fluid concentration in a streamwise slice of the jet for $Re_{\rm j} = 10 \times 10^3$ and $V_{\rm r} \simeq 32.3$ (*cf.* Fig. 2.4). Image data scaled by $x^{1/2}$ to compensate for downstream decay (for display purposes only).

ident in the filaments of jet-fluid that wrap around it. "Fingers" of dye are seen to reach up from middle of the counter-rotating vortex pair, and wrap around the tertiary vortex. The structure and topology of the jet appears to be fairly steady during the course of one experiment.

A visualization of the three-dimensional level set of jet-fluid concentration is

FIG. 2.7 Jet-fluid concentration in a transverse slice of the jet at downstream location $x/d_{\mathrm{j}} = 50$. $V_{\mathrm{r}} \simeq 10.1$ and $Re_{\mathrm{j}} = 1.0 \times 10^3$.

also depicted in Fig. 2.12 at a higher Reynolds number. In comparison to the $Re_{\mathrm{j}} \simeq 1.0 \times 10^3$ transverse jet, the isosurface at $Re_{\mathrm{j}} \simeq 2.0 \times 10^3$ is symmetric, or nearly so. The structure of the transverse jet is again seen to be dominated by a kidney-shaped, counter-rotating vortex pair. "Fingers", or small-scale streaks extend vertically from the main body of the jet. No evidence of a tertiary vortex is seen in the scalar scalar. We note that temporal sampling rate of the Cassini camera does not enable resolution down to the diffusion scales in the streamwise (freestream) direction at

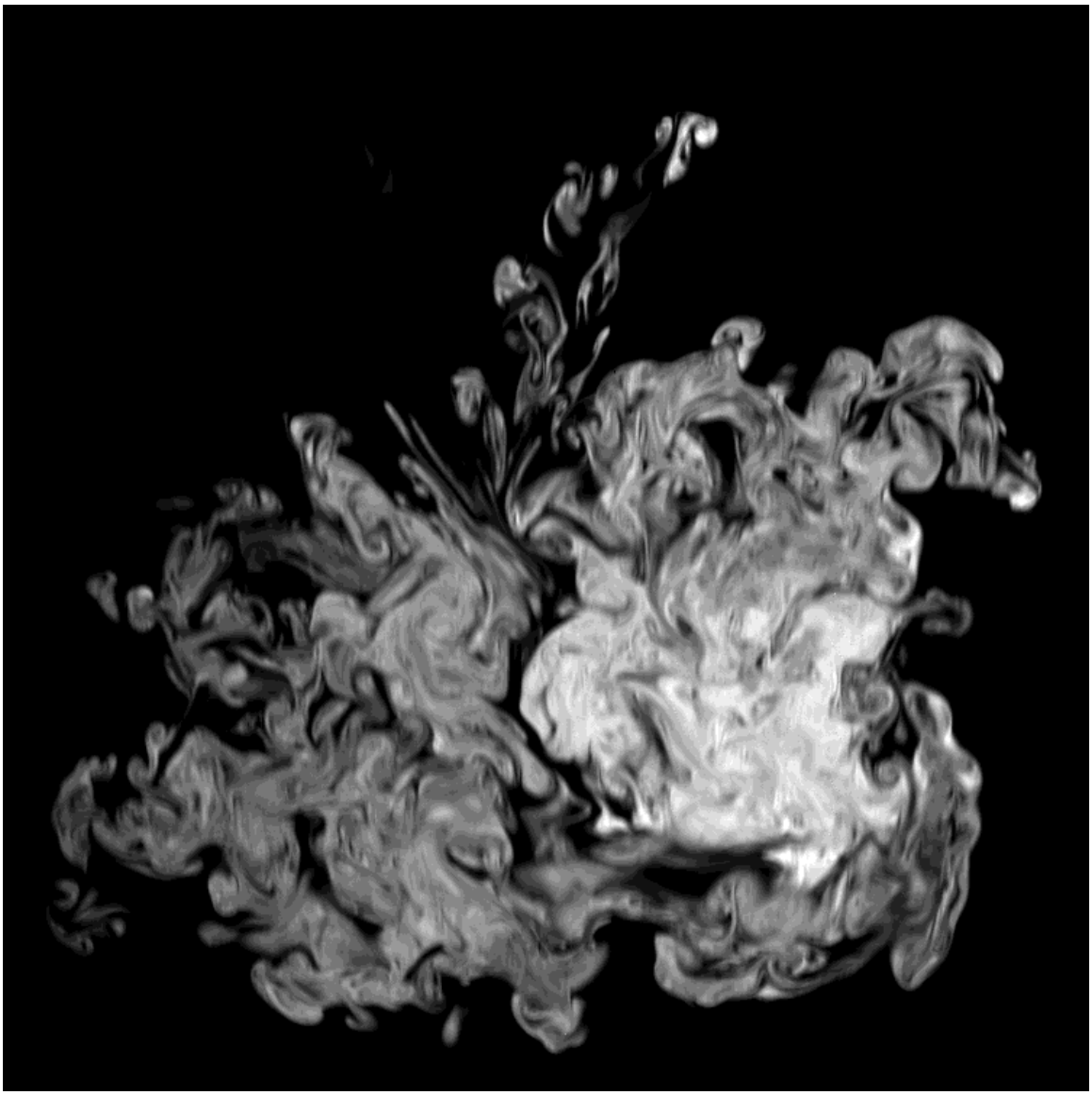

FIG. 2.8 Jet-fluid concentration in a transverse slice of the jet at downstream location $x/d_{\rm j} = 50$. $V_{\rm r} \simeq 10.1$ and $Re_{\rm j} = 10 \times 10^3$.

$Re_{\rm j} \simeq 2.0 \times 10^3$. The main features of the isosurface geometry are still visible, however.

Kuzo (1996) performed experiments measuring the velocity and vorticity fields of transverse jets at Reynolds numbers and velocity ratios similar to those investigated in this thesis. One component of vorticity was computed from digital-particle-imaging velocimetry (DPIV) measurements of velocity in a transverse plane

FIG. 2.9 Jet-fluid concentration in a transverse slice of the jet for $V_{\rm r} \simeq 32.3$ and $Re_{\rm j} = 1.0 \times 10^3$.

at $x/d_{\rm j} = 115$. The mean vorticity fields measured by Kuzo (1996) in cross-sections of the transverse jet are shown in Fig. 2.13. At $Re_{\rm j} = 2079$, Kuzo found tertiary and quaternary vortices in addition to the dominant vortex pair. Only a tertiary vortex was seen at $Re_{\rm j} = 4370$, and, by $Re_{\rm j} = 7250$, the jet consisted of a counter-rotating vortex pair.

Kuzo (1996) defined a symmetry parameter as the (absolute value of the) ratio

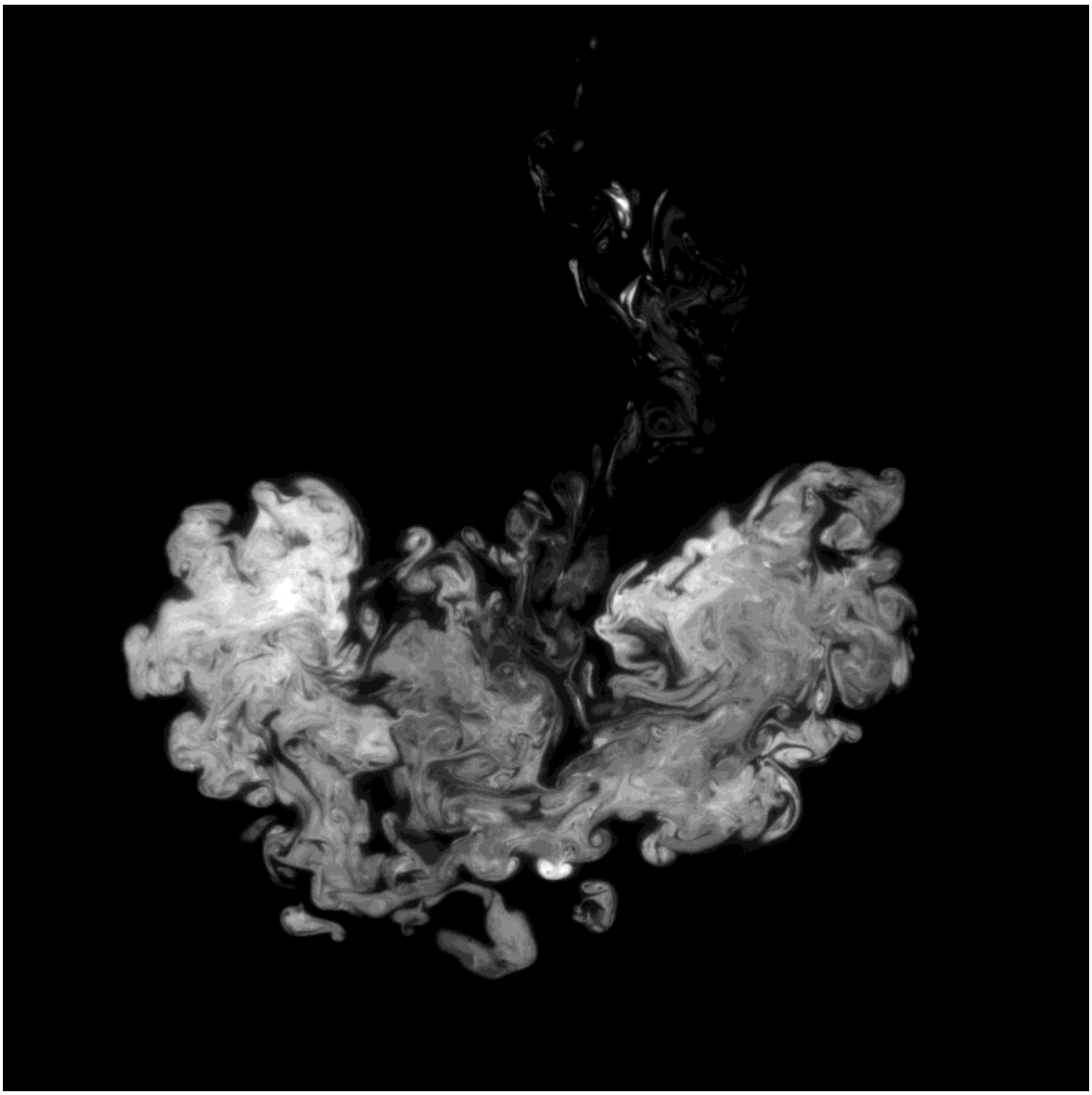

FIG. 2.10 Jet-fluid concentration in a transverse slice of the jet for $V_{\rm r} \simeq 32.3$ and $Re_{\rm j} = 10 \times 10^3$.

of circulation of the strongest positive and negative vortices. He found that the asymmetry in the strength of the vortices increased with Reynolds number, until approximately $Re_{\rm j} \simeq 7 \times 10^3$, at which point the tertiary and quaternary vortices disappeared, and the vortex pair become symmetric (for $V_{\rm r} = 10$). This transition from asymmetric to symmetric flow states was found to be abrupt, and a discontinuous function of Reynolds number (Fig. 2.13). These existence domain of these symmetric/asymmetric flow states is shown in Fig. 2.14 as a function of Reynolds

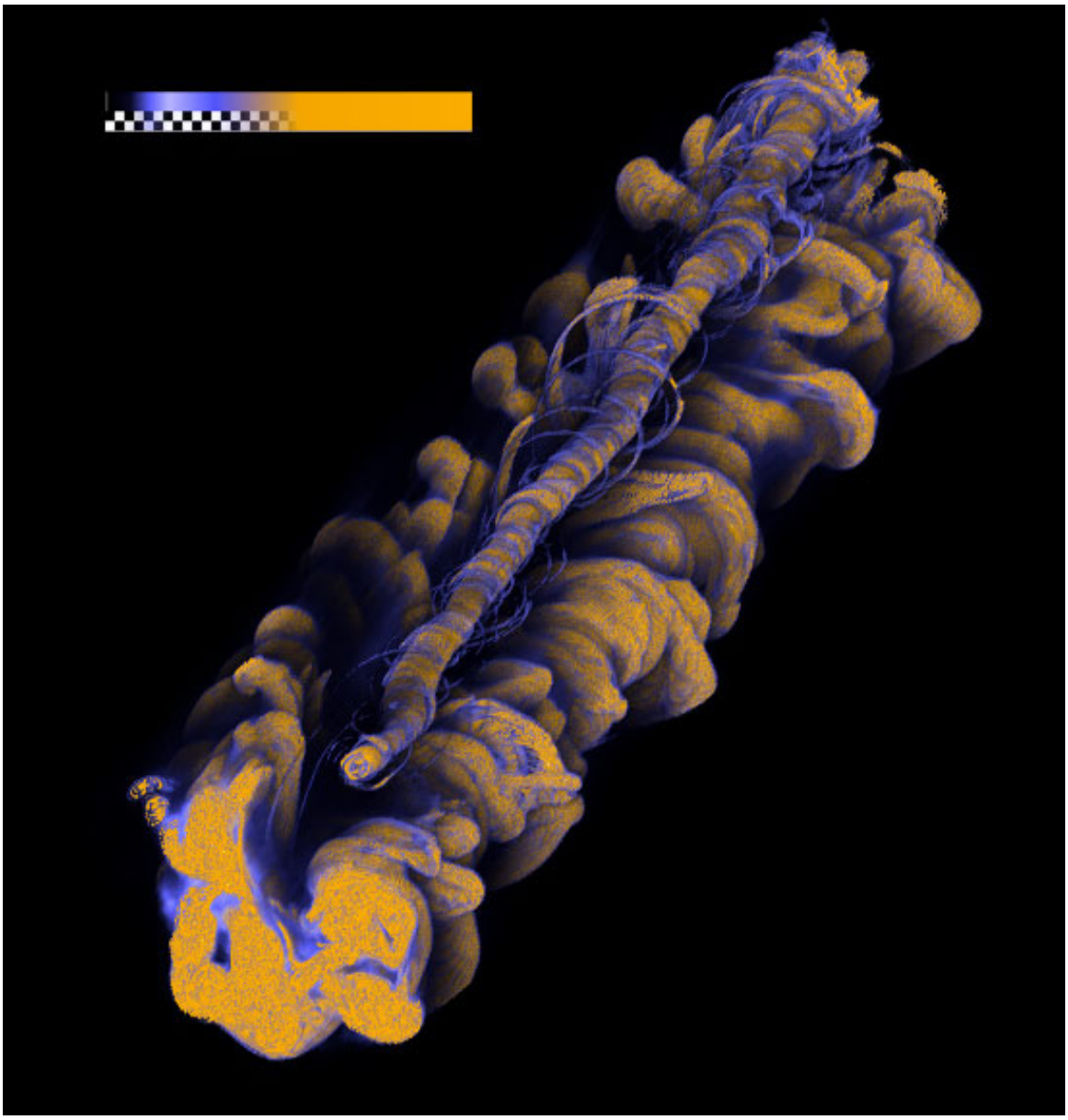

FIG. 2.11 Three-dimensional visualization of an isosurface of jet-fluid concentration for $Re_{\rm j} \simeq 1.0 \times 10^3$, $V_{\rm r} = 10.1$ transverse jet. The visualization is computed in collaboration with Santiago Lombeyda of Caltech's CACR.

number and velocity ratio. The Reynolds number for the transition to symmetric vortices was found to increase with velocity ratio.

Direct comparison is not possible between our LIF measurements of the scalar field, and Kuzo's DPIV measurements of the vorticity field in the transverse jet. However, our isosurface visualizations of the transverse jet are qualitatively sim-

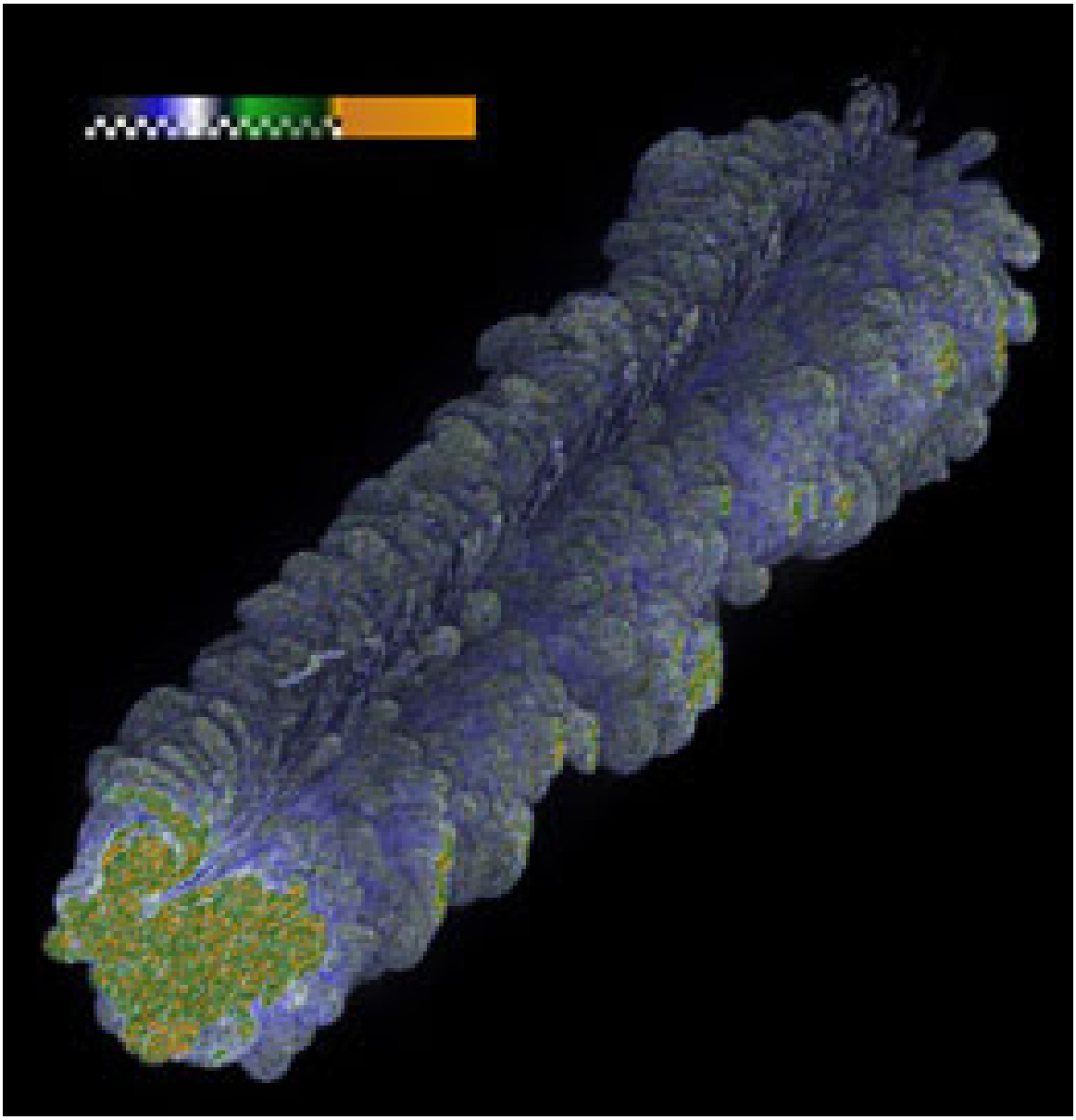

FIG. 2.12 Three-dimensional visualization of an isosurface for $Re_j \simeq 2.0 \times 10^3$, $V_r = 10.1$ transverse jet. The visualization is computed in collaboration with Santiago Lombeyda of Caltech's CACR.

ilar to the flow states found by Kuzo. Asymmetric mean flow is seen at low Reynolds number (Fig. 2.11), and a symmetric, or nearly symmetric vortex pair is seen at higher Reynolds numbers (Fig. 2.12). However, at similar Reynolds numbers ($Re_j \simeq 2 \times 10^3$), the isosurface visualization labels three vortices, while the vorticity measurement shows four vortices. The difference may be real, or may sim-

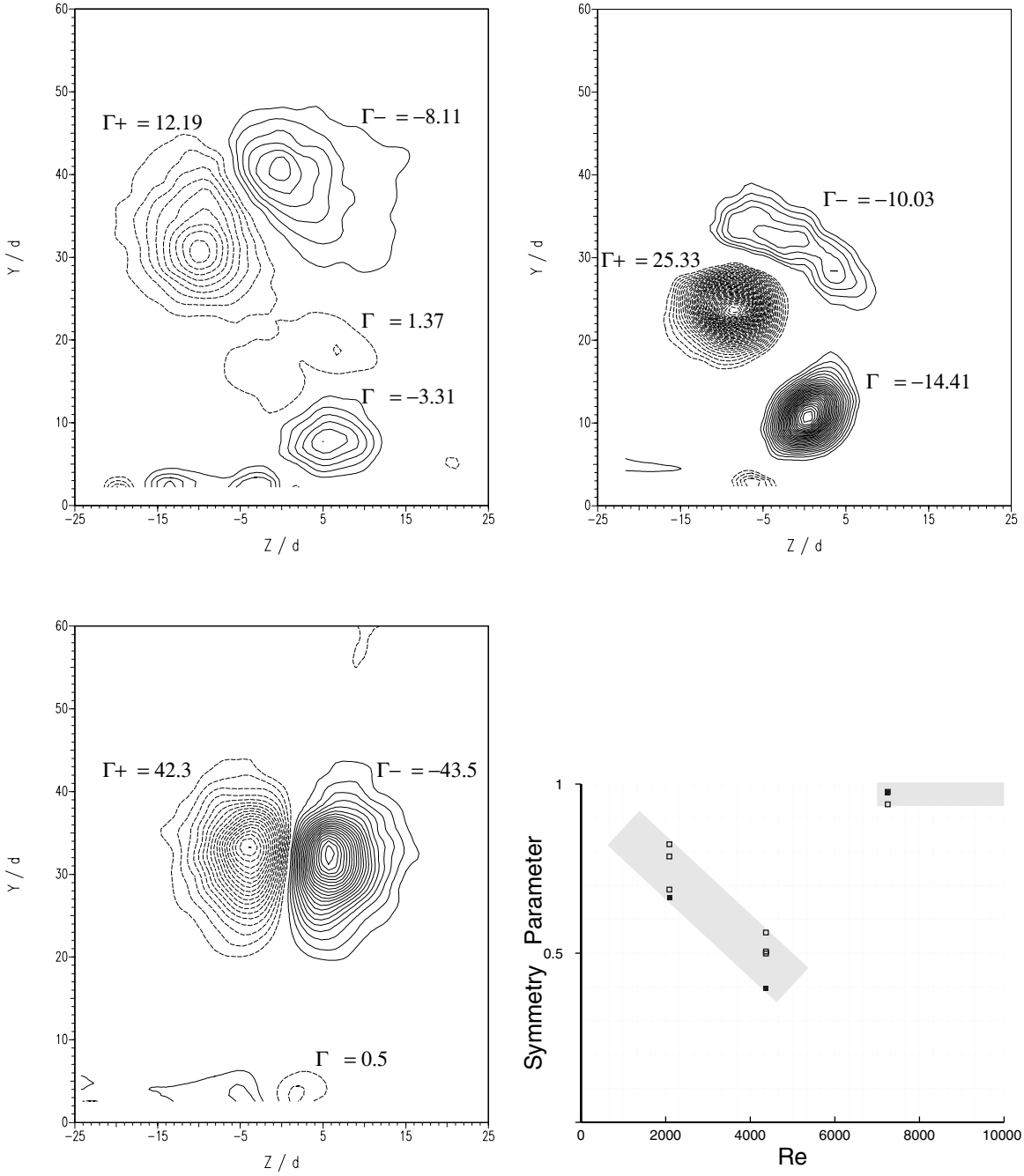

FIG. 2.13 Vorticity and circulation in transverse slices of jet at $x/d_{\rm j} = 115$. Velocity ratio $V_{\rm r} = 10$. Top left: $Re_{\rm j} = 2079$. Top right: $Re_{\rm j} = 4370$. Bottom left: $Re_{\rm j} = 7250$. Bottom right: Symmetry parameter (ratio of circulation of strongest positive and negative vortices) against Reynolds number. From Kuzo (1996).

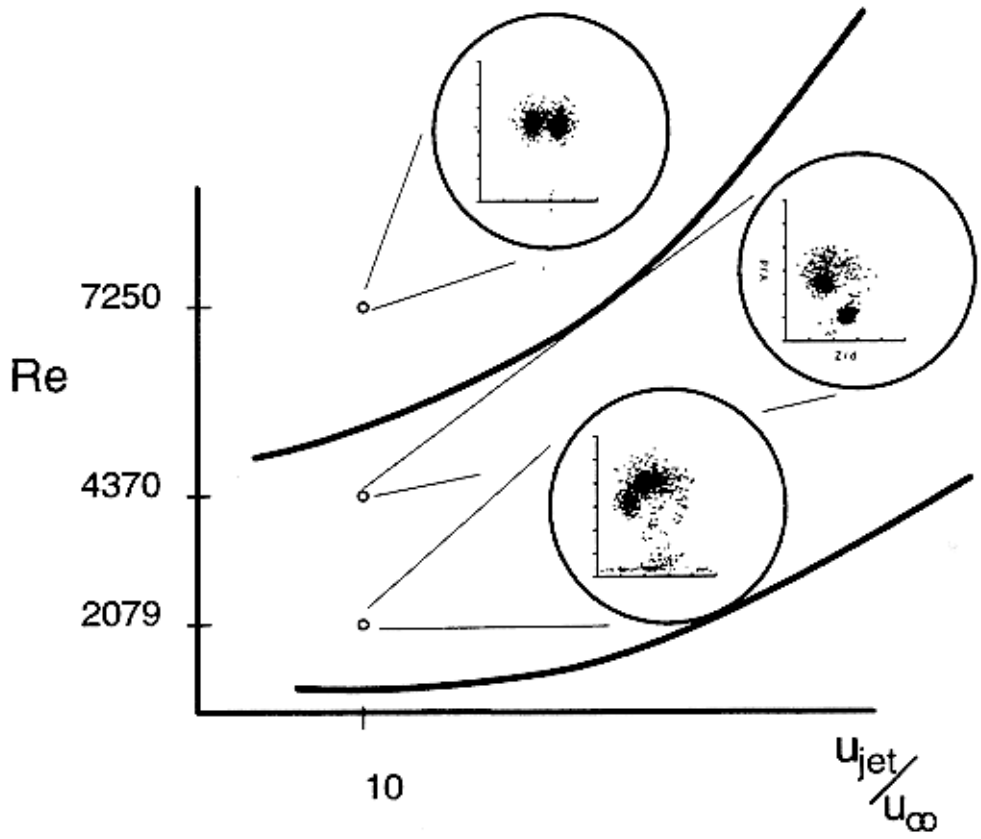

FIG. 2.14 Existence domain of symmetric/asymmetric flow states. From Kuzo (1996).

ply be a consequence of the entrainment (or lack thereof) of dye into the quaternary vortex.

2.5 Local Reynolds number and dissipation scales

For an axisymmetric jet discharging into a quiescent reservoir, the local Reynolds number, $Re(x) \equiv \delta(x)U_{\rm m}/\nu$, is constant after several nozzle diameters, $d_{\rm j}$. Here, $\delta(x)$ is the local width of the jet, $U_{\rm m}$ is the local mean centerline velocity, and ν is the kinematic viscosity. The local Reynolds number in the case of the turbulent jet in a quiescent reservoir is approximately equal to the jet-exit Reynolds number, $Re_{\rm j} \equiv d_{\rm j}U_{\rm j}/\nu$, where $U_{\rm j}$ is the jet-exit velocity. However, as will be shown, the local Reynolds number for the transverse jet is not constant in the far field, but decays with increasing downstream distance.

We follow Broadwell and Breidenthal (1984) in considering a jet of density ρ_j and velocity U_j discharging perpendicularly into a freestream of density ρ_∞ and velocity U_∞. In the limit in which the jet momentum flux, $\dot{m}_\mathrm{j} U_\mathrm{j} = \rho_j \pi (d_\mathrm{j}/2)^2 U_\mathrm{j}^2$, is held constant as jet diameter, d_j, decreases, and the discharge velocity, U_j, increases accordingly, the jet approaches a point source of normal momentum. This source of normal momentum, a "lift" force of vanishing drag, generates a counter-rotating vortex pair that is the analogue of tip-vortices behind a lifting wing. Broadwell and Breidenthal argue from dimensional analysis that, if viscosity has no global role and only serves to dissipate energy at the Kolmogorov scale, then the only global length scale for this limiting case of the transverse jet is:

$$l \;=\; \left(\frac{\dot{m}_\mathrm{j} U_\mathrm{j}}{\rho_\infty U_\infty^2} \right)^{1/2} \;\propto\; V_\mathrm{r}\, d_\mathrm{j}, \tag{2.2}$$

for $V_\mathrm{r} \equiv U_\mathrm{j}/U_\infty$, and equal jet and free-stream densities, $\rho_j = \rho_\infty$. The circulation of one vortex, Γ, the vortex-core separation distance, R, and the vortices' vertical velocity, $\mathrm{d}y/\mathrm{d}t$, are related by

$$\frac{\mathrm{d}y}{\mathrm{d}t} \;=\; \frac{c_1 \Gamma}{R}. \tag{2.3}$$

The fluid impulse per unit length, P, is related to the circulation, Γ, and the vortex-core separation by

$$P \;=\; c_2\, \rho_\infty \Gamma R. \tag{2.4}$$

The constants c_1 and c_2 depend on the distribution of vorticity in the vortex pair, *e.g.*, for line vortices, $c_1 = \pi/4$ and $c_2 = 2$. Equations 2.3 and 2.4 assume that the transverse jet forms a single counter-rotating vortex pair, in the far field. As noted in the previous section, tertiary and quaternary vortices are sometimes formed, particularly at low Reynolds numbers. In such a situation, the vortices would no longer have equal circulation, and each vortex could have a different induced velocity. But, for simplicity, we consider the high Reynolds-number case, in which a single vortex pair is always found. Assuming a similarity form in which the flow is independent of l in the far field (*i.e.*, R is proportional to y), Eq. 2.4 may be substituted into Eq. 2.3, and integrated to find

$$y = c_3 \left(\frac{P}{\rho_\infty} \right)^{1/3} t^{1/3} \tag{2.5}$$

We use the (far-field) transformation $x = U_\infty t$, and note that $P = \dot{m}_\mathrm{j} U_\mathrm{j}/U_\infty$, to find that the trajectory is (Broadwell and Breidenthal 1984)

$$\frac{y}{l} = c_3 \left(\frac{x}{l}\right)^{1/3}.$$

The circulation of one vortex is

$$\frac{\Gamma}{U_\infty l} \;=\; c \left(\frac{x}{l}\right)^{-1/3}, \tag{2.6}$$

where x is downstream (horizontal) distance from the jet exit, and c is a constant. This result may be expected to hold in the far field ($x \gg l$) of high-velocity ratio ($V_\mathrm{r} \gg 1$) transverse jets. Although the fluid impulse per unit length, P, is constant, the separation distance, R, is a function of x. Thus, the circulation is found to be a function of downstream distance, x. This is consistent with the physical picture of two counter-rotating vortices in close proximity decaying through viscous diffusion.

As an aside, we note that the similarity analysis of Broadwell and Breidenthal (1984) assumes that the form of the transverse jet is a counter-rotating vortex pair, and that the vortex-core separation distance, R, is proportional to the penetration depth, y, in the far field ($c \gg l$). It was suggested (Leonard and Hornung 2001) that, yet further downstream, the transverse jet might "forget" about the wall, and R would be a constant independent of both l and y. If this is the case, Eq. 2.3 and Eq. 2.4 may be combined to yield

$$\frac{\mathrm{d}y}{\mathrm{d}t} \;=\; \frac{c_3 P}{\rho_\infty R^2}. \tag{2.7a}$$

Noting that P is constant, and using the far-field transformation, $x = U_\infty t$, we find that the trajectory would be proportional to x, *i.e.*,

$$y \;=\; \frac{c_3 P x}{\rho_\infty U_\infty R^2} \;\propto\; x. \tag{2.7b}$$

Although the prediction of Broadwell and Breidenthal is that $y \propto x^{1/3}$ in the far field, Eq. 2.7 suggests that, further downstream, the transverse-jet trajectory may become linear. However, a linear jet trajectory would imply that the circulation is constant (*cf.* Eq. 2.4), since P and R are constants. It appears unlikely that two counter-rotating vortices in close proximity could maintain constant circulation in the face of viscous diffusion and vorticity annihilation. However, we note this possibility of linear trajectories because it has not been experimentally considered to our knowledge. Up to $x/d_\mathrm{j} < 50$, this thesis (Ch. 3), and other experiments, show approximately power-law jet trajectories of the form $y \propto x^{1/3}$.

For high Reynolds-number jets, the counter-rotating vortex pair is the dominant dynamic structure, and the primary mechanism for entrainment of irrotational freestream fluid by the transverse jet. In this case, a local, circulation-based Reynolds number, Re_Γ, is likely more relevant to turbulence and turbulent mixing in the transverse jet than the jet-exit Reynolds number, Re_j. A local Reynolds number can be defined based on the vortex circulation,

$$Re_\Gamma(x) \equiv \frac{\Gamma}{\nu} \;=\; c\,\frac{U_\infty l}{\nu}\left(\frac{x}{l}\right)^{-1/3}. \tag{2.8}$$

The local Reynolds number, $Re(x)$, is seen to be related to the jet-exit Reynolds number, Re_j, as

$$Re(x) \equiv Re_\Gamma(x) \;=\; c\,\frac{U_\mathrm{j} d_\mathrm{j}}{\nu}\left(\frac{x}{l}\right)^{-1/3} \;=\; c\,Re_\mathrm{j}\left(\frac{x}{l}\right)^{-1/3}, \tag{2.9a}$$

where we have used $l = V_\mathrm{r}\, d_\mathrm{j}$. For a given velocity ratio, the local Reynolds number decays as $(x/d_\mathrm{j})^{-1/3}$ with increasing downstream distance. Although the precise value of the constant, c, is undetermined, we expect the local Reynolds number, $Re_\Gamma(x)$, to approach the jet-exit Reynolds number, Re_j, as $x/l \to 1$. Taking the constant $c \simeq 1$, and using the conditions of the present experiments ($x/d_\mathrm{j} = 50$ and $V_\mathrm{r} = 10.1$), we find

$$Re_\Gamma(x) \;=\; \left(\frac{x/d_\mathrm{j}}{V_\mathrm{r}}\right)^{-1/3} Re_\mathrm{j} \;\simeq\; 0.6\,Re_\mathrm{j}. \tag{2.9b}$$

Thus, the jet-exit Reynolds number Re_j referred to in this thesis may be related to local Reynolds numbers at $x/d_\mathrm{j} = 50$ by multiplying by 0.6.

An estimate of the dissipation scales of the flow may be made based upon the local Reynolds number, $Re_\Gamma(x)$. The Kolmogorov scale, based upon the energy dissipation rate, ϵ, is defined as

$$\lambda_\mathrm{K} \;\equiv\; \left(\frac{\nu^3}{\epsilon}\right)^{1/4}. \tag{2.10}$$

A direct calculation of the Kolmogorov scale for the transverse jet is not possible since no estimate for the energy dissipation rate ϵ is available in the literature. However, from scaling arguments, the Kolmogorov scale is related to the (local) outer scale, $\delta(x)$, by

$$\frac{\lambda_\mathrm{K}}{\delta(x)} \;\simeq\; c_3 Re(x)^{-3/4}, \tag{2.11a}$$

where $Re(x)$ is the local Reynolds number. The constant, c_3, in Eq. 2.11 is taken to be unity on the basis of results in turbulent jets (Dimotakis 2000). For the experiments on the transverse jet described here, the outer scale $\delta(x) \simeq 1000$ pixels. The Kolmogorov scale, based upon the local, circulation-based, Reynolds number, is

$$\frac{\lambda_{\rm K}}{\delta(x)} \;\simeq\; Re(x)^{-3/4} \;\simeq\; Re_{\rm j}^{-3/4} \left(\frac{x}{l}\right)^{1/4}. \tag{2.11b}$$

We find the respective Kolmogorov scales to be $\lambda_{\rm K} \simeq 8.4,\ 5.0,\ 2.5,\ 1.5$, and 0.89 pixels, respectively, for jet Reynolds numbers $Re_{\rm j} = 1.0 \times 10^3,\ 2.0 \times 10^3,\ 5.0 \times 10^3,\ 10 \times 10^3$, and 20×10^3, at $x/d_{\rm j} = 50$.

The viscous scale, λ_ν, defined as the scale where the turbulence spectrum deviates from -5/3 power-law behavior, is estimated to be a factor of 50 times larger than the Kolmogorov scale $\lambda_{\rm K}$ (Dimotakis 2000). This result is found to hold for a variety of flows across a wide range of Reynolds numbers. We estimate the scalar-diffusion scale, $\lambda_{\mathcal{D}}$, as a multiple of the viscous scale, λ_ν, *i.e.*,

$$\lambda_{\mathcal{D}} \;\simeq\; Sc^{-1/2}\lambda_\nu = 50 Sc^{-1/2}\lambda_{\rm K},$$

where $Sc \equiv \nu/\mathcal{D}$ is the Schmidt number. For the present experiments on the transverse jet, the scalar-diffusion scales are estimated to be $\lambda_{\mathcal{D}} \simeq 4.6,\ 2.7,\ 1.4,\ 0.82$, and 0.49 pixels, respectively, for jet Reynolds numbers $Re_{\rm j} = 1.0,\ 2.0,\ 5.0,\ 10$, and 20×10^3, at $x/d_{\rm j} = 50$.

CHAPTER 3

Turbulent mixing in jets: classical measures

Classical measures of turbulent jets are studied using two-dimensional measurements of jet-fluid concentration. Trajectories and maximum mean-concentration decay for transverse jets are investigated at two different Reynolds numbers, $Re_{\mathrm{j}} = 1.0 \times 10^3$ and $Re_{\mathrm{j}} = 10 \times 10^3$. Ensemble-averaged, two-dimensional scalar power spectra are also computed for these two Reynolds numbers. The Reynolds-number dependence and isotropy of the scalar field is assessed in terms of these classical measures.

3.1 Jet trajectory

Mean transverse-jet trajectories have been defined in a variety of ways. Yuan *et al.* (1999), for instance, define the trajectory as the mean streamline originating from the center of the jet nozzle. Depending on whether the primary interest is in scalar mixing or flow dynamics, trajectories have been more commonly identified by the locus of points of concentration or velocity maxima on the jet centerline (Pratte and Baines 1967, Kamotani and Greber 1972). We have chosen to define the trajectory as the locus of points for which the mean jet-fluid concentration is maximum on the centerplane. The ensemble-averaged concentration field for streamwise views of the transverse jet is shown in Fig. 3.1 for $Re_{\rm j} = 1.0 \times 10^3$. Trajectories are computed from the maximum concentration points in such ensemble-averaged images. Figure 3.2 shows scalar jet trajectories, for $Re_{\rm j} = 1.0 \times 10^3$ and 10×10^3, each calculated from ensemble averages of 254 streamwise sections on the centerline of the transverse jet. For comparison, a line of slope 1/4, corresponding to a power-law trajectory, $y/d_{\rm j} \propto (x/d_{\rm j})^{1/4}$, is shown. A line of slope 1/3, corresponding to a power-law trajectory, $y/d_{\rm j} \propto (x/d_{\rm j})^{1/3}$, is also shown. Pratte and Baines reported a power-law trajectory of the form $y/d_{\rm j} \propto (x/d_{\rm j})^{0.28}$ in their experiments, while Broadwell and Breidenthal predict a power-law trajectory of the form $y/d_{\rm j} \propto (x/d_{\rm j})^{1/3}$ from their similarity analysis.

Trajectories computed as loci of scalar maxima are known to differ from maximum-velocity trajectories and mean nozzle-streamline trajectories. This has been shown both experimentally (*e.g.*, Kamotani and Greber 1972) and by large eddy simulation (*e.g.*, Yuan *et al.* 1999). Penetration depths for scalar maxima are found to be slightly, but consistently, smaller than those of velocity maxima, or nozzle-streamlines.

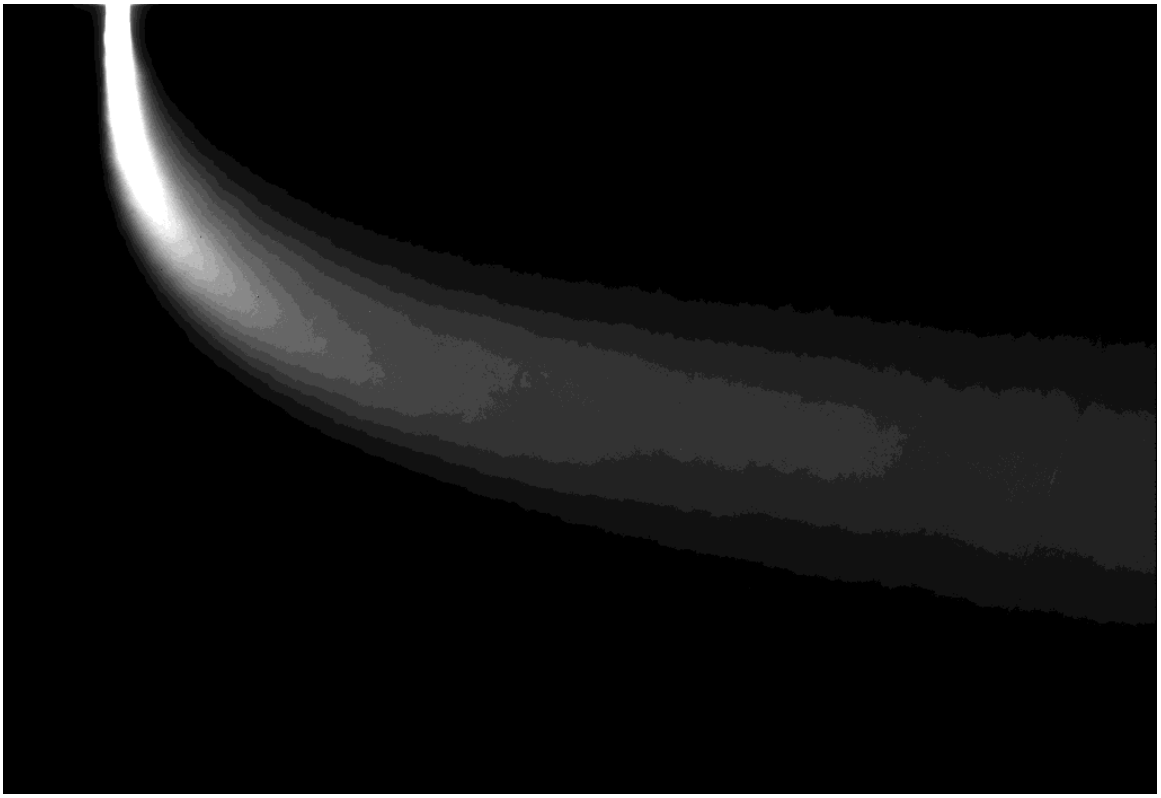

FIG. 3.1 Mean concentration field for $Re_{\rm j} = 10 \times 10^3$ and $V_{\rm r} \simeq 10.1$. Ensemble averaged from 254 streamwise (plane-of-symmetry) slices of transverse jet.

3.2 Concentration decay

The decay of the maximum centerline concentration of the ensemble-averaged scalar field is plotted in Fig. 3.3 as a function of nondimensionalized downstream distance, $x/d_{\rm j}$, and penetration depth, $y/d_{\rm j}$, for $Re_{\rm j} = 1.0 \times 10^3$ and 10×10^3. Concentration decay with downstream distance is nearly power-law with an exponent -2/3, consistent with the gas-phase transverse-jet experiments of Smith and Mungal (1998). Little variation with Reynolds number is seen between $Re_{\rm j} = 1.0 \times 10^3$ and 10×10^3. However, the maximum concentration decay with penetration depth is clearly not power law, and also shows an initial dependence on Reynolds number that is attributable to the longer potential-core length for lower-Reynolds-number jets. By $y/d_{\rm j} \simeq 5$, the initially slower-mixing $Re_{\rm j} = 1.0 \times 10^3$ jet is unsteady and turbulent, and its decay trajectory overlaps with that of the $Re_{\rm j} = 10 \times 10^3$ jet. There is agreement in the literature that the jet trajectory is power law (Pratte and

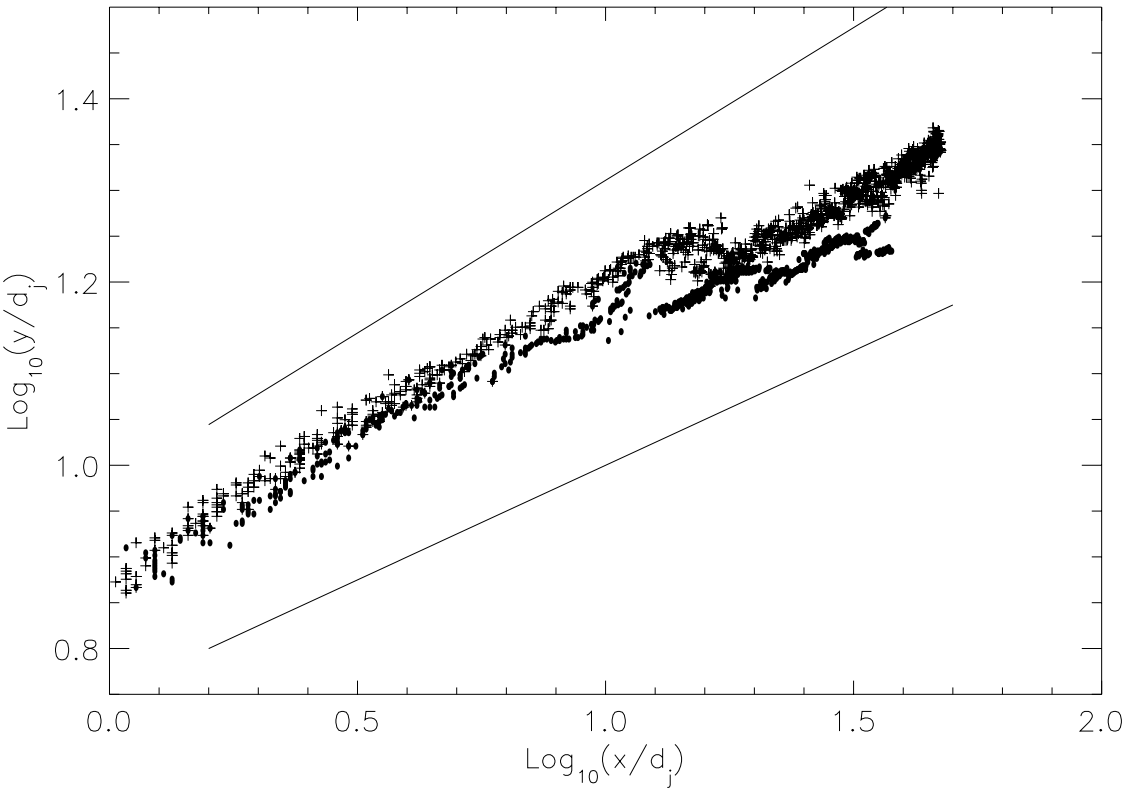

FIG. 3.2 Maximum jet-fluid-concentration trajectory. Penetration depth versus downstream distance with logarithmic axes. Lower comparison line is $y/d_{\rm j} \propto (x/d_{\rm j})^{1/4}$ (*cf.* experiments of Pratte and Baines 1967). Upper comparison line is) $y/d_{\rm j} \propto (x/d_{\rm j})^{1/3}$ (*cf.* prediction of Broadwell and Breidenthal 1984). $Re_{\rm j} = 1.0 \times 10^3$: circles, $Re_{\rm j} = 10 \times 10^3$: crosses.

Baines 1967, Kamotani and Greber 1972, Chassaing *et al.* 1974). We note that it would be inconsistent for the maximum-concentration trajectory, $y = Y(x)$, to be power law if maximum-concentration decay with downstream distance, x, is power law, and maximum-concentration decay with penetration depth, y, is not power law.

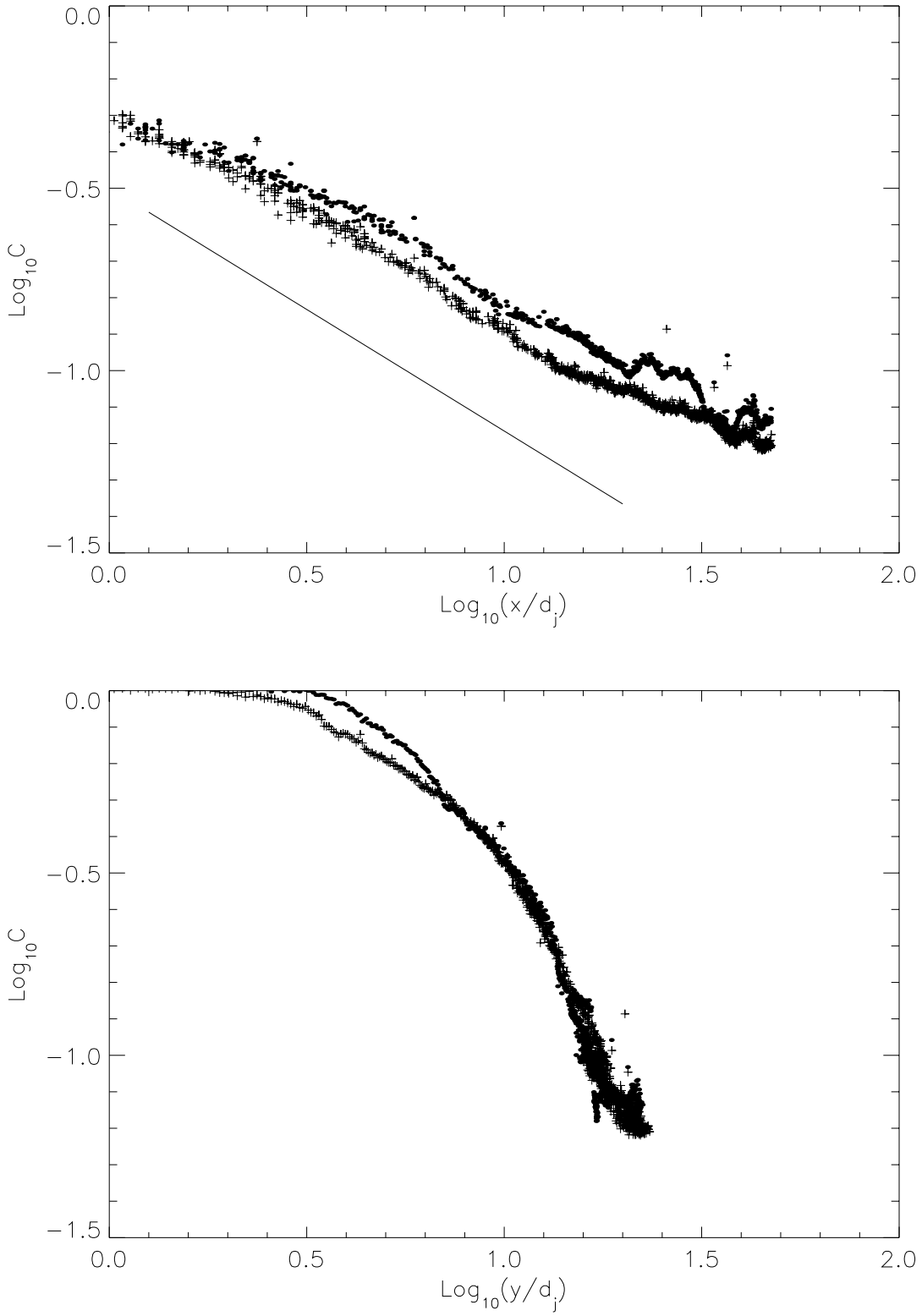

FIG. 3.3 Decay of maximum mean concentration, in logarithmic coordinates. $Re_{\rm j} = 1.0{\times}10^3$ is shown with circles, $Re_{\rm j} = 10{\times}10^3$ with crosses. Top: Concentration decay with downstream distance. Comparison line is $C \propto (x/d_{\rm j})^{-2/3}$ (*cf.* Smith and Mungal 1998). Bottom: Concentration decay with penetration depth.

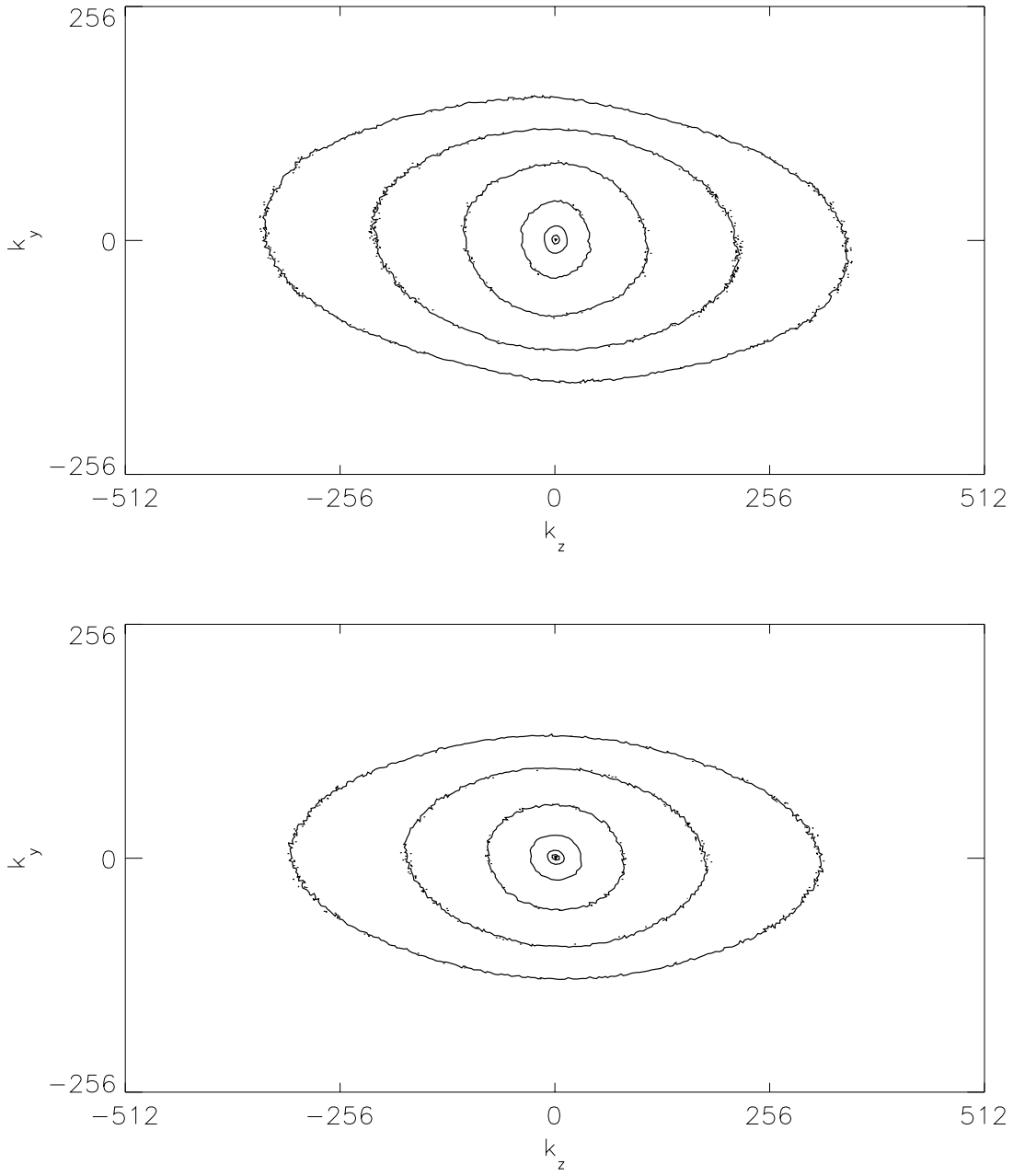

FIG. 3.4 Two-dimensional power spectra of the scalar field of the transverse jet at $x/d = 50$. Contour plot in $\log_{10}$ increments of 1.0. Top: $Re_{\rm j} = 1.0 \times 10^3$. Bottom: $Re_{\rm j} = 10 \times 10^3$.

3.3 Scalar power spectra

The scalar field of the transverse jet is spatially confined, and thus inhomogeneous. Scalar power spectra are shown in Fig. 3.4 for $Re_{\rm j} = 1.0 \times 10^3$ and 10×10^3 jets at $x/d = 50$. These two-dimensional power spectra indicate that the transverse-

jet scalar field is not isotropic. Power spectral densities (PSD) are calculated as the modulus squared of the discrete Fourier transform of the Hann-windowed concentration field, and ensemble-averaged over 508 images for each Reynolds number. Contour plots of the ensemble-averaged PSD, in $\log_{10}$ increments of 1.0, show that the scalar field is not axisymmetric in any statistical sense. The power-spectra contours are increasingly elliptical with higher wavenumbers. These results indicate that scalar gradients are steeper horizontally than vertically, due to overall vertical straining (or history of vertical straining), in the transverse jet. While large scales (small wavenumbers) are more isotropic in the two in-plane directions, y and z, the smaller length scales are increasingly anisotropic. Small-scale scalar anisotropy, evident in the spatial power spectra, stands in contrast to the statistical axisymmetry of the ordinary round turbulent jet (*cf.* Catrakis and Dimotakis 1996). The anisotropy of the scalar field for the transverse jet is, however, consistent with scalar anisotropy for other turbulent shear flows. (*e.g.*, Sreenivasan 1991).

CHAPTER 4

Probability density function of scalar field

The spatial probability-density function of the scalar field is considered in this chapter. The difference between one-dimensional, temporal PDFs and d-dimensional, spatial PDFs is discussed. Spatial PDFs for two-dimensional measurements of the jet-fluid-concentration field are analyzed for both transverse ($x/d_{\mathrm{j}} = 50$) and streamwise sections of the jet in crossflow. The evolution with Reynolds numbers of several scalar-field measures is discussed: the PDF of jet-fluid concentration, the mean concentration, the peak concentration, and the mean mixed-fluid concentration. A comparison is made between mixing in transverse jets and turbulent jets discharging into a quiescent reservoir. Based upon this comparison, the flow-dependence of turbulent mixing in free-shear flows is discussed.

4.1 Introduction

Probability-density functions (PDFs) describe statistics of the fluctuating quantities (*e.g.*, velocity or scalar concentration) inherent to turbulent flows. They can be used to compute all moments of the fluctuations, and form the basis for statistical approaches toward turbulent flow with chemical reactions (Pope 1985, Goldin and Menon 1997). In these formulations, the Navier-Stokes equations, along with scalar-transport and chemical-reaction equations, are recast into an evolution equation for the joint PDF of flow variables.

The PDF, $f(C)$, of a random variable, C, is defined such that its integral gives the probability that $C_1 \leq C < C_2$, *i.e.*,

$$\Pr\{C_1 \leq C < C_2\} = \int_{C_1}^{C_2} f(c)dc = F(C_1) - F(C_2). \tag{4.1}$$

The PDFs discussed in this thesis are spatial, rather than temporal, PDFs. They are based upon the probability of occurrence for C within image data of the scalar concentration field. The spatial PDF is (normalized magnitude of) the differential area associated with a differential concentration (Kuznetsov and Sabelnikov 1990, Catrakis and Dimotakis 1996), in two-dimensions,

$$f(C) \;=\; \frac{1}{A_{\rm tot}} \left| \frac{{\rm d}A(C)}{{\rm d}C} \right|, \tag{4.2a}$$

and in d-dimensions,

$$f_n(C) \;=\; \frac{1}{V_{d,{\rm tot}}} \left| \frac{{\rm d}V_d(C)}{{\rm d}C} \right|. \tag{4.2b}$$

In two-dimensions, $A(C)$ is the area associated with a specified value of the scalar concentration, C, in the image. In d-dimensions, $V_d(C)$ is the d-dimensional volume associated with each value of C. $A_{\rm tot}$ and $V_{d,{\rm tot}}$ are the total area and volume, respectively, of the spatial measurement of the scalar field.

In general, PDFs depend not only on the statistics of the scalar field, $C(\mathbf{r}, t)$, but also on the dimensionality of the space or measurement (see Appendix A). We note that spatial PDFs differ from one-dimensional, temporal PDFs at a point. Rather than the temporal probability of occurrence of C at a fixed spatial location, the spatial PDF is associated with the differential probability of finding scalar concentration C in d-dimensional space.

4.2 Scalar probability-density functions in transverse sections

For the transverse jet, spatial PDFs of jet-fluid concentration are computed from normalized histograms of the scalar-image data (Figs. 2.7 and 2.8). The PDFs at each Reynolds number are estimated from 508 images, each image (1024×1024)-pixels in resolution, so that the PDFs consist of 5.4×10^8 point measurements of the scalar concentration field. The large number of measurements allows the concentration histograms to be computed for order 10^2 bins, yielding PDFs that are well resolved in C.

Figure 4.1 shows the PDF for transverse sections of the jet at $x/d_\mathrm{j} = 50$, for Reynolds numbers $Re_\mathrm{j} = 1.0$, 2.0, 5.0, 10, and 20×10^3. The singularity in the PDFs at $C = 0$ is a consequence of the unmixed, freestream fluid surrounding the spatially-confined jet. This singularity at the origin is excluded in the normalization of the PDFs. At $Re_\mathrm{j} = 1.0 \times 10^3$, the PDF is peaked around $C = 0$ and decreases monotonically with increasing scalar concentration. This is qualitatively similar to the PDF of a diffusive (Gaussian) concentration distribution (Appendix A). The jet-fluid concentration PDF at $Re_\mathrm{j} = 2.0 \times 10^3$ still decreases monotonically, but shows less probability for unmixed, high-C fluid than at $Re_\mathrm{j} = 1.0 \times 10^3$. By Reynolds number 5.0×10^3, a distinct peak in the PDF has formed near $C \simeq 0.04$. Peaks in the jet-fluid-concentration PDF, which occur for $Re_\mathrm{j} \geq 5.0 \times 10^3$, are not symmetric about the most probable concentration, but biased toward lower concentrations. At fixed downstream location, the scalar PDF qualitatively changes shape over the range $1.0 \times 10^3 \leq Re_\mathrm{j} \leq 20 \times 10^3$, with growing peaks implying more-uniform mixing (*i.e.*, better spatial homogenization of the scalar field) with increasing Reynolds number. In this sense, mixing is enhanced by increasing Reynolds number.

Figure 4.2 shows that the peaks, C_peak, of the jet-fluid concentration PDFs shift slightly to lower concentrations at successively higher Reynolds numbers, but appear to asymptote between $Re_\mathrm{j} = 10 \times 10^3$ and 20×10^3. Recall from Ch. 2 that the local Reynolds number, Re_Γ, is approximately 0.6 times the jet Reynolds number, Re_j, for velocity ratio $V_\mathrm{r} = 10.1$ and $x/d_\mathrm{j} = 50$. Thus, jet Reynolds numbers $Re_\mathrm{j} = 10 \times 10^3$ and 20×10^3, have corresponding local (circulation-based) Reynolds numbers of $Re_\Gamma = 5.9 \times 10^3$ and 12×10^3, respectively. The asymptotic behavior of the PDFs that is seen around Reynolds numbers $Re_\Gamma = 5.9 \times 10^3$ to

12×10^3 is consistent with the mixing transition documented in other flows for (local) Reynolds number $Re \simeq 10^4$ (Dimotakis 2000). The mean mixed-fluid-fluid concentration, defined as the mean of all concentrations $C > 0.01$, also decreases with increasing Reynolds number, and levels off around $Re = 10^4$.

As an aside, we note that control-volume analysis shows that the mean concentration, $\bar{C}$, in a far-downstream transverse plane, depends linearly on the jet-exit concentration, C_0, and the velocity ratio, V_r,

$$\bar{C} \;=\; \int_{-\infty}^{\infty} C\, f(C)\, \mathrm{d}C \;=\; \int_{0}^{1} C\, f(C)\, \mathrm{d}C \;\simeq\; C_0\, V_\mathrm{r}\, \frac{A_\mathrm{j}}{A} \tag{4.3}$$

where A_j is the exit area of the nozzle and A is the total area of the image plane. Recall that $0 \leq C \leq 1$, from Eq. 2.1. When C_0 and V_r are constant, as they are in these experiments, the mean concentration, $\bar{C}$, in a far-downstream plane should be independent of Reynolds number. This is verified in Fig. 4.2 for $1.0 \times 10^3 \leq Re_\mathrm{j} \leq 20 \times 10^3$.

4.3 Scalar probability-density functions in streamwise sections

Probability-density functions are also computed from streamwise sections of the scalar-concentration field on the centerline of the transverse jet (*e.g.*, Figs. 2.3 and 2.4), for $Re_\mathrm{j} = 1.0$, 2.0, 5.0, and 10×10^3. The downstream progression in scalar mixing is studied by computing jet-fluid-concentration PDFs for eight vertical, $6d_\mathrm{j}$-wide strips, with the first strip covering the jet exit, and the last strip centered at $x/d_\mathrm{j} = 50$ (Fig. 4.3). Figure 4.4 shows the scalar-field PDFs with increasing downstream distance for $Re_\mathrm{j} = 1.0 \times 10^3$ and 10×10^3 transverse jets. A small peak near $C = 1$ is seen in the PDF of the strip that includes the jet exit. The jet-fluid concentration PDFs shift toward lower concentrations with increasing downstream distance. Maximum concentration on the centerplane of the jet decreases rapidly with increasing downstream distance. This suggests that much of the entrainment of crossflow fluid and mixing of high scalar concentrations occurs relatively close to the jet nozzle (*cf.* Smith and Mungal 1998). A comparison of the PDFs for $Re_\mathrm{j} = 1.0 \times 10^3$ and 10×10^3 shows that the probability of finding unmixed, high-concentration

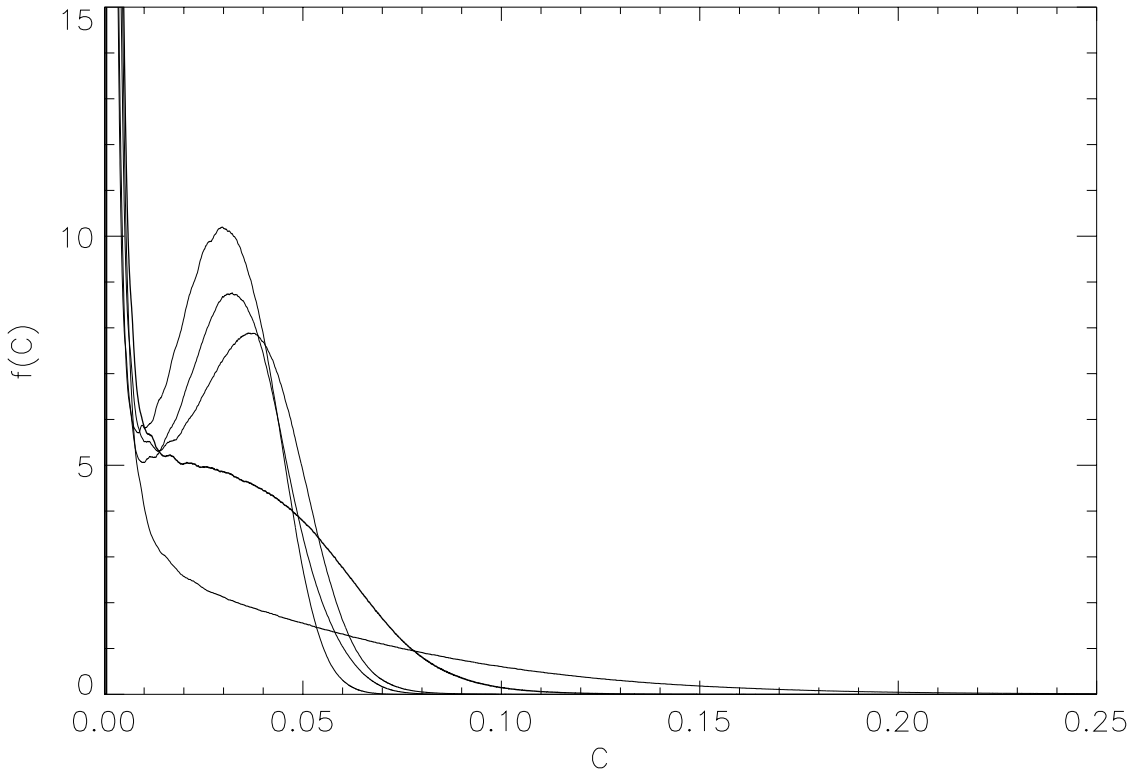

FIG. 4.1 PDFs of jet-fluid-concentration in transverse slices (*cf.* Fig. 2.7) of jet at $x/d_{\rm j} = 50$. Concentrations normalized by plenum-exit concentration, $C = c/c_0$. Increasingly peaked PDFs at $C \simeq 0.04$ with increasing Reynolds number for $Re_{\rm j} = 1.0$, 2.0, 5.0, 10, and 20×10^3.

fluid at any given downstream location, $x/d_{\rm j}$, decreases with increasing Reynolds number. The enhanced scalar mixing at higher Reynolds numbers also manifests itself in the sharp peaks in the PDF at $Re_{\rm j} = 10 \times 10^3$, which indicate a preference for uniformly-mixed fluid. For $Re_{\rm j} = 1.0 \times 10^3$, peaks in the PDF have not yet developed for $x/d_{\rm j} = 50$, and the PDF shows (approximately) equal probability for a broad range of jet-fluid concentrations.

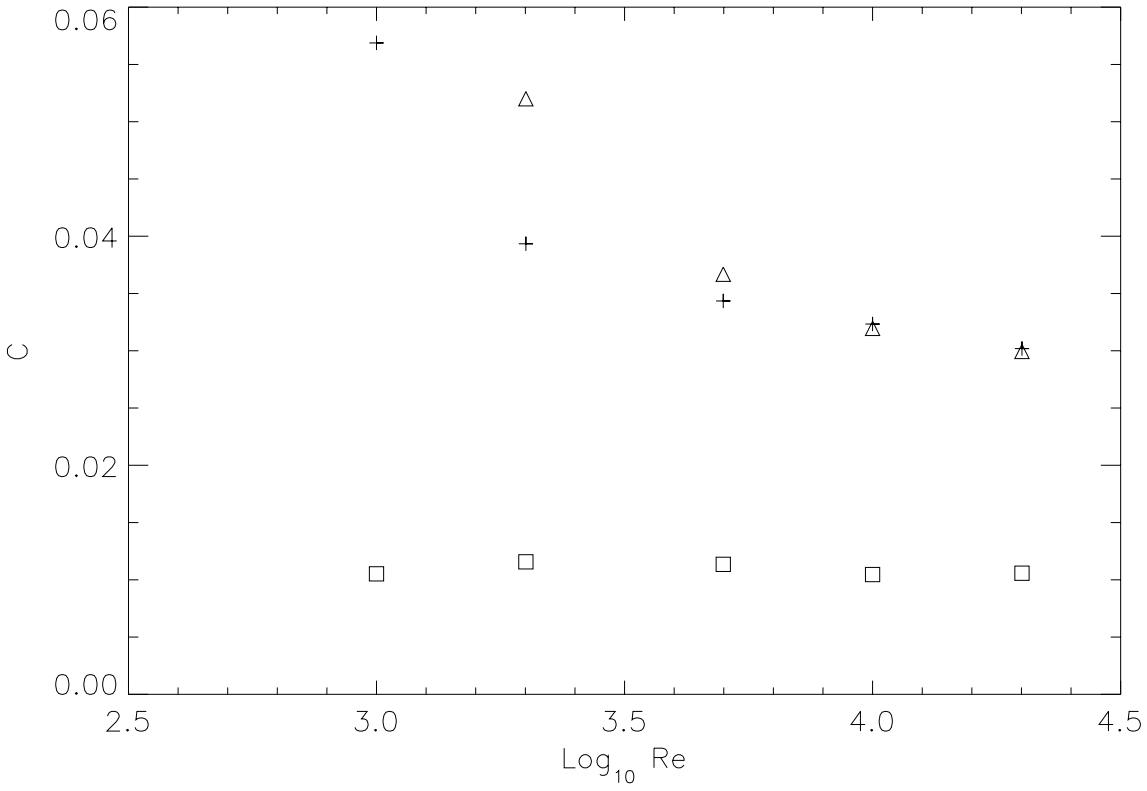

FIG. 4.2 Concentrations in transverse section of jet at $x/d_{\rm j} = 50$. Squares: mean concentration, $\bar{C}$. Crosses: mean mixed-fluid concentration, $\bar{C}_{\rm m}$, for $C > 0.01$. Triangles: peak concentration, $C_{\rm peak}$, defined as point of zero slope (for $Re_{\rm j} = 5.0$, 10, and 20×10^3), or as point of maximum negative curvature (for $Re_{\rm j} = 2.0 \times 10^3$).

4.4 Comparison with jet in quiescent reservoir

Comparison of the transverse-jet scalar PDF with the PDF of ordinary turbulent jets reveals flow-dependent differences in turbulent mixing (Figs. 4.1 and 4.5). Entrainment (engulfment of large pockets of irrotational flow species into the turbulent flow region), stirring (kinematic motion responsible for the generation of large interfacial surface area between mixing species), and molecular mixing have been viewed as the initial, intermediate, and final stages of the turbulent mixing process (Eckart 1948, Dimotakis 2000). For the transverse jet, increasing Reynolds numbers result in taller peaks in the scalar concentration PDFs, with slight shifts in preferred concentration toward lower concentrations. For the ordinary turbulent jet (Catrakis and Dimotakis 1996), peaks in the PDFs become less prominent

FIG. 4.3 The eight, six-jet-diameter-wide strips used to calculate jet-fluid-concentration PDFs in streamwise sections of transverse jet. The smaller strip at the extreme left does not contain jet fluid, and is not counted as one of the eight, $6d_j$-wide strips.

with increasing Reynolds number (Fig. 4.5). The "valley" on the low concentration side of the PDF peak fills in with increasing Reynolds number, and the preferred concentration shifts strongly toward lower concentrations.

Experiments by Smith and Mungal (1998) offer a clue to understanding the different behavior of the transverse-jet and the regular-jet PDFs. For the transverse jet, they found that mean centerline concentration in the far field decayed at a rate $s^{-2/3}$. This is slower than the s^{-1} decay rate of the ordinary jet (s is the arclength along the jet trajectory). We note that the centerline-concentration decay rate, which is calculated from ensemble-averaged images of the scalar field, is a measure of entrainment, rather than molecular mixing. The mean concentration can not distinguish between two concentration PDFs having the same first moment. Thus, although the jet-fluid concentration PDF is found to evolve with Reynolds number

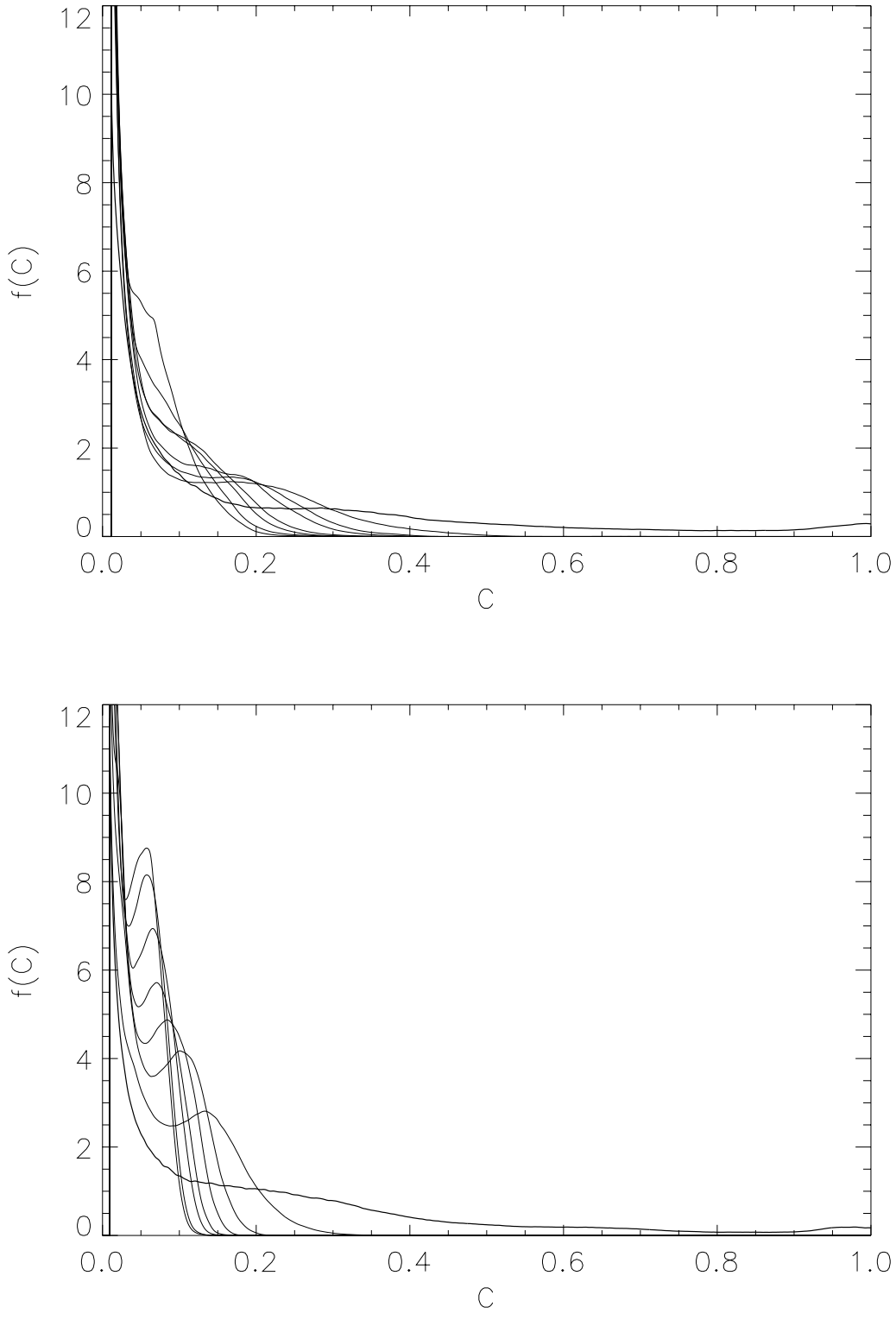

FIG. 4.4 Jet-fluid-concentration PDFs in streamwise sections (*cf.* Fig. 2.3) of transverse jet. PDFs calculated from strips shown in Fig. 4.3. Concentrations normalized by plenum-exit concentration, $C = c/c_0$. PDF of strip nearest to jet exit shows small peak near $C = 1$; PDFs shift toward lower concentrations with increasing distance from nozzle. Top: $Re_j = 1.0 \times 10^3$. Bottom: $Re_j = 10 \times 10^3$.

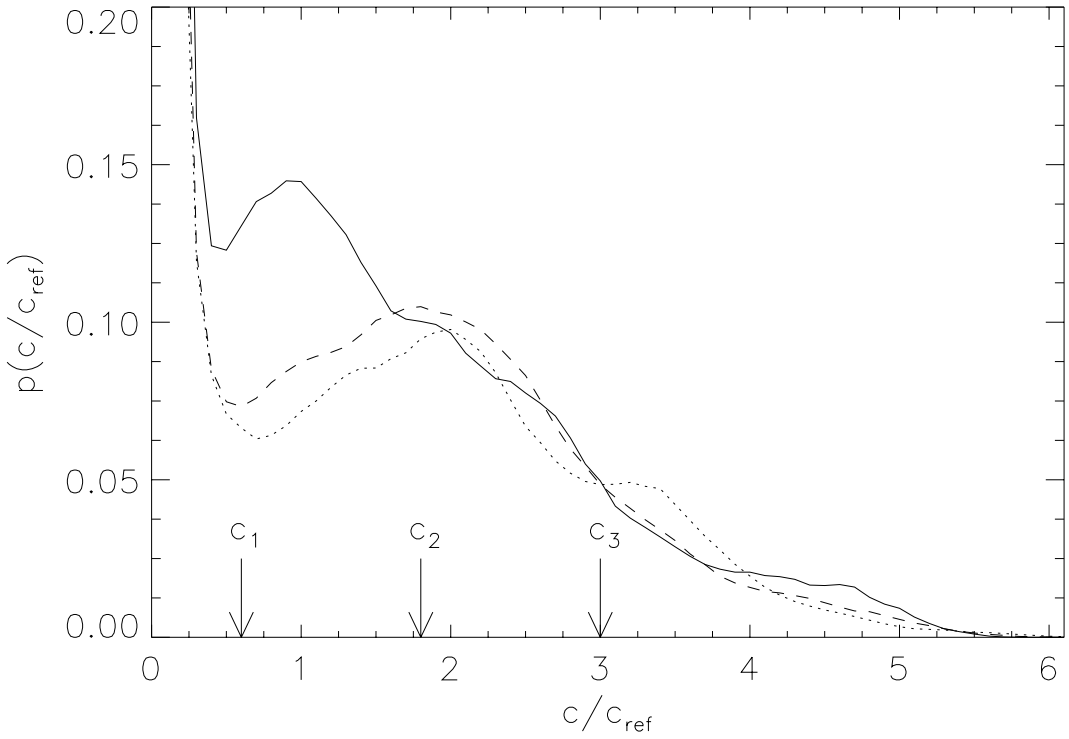

FIG. 4.5 Jet-fluid concentration PDFs for jets in a quiescent reservoir. Lines of increasing solidity denoting increasing $Re_{\rm j} = 4.5$, 9, and 18×10^3 (Catrakis and Dimotakis 1996, Fig. 8).

in the transverse jet, the mean centerline concentration decay is seen to be largely independent of Reynolds number (Fig. 3.3). We infer, based on Smith and Mungals' experiments, that the entrainment rate, relative to stirring and molecular mixing, is higher in the ordinary turbulent jet than in the far-field of the transverse jet. Thus, the transverse jet entrains less ambient fluid than the ordinary jet (as seen from the mean centerline concentration decay), but is able to homogenize entrained fluid more effectively. The growing preferred-concentration peaks in the scalar PDF suggest that, for the transverse jet at $d/d_{\rm j} = 50$, the balance between entrainment, stirring, and molecular mixing tilts toward stirring and mixing, producing better homogenization with increasing Reynolds number. In ordinary jets, the entrainment rate is higher and the balance tilts toward entrainment, with PDFs tending toward smaller peaks (and lower preferred concentrations, $C_{\rm peak}$), with increasing Reynolds number. As a result of competition between entrainment, stirring, and molecular mixing, we conclude that different mixing is possible for two very-similar turbulent flows. This is found to be the case for transverse jets and jets discharging into a

quiescent reservoir.

CHAPTER 5

Probability density function of scalar increments

A technique is introduced for whole-field measurements of scalar increments, also known as scalar differences, $\Delta_{\mathbf{r}} C \equiv C(\mathbf{x}+\mathbf{r},t) - C(\mathbf{x},t)$. The distribution of scalar increments in a variety of turbulent flows is discussed. PDFs of scalar increments for transverse jets are computed from measurements of the jet-fluid concentration field, for varying Reynolds numbers and separation distances, r. The PDFs of scalar increments for the transverse jet are normalized by their own standard deviation to compare shapes of distributions for different separation distances. Isotropy of the scalar field is assessed in terms of PDFs of scalar increments for separations in different directions. A direction-dependent scalar microscale is introduced, and computed in two orthogonal directions, to quantify the scalar-field anisotropy as a function of Reynolds number. The anisotropy is shown to be localized to specific regions of the scalar field, and an explanation is proposed.

5.1 Introduction

Scalar differences, $\Delta_r C$, also called scalar increments, are differences between simultaneous measurements of the scalar field at two points separated by distance $\mathbf{r}$ (1.1). The probability density function, $f(\Delta_{\mathbf{r}} C)$, of scalar differences expresses the probability of finding scalar concentration $C+\Delta C$ at a vector distance $\mathbf{r}$ away from a point of concentration C. Intermittency of the scalar field can be described in terms of the PDF of scalar differences as an excess of large fluctuations as compared to a Gaussian distribution (Shraiman and Siggia 2000). The n^{th}-order scalar structure functions in a turbulent flow can be expressed as moments of the PDF of scalar increments:

$$\langle [C(\mathbf{x}+\mathbf{r}) - C(\mathbf{x})]^n \rangle \;=\; \langle (\Delta_{\mathbf{r}} C)^n \rangle \;=\; \int_{-1}^{1} (\Delta_{\mathbf{r}} C)^n \, f(\Delta_{\mathbf{r}} C)\, \mathrm{d}\Delta_{\mathbf{r}} C, \tag{5.1}$$

where $0 \leq C \leq 1$.

The statistics of passive scalars and their derivatives in turbulence have been studied by numerous investigators. Probability-density functions of temperature and temperature fluctuations were measured by Alisse and Sidi (2000) in stably-stratified atmospheres, and by Jayesh and Warhaft (1992), and Tong and Warhaft (1994), in grid turbulence. Guilkey *et al.* (1997) reported on exponential-tailed scalar PDFs in turbulent-pipe-flow. Kailasnath *et al.* (1993) measured scalar concentrations (temperature and scalar-species concentration) and inferred scalar-dissipation rates, conditioned on the scalar value, for turbulent wakes, jets and boundary layers.

Statistics of temperature increments have been gathered by point measurements in a variety of flows, at low Prandtl numbers. Mydlarski and Warhaft (1998) measured spatial temperature differences in decaying grid turbulence. Ould-Rouis *et al.* (1995) reported on temporal temperature increments in a turbulent boundary layer. Antonia *et al.* (1984) conducted experiments on temperature differences on the centerline of a turbulent plane jet, and found, for this flow, reasonable agreement between the statistics of temporal and spatial temperature increments. Ching (1991) reported on the PDFs of temporal temperature differences for Rayleigh-Benard convection at the center of a helium-gas cell. Collectively, these experiments found that PDFs of passive-scalar differences behaved like an exponential, or

stretched exponential, at separations on order of the Kolmogorov scale, *i.e.*, $r \sim \lambda_K$, and tended toward Gaussian distributions for large, integral-scale separations, *i.e.*, $r \sim L$. A review of passive-scalar turbulence is given by Shraiman and Siggia (2000).

5.2 Whole-field measurement of scalar increments

Two-dimensional scalar-concentration image data (*e.g.*, Figs. 2.7 and 2.8) enable whole-field measurements, rather than point measurements, of scalar increments. To compute scalar differences, measured concentration fields are spatially shifted by a vector distance $\mathbf{r}$, and subtracted from unshifted data. As was the case for the PDF of scalar concentration (Ch. 4), up to 5.4×10^8 measurements of scalar differences are made from a total of 508 images, each (1024×1024)-pixels. Examples of the two-dimensional scalar-difference fields for horizontal (spanwise, z-axis) shifts of 2 and 16 pixels are shown in Fig. 5.1. The PDF of scalar increments is computed from histograms of the scalar-difference field, conditioned on the intersection between the shifted and unshifted image data (the extent of the jet is defined by a scalar threshold). This condition on the PDF is equivalent to requiring two, spatially-separated measurement points to both be within the instantaneous body of the jet. Without the condition, the PDF would be dominated by the difference between the jet and the dark, $C = 0$, portions of the image. The unconditional PDF of scalar differences would thus approach the jet-fluid concentration PDF, and its reflection about the line $\Delta_r C = 0$ (the vertical axis), in the limit of large separations $r \geq L$. Thus, a condition on the PDF is necessary because of the spatial confinement and inhomogeneity of the transverse-jet concentration field.

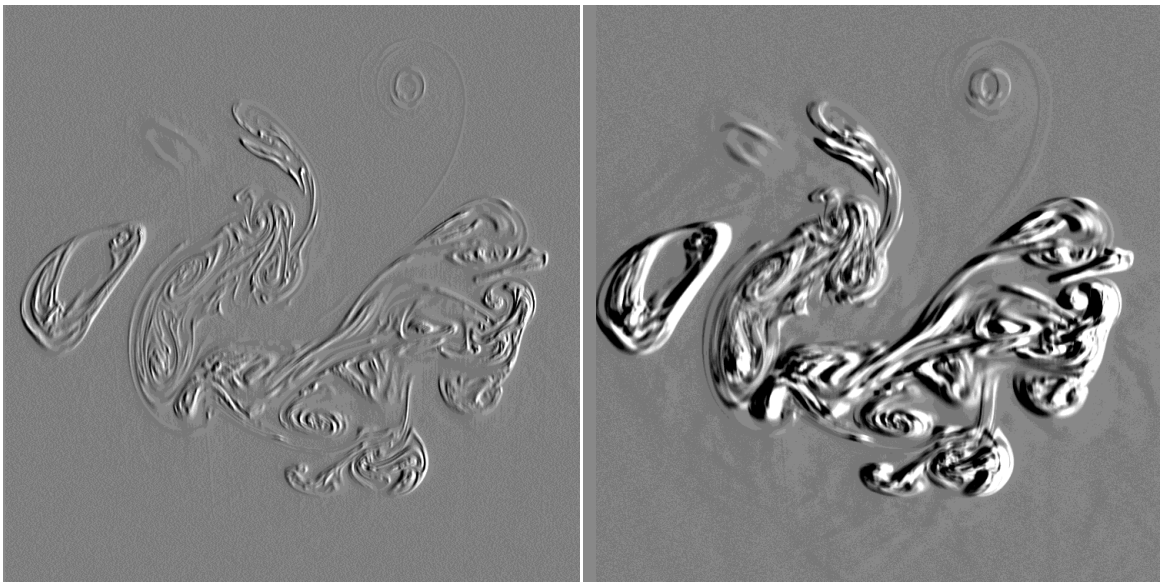

FIG. 5.1 Jet-fluid concentration difference. Left: Horizontal (z-axis) shift of 2 pixels. Right: Horizontal shift of 16 pixels.

5.3 Scalar increments

Conditional PDFs of scalar increments for horizontal (spanwise, z-axis) separations of $\mathbf{r} = 2\,\widehat{\mathbf{z}},\ 4\,\widehat{\mathbf{z}},\ 16\,\widehat{\mathbf{z}},\ 64\,\widehat{\mathbf{z}}$, and $128\,\widehat{\mathbf{z}}$ pixels are shown in Fig. 5.2. The PDFs of scalar increments were computed from jet-fluid concentration fields at $x/d_\mathrm{j} = 50$ for $Re_\mathrm{j} = 2.0 \times 10^3$ and 20×10^3. The distributions are nearly symmetric, as would be expected for statistically-converged measurements. At jet Reynolds number 20×10^3, the small separations ($r = 2$, 4 pixels) show exponential-tailed distributions of scalar increments (straight lines on the log-linear plot). In Ch. 4, the Kolmogorov scale was estimated to be 0.89 pixels for $Re_\mathrm{j} = 20 \times 10^3$. As separations become substantially larger than the Kolmogorov scales and approach inertial and integral scales, the shoulders of the distribution broaden, and the tails drop. Others have reported Gaussian PDFs for large separation distances (*e.g.*, Ching 1991). Decreasing probability for fluid of similar concentration, *i.e.*, smaller $f(\Delta_\mathbf{r} C = 0)$, is seen with increasing separation distance. For low Reynolds numbers, $Re_\mathrm{j} = 2.0 \times 10^3$, the shoulders of the PDF of scalar increments, $f(\Delta_\mathbf{r} C)$, again broaden with increasing separation distance, r; however, the tails of the PDFs for small separations are no longer strictly exponential but rather stretched exponential. For reference, the Kolmogorov scale for $Re_\mathrm{j} = 2.0 \times 10^3$ was estimated to be

5.0 pixels in Ch. 4. The relevant scalar-diffusion scales, $\lambda_{\mathcal{D}}$, are 3 and 0.5 pixels, for $Re_{\rm j} = 2.0 \times 10^3$ and 20×10^3, respectively.

5.4 Standard-deviation-normalized scalar increments

Probability density functions are normalized by their own standard deviation to compare shapes of distributions. Figure 5.3 shows the PDF of scalar increment, $f(\Delta_{\mathbf{r}}C/\langle(\Delta_{\mathbf{r}}C)^2\rangle^{1/2})$, as a function of normalized separation distance. The separation distance, $\mathbf{r}$, is normalized by the square root of the variance, $\langle(\Delta_{\mathbf{r}}C)^2\rangle^{1/2}$. For the range of Reynolds numbers studied, the normalized PDFs show wider exponential tails with decreasing separation distance. An excess of large and small concentration differences is seen, relative to a Gaussian distribution of the same variance. This is a hallmark of the intermittency of the scalar field (Shraiman and Siggia 2000). This intermittency of the transverse-jet scalar field is apparent when the PDFs are based on the normalized scalar difference $\Delta_{\mathbf{r}}C/\langle(\Delta_{\mathbf{r}}C)^2\rangle^{1/2}$.

5.5 Anisotropy of scalar increments

Anisotropy of the jet-fluid-concentration field at small scales, which was seen in the 2-D scalar power spectra of Fig. 3.4, is also evident in comparing PDFs of scalar increments for vertical (y-axis) and horizontal (z-axis) separations. Figure 5.4 shows the PDF of scalar differences in the cross-section of the transverse jet for separations of $\mathbf{r} = 2\,\widehat{\mathbf{y}}$ pixels and $\mathbf{r} = 2\,\widehat{\mathbf{z}}$ pixels. The narrower width of the PDF for a vertical separation of 2 pixels, relative to a horizontal separation of 2 pixels, indicates that the scalar field is anisotropic for small separation distances, r. In particular, the scalar field has less variation (in terms of the width of the PDF of scalar increments and all higher moments) in the vertical direction than in the horizontal direction. Scalar-field anisotropy, seen in the difference in the PDFs between 2-pixel vertical and horizontal shifts, is less evident for the larger separation distance of 16 pixels (Fig. 5.4). This result is consistent with the 2-D scalar power spectra (Fig. 3.4), which are more-nearly axisymmetric at low wavenumbers and increasingly elliptical with increasing wavenumber. The (in-plane) anisotropy of small scales, and near

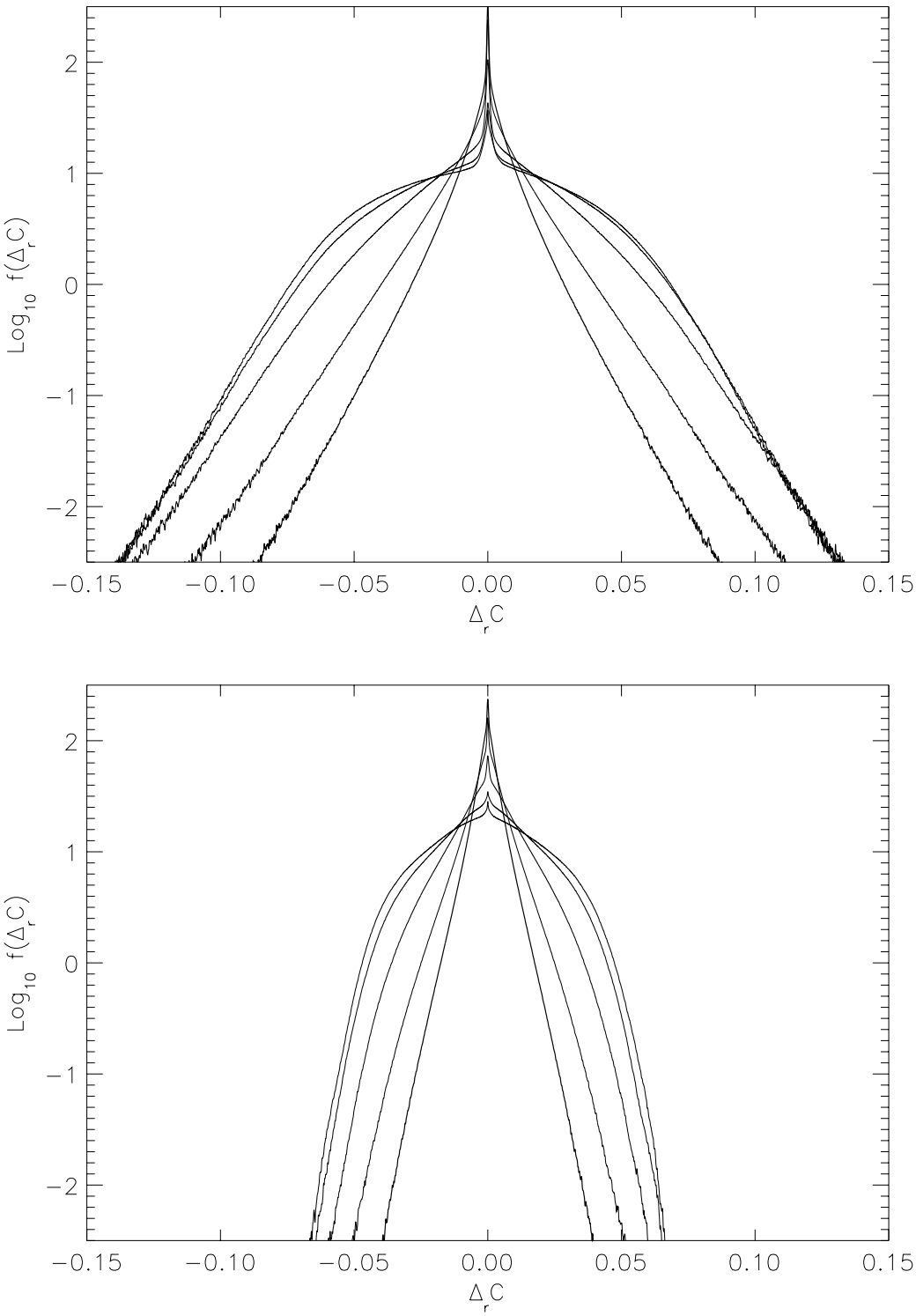

FIG. 5.2 PDFs of scalar increments at $x/d_{\rm j} = 50$ for horizontal separations of $\mathbf{r} = 2\,\widehat{\mathbf{z}},\ 4\,\widehat{\mathbf{z}},\ 16\,\widehat{\mathbf{z}},\ 64\,\widehat{\mathbf{z}}$, and $128\,\widehat{\mathbf{z}}$ pixels. Innermost, triangular PDF is for smallest separation distance, while outermost, broad-shouldered PDF is for largest separation. For comparison, the scalar diffusion scales for the $Re_{\rm j} = 2.0 \times 10^3$ and 20×10^3 jets are 3 and 0.5 pixels, respectively. Top: $Re_{\rm j} = 2.0 \times 10^3$. Bottom: $Re_{\rm j} = 20 \times 10^3$.

isotropy of the large scales, is not only a low-Reynolds-number result, but persists to the highest Reynolds number investigated, $Re_j = 20 \times 10^3$ (Fig. 5.5). The anisotropy of small scales appears to decrease with increasing Reynolds number. More evidence of this will be seen in Sec. 5.6.

Anisotropy of small scales is also visually apparent in images of the jet-fluid concentration difference. Figure 5.6 compares scalar-difference fields for a horizontal shift of $\mathbf{r} = 2\widehat{\mathbf{z}}$ pixels and a vertical shift of $\mathbf{r} = 2\widehat{\mathbf{y}}$ pixels. Both images use the same (linear) intensity scaling for scalar concentration. The occurrence of large scalar differences, shown as purely black or white features in the scalar-increment field, is more prominent and frequent for the horizontal separations than for the vertical ones. This difference in contrast indicates that scalar structure is preferentially oriented in the vertical (y-axis) direction, and that scalar gradients are larger horizontally than vertically. Small-scale anisotropy of the scalar field is particularly apparent near the vertical centerline, and in the "finger" extending upwards at the top of the jet. The location of these small, vertically-oriented structures suggest that they are produced by the mean strain field of the dominant, counter-rotating vortex pair.

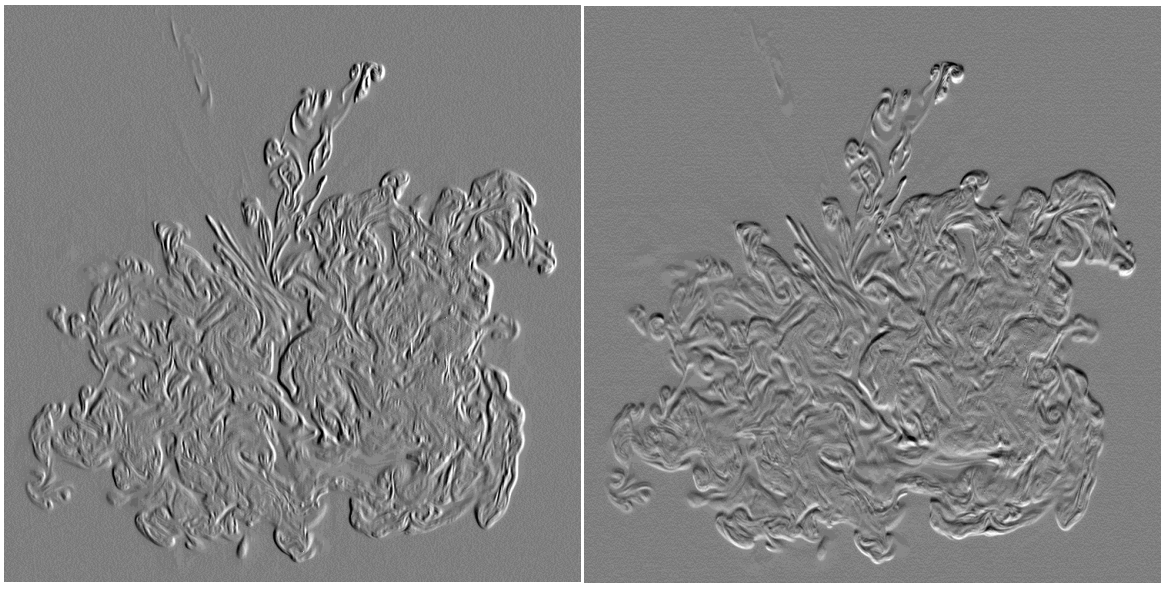

FIG. 5.6 Jet-fluid concentration difference for $Re_j = 10 \times 10^3$. Left: Horizontal shift of $\mathbf{r} = 2\,\widehat{\mathbf{z}}$ pixels. Right: Vertical shift of $\mathbf{r} = 2\,\widehat{\mathbf{y}}$ pixels. Same intensity scaling used to display both images.

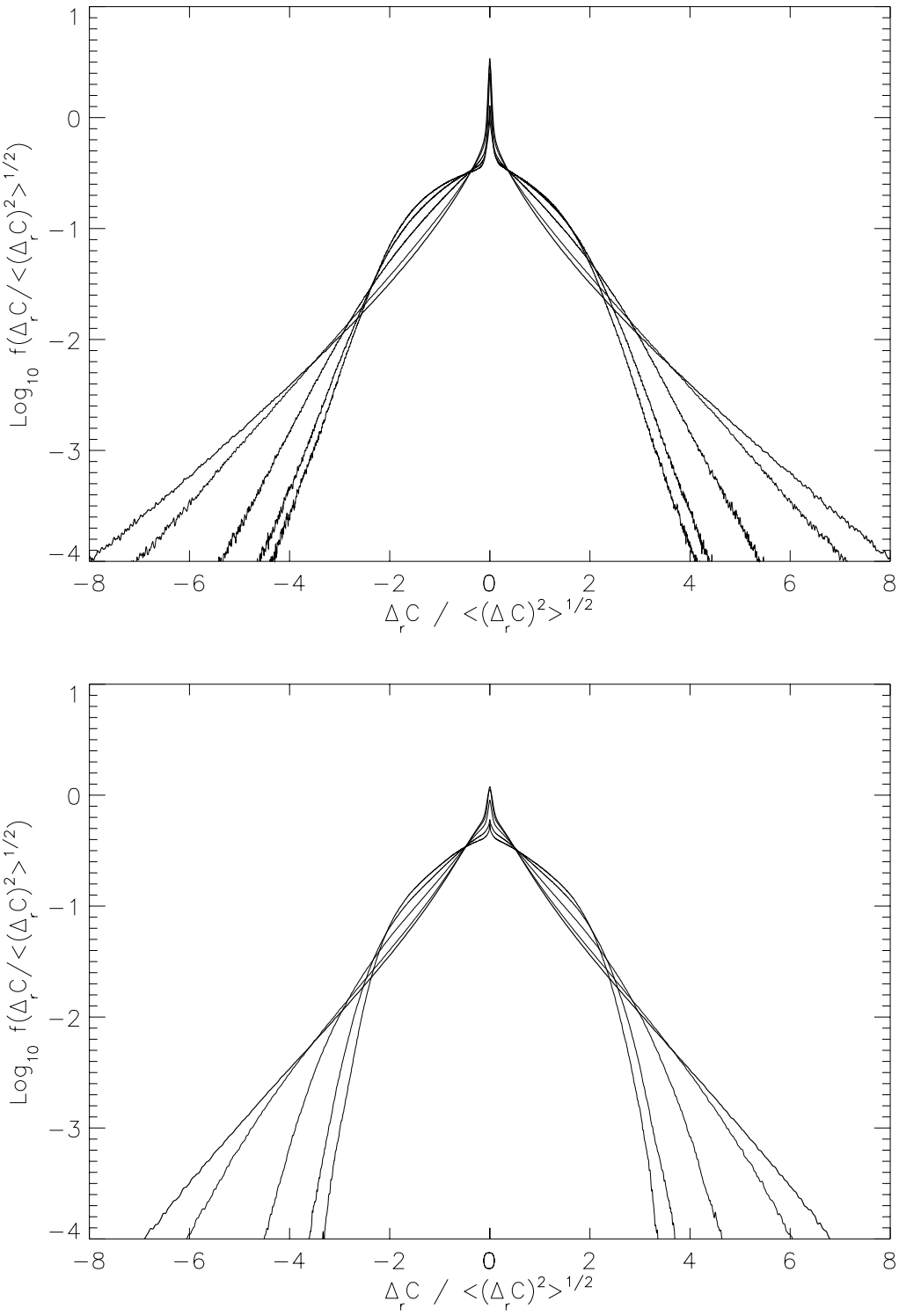

FIG. 5.3 PDFs of standard-deviation-normalized scalar increments at $x/d_{\rm j} = 50$ for horizontal separations of $\mathbf{r} = 2\,\widehat{\mathbf{z}}$, $4\,\widehat{\mathbf{z}}$, $16\,\widehat{\mathbf{z}}$, $64\,\widehat{\mathbf{z}}$, and $128\,\widehat{\mathbf{z}}$ pixels. Concentration difference normalized by square root of the variance for each PDF. Outermost, triangular PDF is for smallest separation distance, while innermost PDF is for largest separation. Top: $Re_{\rm j} = 2.0 \times 10^3$. Bottom: $Re_{\rm j} = 20 \times 10^3$.

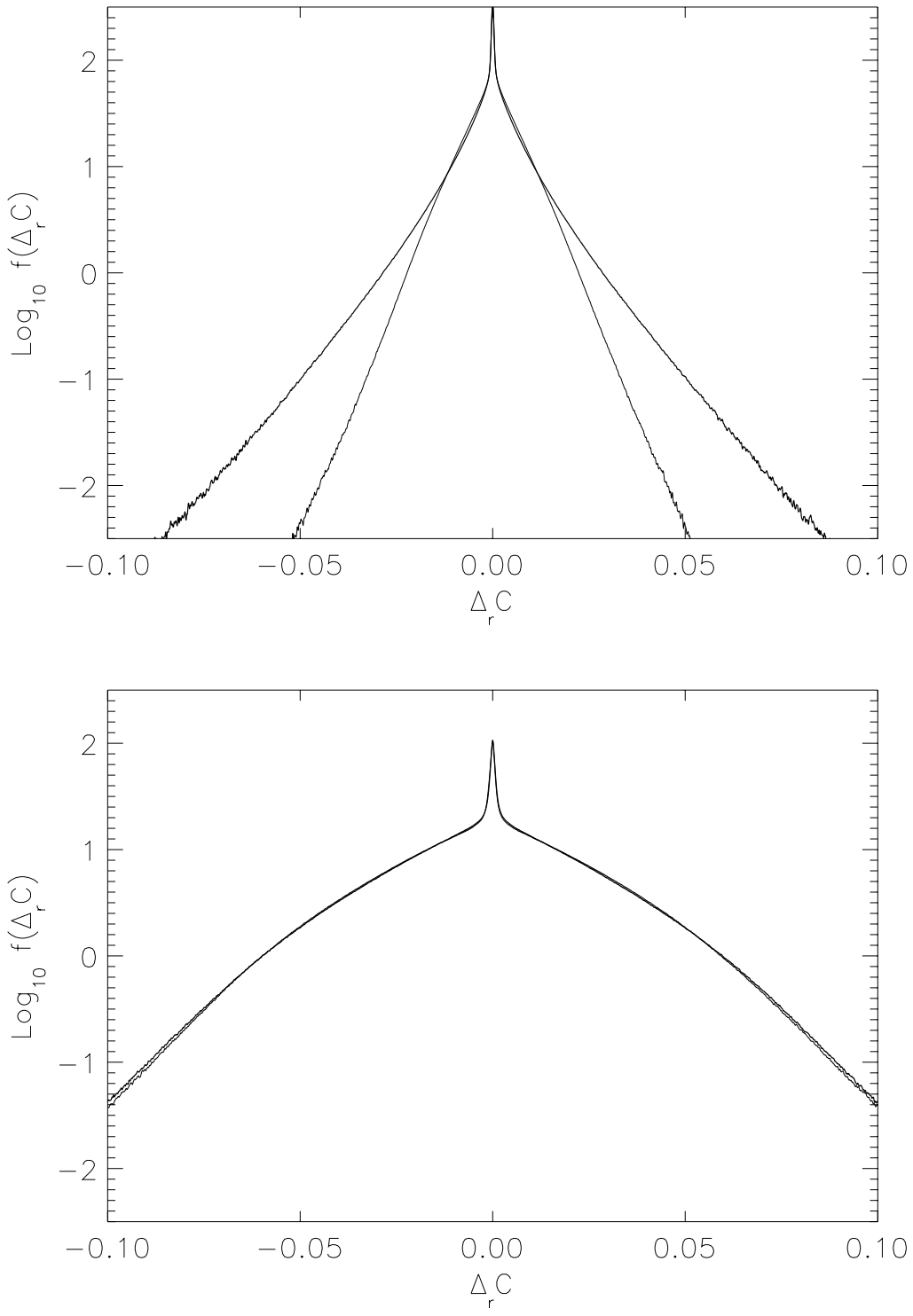

FIG. 5.4 PDFs of scalar increments for horizontal (z-axis) and vertical (y-axis) shifts. $Re_{\rm j} = 2.0 \times 10^3$ and $x/D = 50$. Top: Outer PDF is for horizontal separations of $\mathbf{r} = 2\,\widehat{\mathbf{z}}$ pixels and inner PDF is for vertical separations of $\mathbf{r} = 2\,\widehat{\mathbf{y}}$ pixels. Bottom: $\mathbf{r} = 16\,\widehat{\mathbf{y}}$ pixels and $\mathbf{r} = 16\,\widehat{\mathbf{z}}$ pixels.

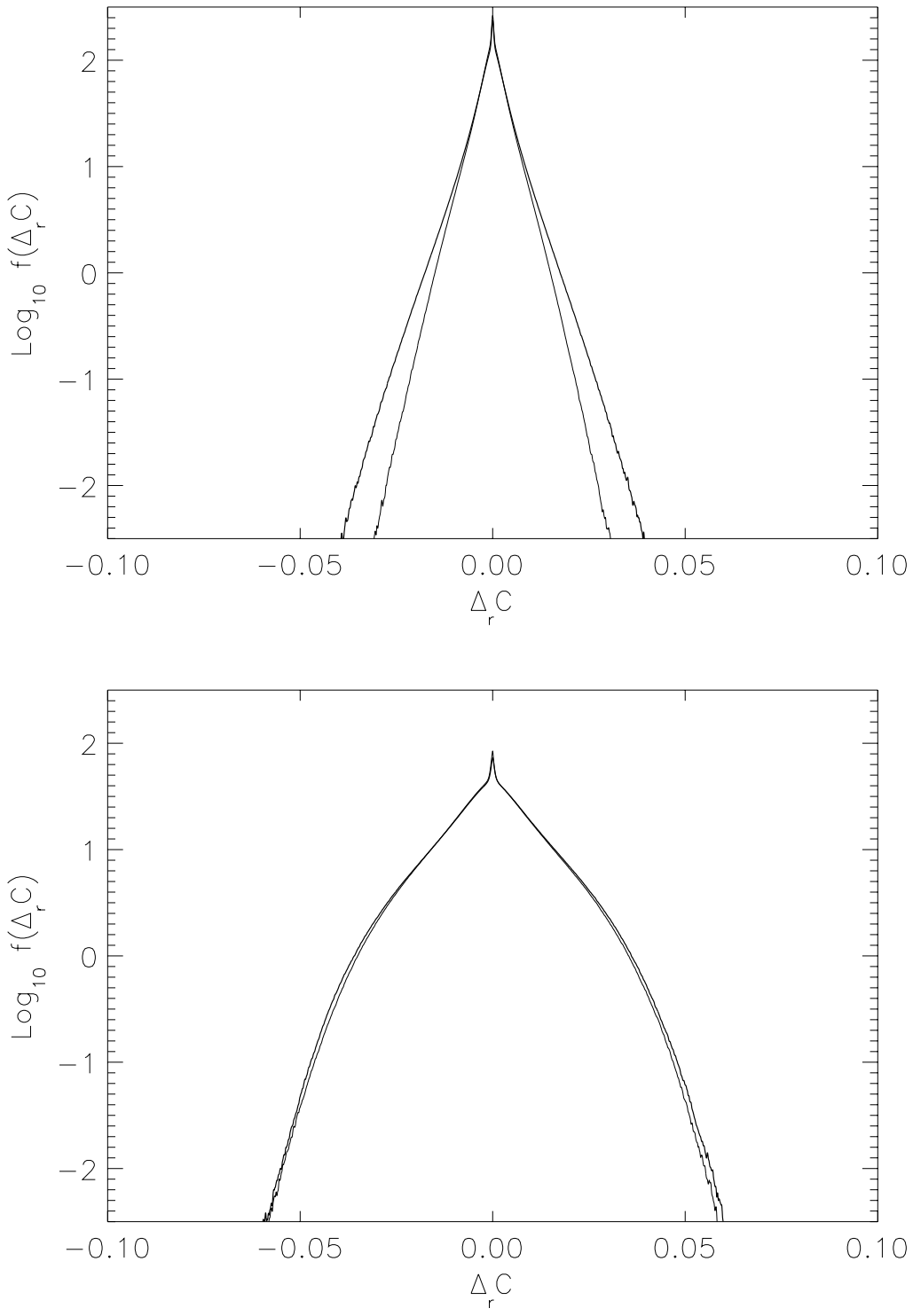

FIG. 5.5 Same as Fig. 5.4, but for $Re_{\rm j} = 20 \times 10^3$. Top: Outer PDF is for horizontal separations of $\mathbf{r} = 2\,\widehat{\mathbf{z}}$ pixels and inner PDF is for vertical separations of $\mathbf{r} = 2\,\widehat{\mathbf{y}}$ pixels. Bottom: $\mathbf{r} = 16\,\widehat{\mathbf{y}}$ pixels and $\mathbf{r} = 16\,\widehat{\mathbf{z}}$ pixels.

5.6 Microscale for scalars

A microscale for scalar fluctuations may be defined analogously to the Taylor microscale for velocity fields. For an isotropic scalar field, the scalar microscale, λ_C, can be defined as (Tennekes and Lumley 1972, Cook and Dimotakis 2000):

$$\lambda_C^2 \equiv \frac{\left\langle C'^2 \right\rangle}{\left\langle \left(\frac{\partial C'}{\partial x}\right)^2 \right\rangle}, \tag{5.2a}$$

To generalize to an anisotropic field, the scalar microscale, $\lambda_{C,i}$, in a given direction, x_i, is defined as

$$\lambda_{C,i}^2 \equiv \frac{\left\langle C'^2 \right\rangle}{\left\langle \left(\frac{\partial C'}{\partial x_i}\right)^2 \right\rangle}. \tag{5.2b}$$

The variance of the scalar fluctuations, $< C'^2 >$, may be expressed as the second moment of the PDF of the scalar field, $f(C)$,

$$\left\langle C'^2 \right\rangle = \left\langle (C - \bar{C})^2 \right\rangle = \int_0^1 (C - \bar{C})^2 \, f(C) \, \mathrm{d}C. \tag{5.3}$$

Equation 5.3 can be used to compute the variance, $< C'^2 >$, from the PDF of concentration, $f(C)$. Similarly, we write the variance of the scalar partial derivatives, $< (\frac{\partial C'}{\partial x_i})^2 >$, as

$$\left\langle \left(\frac{\partial C'}{\partial x_i}\right)^2 \right\rangle = \int_{-\infty}^{\infty} \left(\frac{\partial C'}{\partial x_i}\right)^2 f\left(\frac{\partial C'}{\partial x_i}\right) \mathrm{d}\left(\frac{\partial C'}{\partial x_i}\right), \tag{5.4}$$

no sum on i. The spatial partial derivatives $\frac{\partial C'}{\partial x_i}$ are estimated from the PDF of scalar increments by noting that

$$\frac{\partial C'}{\partial x_i} = \lim_{r \to 0} \frac{C(x_i + r) - C(x_i)}{r} = \lim_{r \to 0} \frac{-\Delta_{\mathbf{r}} C}{r} \simeq \frac{-\Delta_{\mathbf{r}} C}{r}, \tag{5.5a}$$

for small separation distances, r. In this case, we estimate $\frac{\partial C'}{\partial z}$ and $\frac{\partial C'}{\partial y}$ as

$$\frac{\partial C'}{\partial x_i} \simeq -\frac{\Delta_{x_i} C}{x_i} = -\frac{1}{2} \Delta_{x_i} C \tag{5.5b}$$

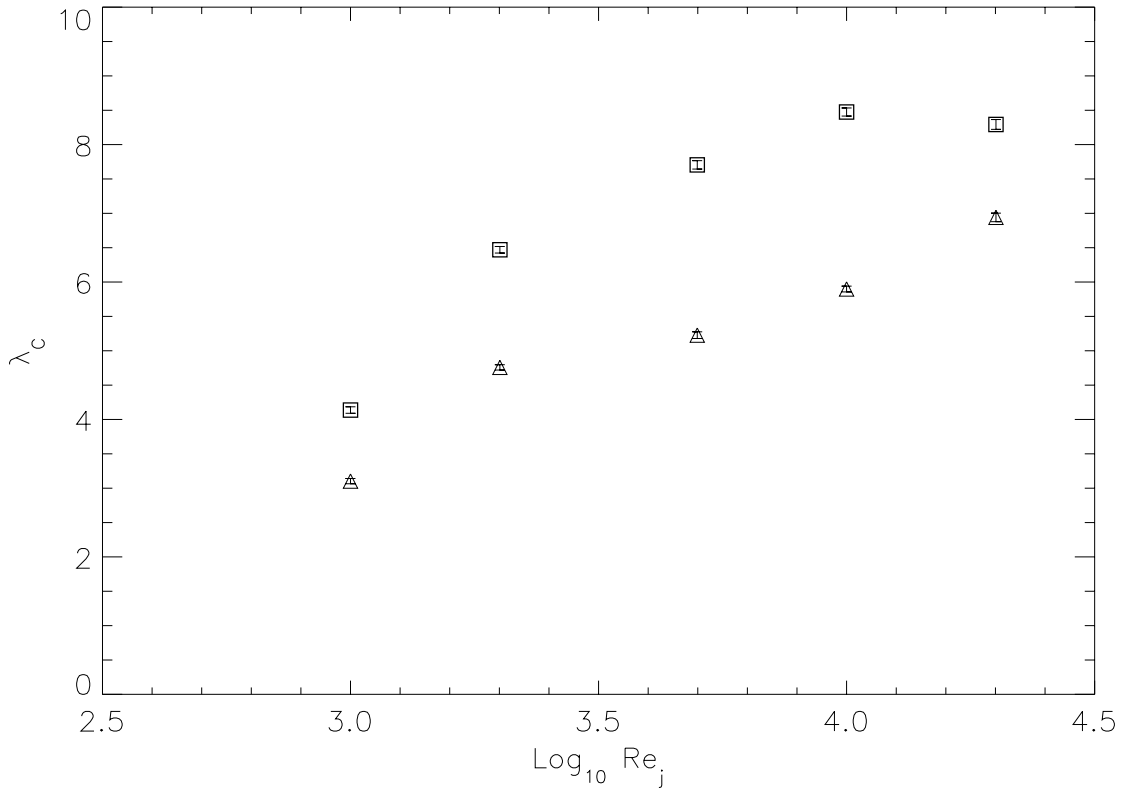

FIG. 5.7 Scalar microscale at $x/d_j = 50$ as a function of jet Reynolds number. Error bars smaller than plot symbols in all cases. Length scale is pixels. Squares: Microscale in the vertical, y, direction. Triangles: Microscale in the horizontal, z, direction.

for horizontal shifts of $2\,\widehat{\mathbf{z}}$ pixels, and vertical shifts of $2\,\widehat{\mathbf{y}}$ pixels, respectively.

The scalar microscale in each direction for the transverse-jet scalar field is computed from PDFs of concentration and PDFs of scalar increment. Horizontal and vertical microscales are computed for each image, and the mean microscales at each Reynolds number are found by ensemble averaging over 508 realizations. Figure 5.7 shows the scalar microscales for $Re_j = 1.0$, 2.0, 5.0, 10, and 20×10^3. The scalar microscale in the vertical, y, direction is seen to be consistently larger than the microscale in the horizontal, z, direction. This evidence of longer length scales in the vertical direction, as compared to the horizontal direction, is consistent with the results of the two-dimensional power spectra, and the directional PDF of scalar increments. The ratio of the horizontal microscales to the vertical microscales is

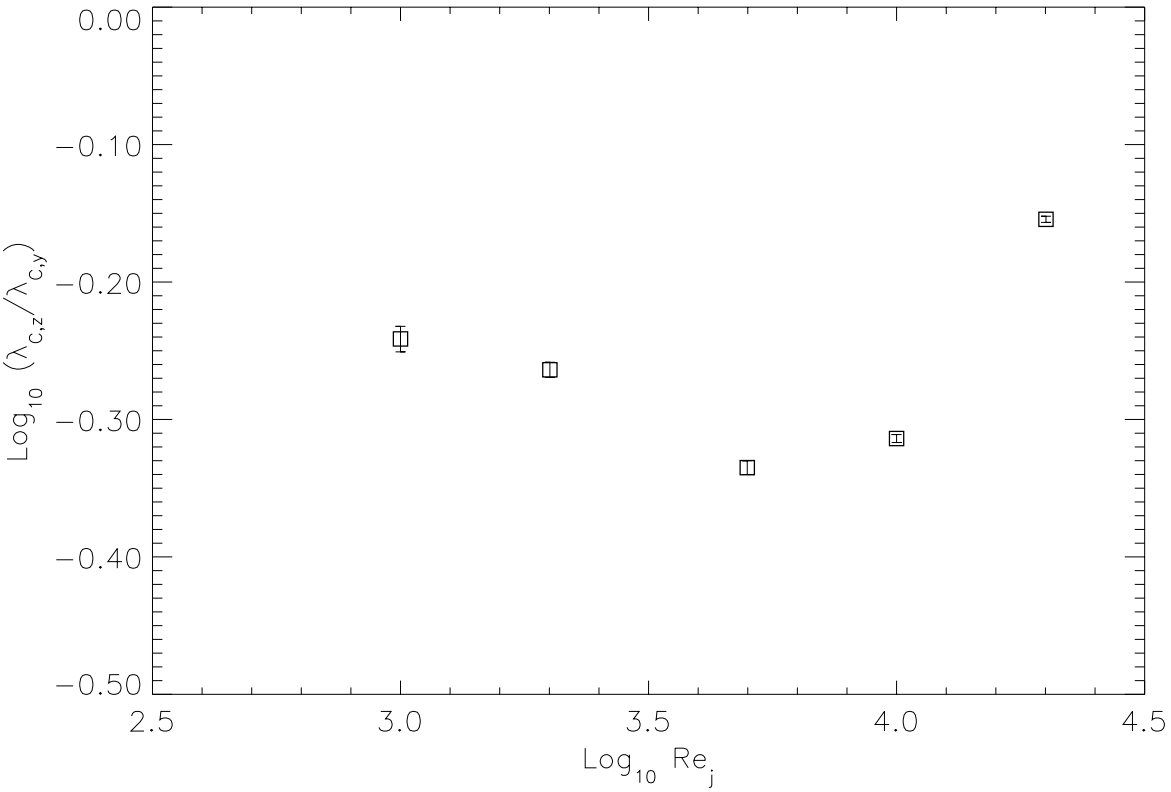

FIG. 5.8 Ratio of horizontal to vertical scalar microscales. Error bars smaller than plot symbols in all but lowest Reynolds number case.

plotted in Fig. 5.8 as a function of Reynolds number. The anisotropy of the scalar microscale is found to increase slightly with increasing Reynolds number, and then decrease for jet Reynolds numbers greater than approximately 10×10^4. In the limit of high Reynolds numbers, the scalar microscale, referenced to the outer scale, is expected to decrease as the square-root of the local (outer) Reynolds number. In these experiments, the scalar microscale is found to increase with Reynolds number up to $Re_\mathrm{j} = 10 \times 10^4$. The data for $Re_\mathrm{j} = 20 \times 10^4$ suggest that the scalar microscale begins to decrease with further increases in Reynolds number. However, in order to draw firm conclusions about the asymptotic behavior of the scalar microscale, even higher Reynolds numbers would be required. We note that the local Reynolds number, $Re_\Gamma(x)$, is approximately 0.6 times the jet Reynolds number Re_j, for velocity ratio $V_\mathrm{r} = 10.1$ and $x/d_\mathrm{j} = 50$ (Ch. 2).

The precision in determining the mean scalar microscales, $\lambda_{C,z}$ and $\lambda_{C,y}$, is

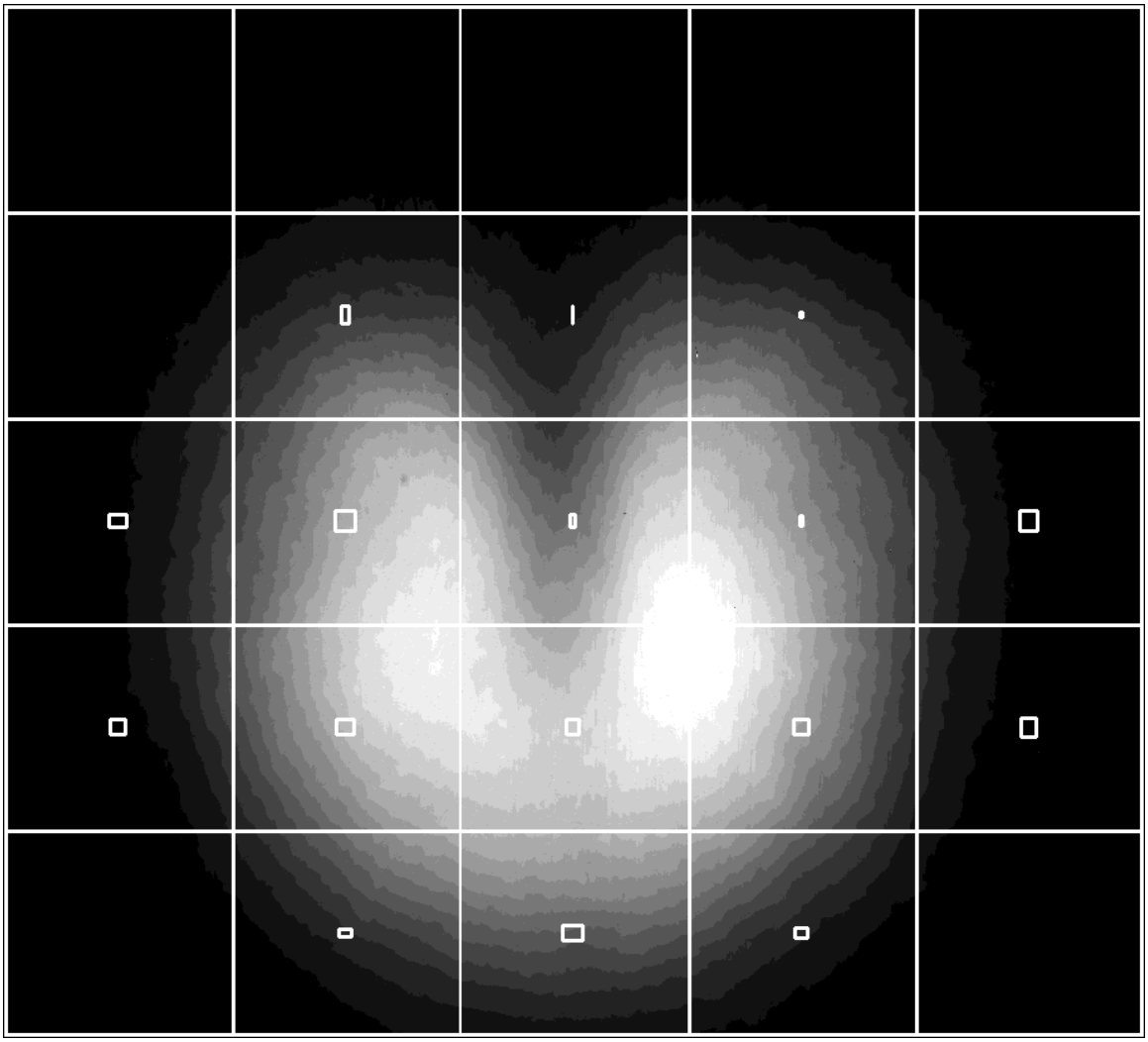

FIG. 5.9 Localized scalar microscale superimposed upon the mean scalar field, for $Re_{\rm j} = 20 \times 10^3$. Microscales are ensemble averaged over 508 images, in each rectangular section shown. Horizontal and vertical dimensions of the rectangles are $2\lambda_{C,z}$ and $2\lambda_{C,y}$, respectively.

indicated by the error bars in Fig. 5.7. The error bars, which are of size equal to two standard deviations of the microscales, are less than the size of the plot symbols. The standard deviation of the mean is computed as

$$\sigma_{<\lambda_{C,i}>} \equiv \sqrt{\frac{1}{N(N-1)} \sum_{n=1}^{N} \left(\lambda_{C,i} - \langle \lambda_{C,i} \rangle\right)^2}, \tag{5.6}$$

where N = 508 (the number of images at each Reynolds number), and $< \lambda_{C,i} >$ is the mean microscale length. Error bars for the ratio of horizontal-to-vertical length scales, $< \lambda_{C,z} > / < \lambda_{C,y} >$, are computed in the same way. For all but the lowest Reynolds number ($Re_{\mathrm{j}} = 1.0 \times 10^3$), the error bars for the anisotropy ratio are smaller than the size of the plot symbols. The error bars on the mean microscales, $\lambda_{C,i}$, and the mean anisotropy ratio, $< \lambda_{C,z} > / < \lambda_{C,y} >$, are an indication of the precision, rather than the accuracy, of the measurement.

The global dynamics of the transverse jet are believed to be responsible for the observed anisotropy of the scalar field at small scales. The counter-rotating vortex pair which dominates the flow in the far field of the transverse jet induces a vertically-aligned mean strain field. This mean strain field acts on the scalar field to produce thin, vertical filaments, or "fingers," in the wake of the jet. As a result, the anisotropy is localized to specific regions of the transverse jet. Figure 5.9 shows the scalar microscale computed in small sections of the transverse jet. Rectangles representing the microscales are superimposed on an image of the ensemble-averaged, jet-fluid-concentration field at $x/d_{\mathrm{j}} = 50$, for $Re_{\mathrm{j}} = 20 \times 10^3$. The rectangles have horizontal and vertical dimensions corresponding to $2\lambda_{C,z}$ and $2\lambda_{C,y}$, respectively. The anisotropy of the scalar fluctuations is seen to be greatest in the upper half of the image, particularly in the region between the vortex centers. This is precisely the area where extensional strain is produced by the counter-rotating vortex pair. We conclude that anisotropic, large-scale flow can impose itself on the small-scale features of the scalar field. Thus, a scalar field can be anisotropic at small scales, even if the small-scale velocity field is isotropic.

CHAPTER 6

Generalized coverage statistics for anisotropic sets

Fractals, and scale-dependent coverage statistics, for self-similar geometric surfaces are reviewed. We introduce generalized coverage statistics suitable for anisotropic, non-self-similar geometries. This generalized coverage counting involves covering with parallelepipeds of varying sizes and aspect ratios. For curves embedded in two dimensions, the generalized coverage count, $N(\lambda_1, \lambda_2)$, is a function of two variables. A scale-dependent measure, $\beta(\lambda)$, of the anisotropy of a set is introduced. It is shown that $\beta(\lambda)$ transforms the coverage count, $N(\lambda_1, \lambda_2)$, to isotropy through a scale-dependent normalization of the coordinates. Examples of generalized coverage statistics are given for a simple rectangular perimeter, and an anisotropic Sierpinski carpet. The anisotropy of the set is measured in each case.

6.1 Introduction

The term "fractal" was coined by Mandelbrot (1975) to describe complicated geometric figures having repeated features at different length scales, *i.e.*, self-similarity, or scale-invariance. This symmetry across scales, and lack of characteristic length, yields shapes that are more complicated than ordinary geometric figures, such as lines, (Euclidean dimension $D_{\rm E} = 1$), squares ($D_{\rm E} = 2$), and cubes ($D_{\rm E} = 3$). Fractal geometries are non-rectifiable, having "lengths," "areas," or "volumes" that depend on the resolution of the measurement (Richardson 1961). For instance, the coverage length of a fractal curve embedded in a plane increases without limit as scale is decreased. Mandelbrot recognized that the geometric complexity of these self-similar objects could be characterized by a non-integral dimension defined by Hausdorff (1919).

Consider a geometric figure (set), A, embedded in d-dimensional space. Cover the set with d-spheres of variable radius $r_i \leq \epsilon$ and define the function,

$$H_{\alpha,\epsilon}(A) = \inf \sum_{\rm i} {\rm r_i}^{\alpha},$$

where the summation is over all spheres required to cover A. The Hausdorff measure, $H_\alpha(A)$, which is suited for fractal geometries, is defined as the smallest-possible sum, for $\epsilon \to 0$, of the α-dimensional volume of the coverage spheres:

$$H_\alpha(A) = \lim_{\epsilon\to 0} H_{\alpha,\epsilon}(A) = \lim_{\epsilon\to 0} \inf \sum_{\rm i} {\rm r_i}^{\alpha}.$$

The Hausdorff measure has the property that there exists a critical value of $\alpha = D_{\rm H}$ such that

$$H_\alpha(A) = \infty \ \text{ for } \ \alpha < {\rm D_H}$$

and

$$H_\alpha(A) = 0 \ \text{ for } \ \alpha > {\rm D_H}.$$

This defines $D_{\rm H}$, the Hausdorff dimension of A. The Hausdorff dimension is non-integer for fractal geometries, and reduces to the Euclidean dimension for simple figures.

The capacity, or coverage, dimension is another way of defining a non-integral dimension that is related, and usually equal, to the Hausdorff dimension, although counterexamples exist (Cross 1999). Consider coverage of a set A in d-dimensional space with equal-sized d-spheres of radius $r = \epsilon$, and count the number of d-spheres containing points in A. The capacity is defined as

$$D_C = \lim_{\epsilon \to 0} \frac{\log N(\epsilon)}{\log(\epsilon^{-1})},$$

where $N(\epsilon)$ is the number of spheres needed to cover the given set. In order for the capacity to be constant, the coverage count must be a power-law function of the measurement scale, λ, *i.e.*, $N(\lambda) \propto \lambda^{-D_C}$. This behavior was termed "power-law fractal" by Miller and Dimotakis (1991). For box-counting, the equal-sized d-spheres are replaced by d-cubes of size ϵ. The box-counting method lends itself readily to computation and is a particularly-convenient definition of fractal dimension for experimental datasets.

A generalized fractal geometry that depends on the scale of observation was introduced by Takayasu (1989), and independently suggested by Miller and Dimotakis (1991), on the basis of their experimental data, and Dimotakis (1991), on the basis of scaling arguments. Within this scale-dependent framework, the coverage dimension, D_C is, in general, a function of scale λ,

$$D_C(\lambda) = \frac{\mathrm{d} \log N(\lambda)}{\mathrm{d} \log(\lambda^{-1})}. \tag{6.1}$$

Power-law fractals, where D_C is a constant, are seen to be a special case of the scale-dependent geometry. The scale-dependent coverage dimension is related to a distribution of geometric scales, in particular the probability density distribution of "largest-empty-box scales" (Catrakis and Dimotakis 1996). From experimental measurements of jet-fluid concentration in jets discharging into a quiescent reservoir, Catrakis and Dimotakis (1996) found that the coverage dimension of two-dimensional isosurfaces increased monotonically with increasing scale, varying smoothly from near unity at smallest scales to 2 at largest scales.

6.2 Generalized coverage for anisotropic sets

For self-similar geometries, it is natural to consider the statistics of covering a set with d-dimensional spheres or cubes, and to define the coverage dimension based upon the coverage count, $N(\lambda)$. However, many natural phenomena are not isotropically scale invariant and thus are not readily addressed within the framework of isotropic fractal geometry. Self-affine sets, for instance, become self-similar upon anisotropic rescaling by an affine transformation, $\mathbf{S}$. Affine transformations are a combination of translation, rotation, dilation, and possibly reflection. Such transformations, $\mathbf{S}: \mathbf{R}^d \rightarrow \mathbf{R}^d$, may be expressed as

$$\mathbf{S}(A) = \mathbf{T}(A) + \mathbf{b},$$

where $\mathbf{T}$ is a linear transformation on A, and $\mathbf{b}$ is a vector, in the space $\mathbf{R}^d$. In general, affine transformations can contract or expand by differing amounts in different directions. Self-similar sets are a special case of self-affine sets.

Falconer (1990) reported that ferns and grasses are well-represented by self-affine sets. Fracture in geologic materials important for oil and gas recovery have been found to be self-affine fractals (Drazer and Koplik 2000). Vicsek *et al.* (1990) found self-affine shapes of bacterial colonies when growth was initiated from a straight line segment in an agar plate. Thin films grown in a vacuum are self-affine surfaces when the process of deposition is realized at low temperature and the angle of incidence is non-normal to the substrate (Pfeifer *et al.* 1989, Vicsek *et al.* 1990). Vicsek (1990) argues that, in general, self-affine geometries may be produced by marginally-stable growth of interfaces, in which fluctuations (which would die out for stable interfaces, and grow exponentially for unstable interfaces) can persist for long times.

Anisotropic driving forces can also introduce a preferred direction in the growth of complex interfaces. In Rayleigh-Taylor unstable flows, for instance, a constant acceleration (*i.e.*, gravity) drives the growth of the mixing zone in one direction. Additional (horizontal) small scales of the interface are generated as a consequence of secondary, Kelvin-Helmholtz instabilities of the vertical shear layers produced by the Rayleigh-Taylor instability (Cook and Dimotakis 2000). Self-similar fractal

geometric descriptions may be inadequate for Rayleigh-Taylor unstable interfaces because of the existence of different characteristic length scales in different directions.

In turbulence, local isotropy does not appear to hold in general for scalar fields. For instance, Sreenivasan (1991) argues that small-scale scalar fields can be directly influenced by anisotropic large-scale motions, and thus might be more anisotropic than the small-scale velocity field. As seen in two-dimensional scalar power spectra (Ch. 3), the directional PDF of scalar increments (Ch. 5), and the scalar microscales in two directions (Ch. 5), the scalar field of the transverse-jet is anisotropic, particularly at small length scales.

We introduce generalized coverage statistics for anisotropic sets by considering coverages with anisotropic, d-dimensional ellipses or parallelepipeds. In two dimensions, consider covering a plane curve, *e.g.*, an iso-concentration contour in a 2-D concentration field, with rectangles of size $\lambda_1 \times \lambda_2$. The generalized coverage counts, $N(\lambda_1, \lambda_2)$, are functions of two variables and may be viewed as contour plots in a [$\log(\lambda_1)$, $\log(\lambda_2)$]-plane. Coverage counts with high-aspect-ratio rectangles lie close to the axes of such contour plots. Box-coverage counting, which is used for isotropic, self-similar sets, is a special case of the generalized coverage count. Ordinary box-counting can be recovered by considering the line $\log(\lambda_1) = \log(\lambda_2)$ on the contour plot of generalized counts.

The generalized coverage counts allow a simple test for isotropy. An isotropic geometry would have coverage counts that are invariant to interchange of the λ_1-axis with the λ_2-axis. Thus, isotropy would be evidenced by reflective symmetry about the line $\log(\lambda_1) = \log(\lambda_2)$ in the generalized coverage count, $N(\lambda_1, \lambda_2)$. Conversely, anisotropy of a geometric figure (*e.g.*, jet-fluid-concentration level set for the transverse jet) is detectable by a lack of reflective symmetry about $\log(\lambda_1) = \log(\lambda_2)$.

We introduce a measure of the anisotropy of a contour embedded in two dimensions by considering the locus of points where the gradient of the coverage, $\nabla N(\lambda_1, \lambda_2)$, is aligned with the line $\log(\lambda_1) = \log(\lambda_2)$, *i.e.*,

$$\nabla N(\lambda_1, \lambda_2) \;\parallel\; (\widehat{\mathbf{e}}_1 + \widehat{\mathbf{e}}_2), \tag{6.2}$$

where $\widehat{\mathbf{e}}_1$ and $\widehat{\mathbf{e}}_2$ are unit vectors corresponding to the $\log(\lambda_1)$-axis and the $\log(\lambda_2)$-axis. We can define the (negative) partial logarithmic derivatives of the coverage (*cf.* Eq. 6.1) to be $D_{C,i}$,

$$D_{C,i} \equiv -\frac{\partial \log N(\lambda_1, \lambda_2)}{\partial \log \lambda_i} \tag{6.3}$$

The alignment of the gradient of coverage, as defined in Eq. 6.2 is equivalent to requiring $D_{C,1} = D_{C,2}$. At points given by Eq. 6.2, the generalized coverage is normalizable to yield (at least local) isotropy through rescaling of the axes by the ratio $\beta(\lambda)$,

$$\beta(\lambda) \;=\; \left.\frac{\lambda_1}{\lambda_2}\right|_{D_{C,1}=D_{C,2}}. \tag{6.4}$$

$\beta(\lambda)$, as defined by Eq. 6.4, is a scale-dependent measure of anisotropy for the set being covered, in the following sense: For every scale λ_1, there exists a multiplicative scaling, $\beta(\lambda)$, given by Eq. 6.4, of the $\log(\lambda_2)$-axis that transforms the generalized coverage count, $N(\lambda_1, \lambda_2)$, into $N(\lambda_1, \lambda_2' = \beta\lambda_2)$. The transformed coverage count, $N(\lambda_1, \lambda_2' = \beta\lambda_2)$, has local reflective symmetry about the line $\log(\lambda_1) = \log(\lambda_2')$ in the $[\log(\lambda_1), \log(\lambda_2')]$-plane. Thus, the geometric set can be renormalized in a scale-dependent manner to be isotropic. This isotropy is, in general, local about the line $\log(\lambda_1) = \log(\lambda_2')$, but in special cases can be complete for the entire $[\log(\lambda_1), \log(\lambda_2')]$-plane. We note that the points of equal partial derivatives given by Eq. 6.4 are not necessarily unique for a given length scale.

For instance, consider the simple affine transformation in two dimensions,

$$\mathbf{S}(A) \;=\; \mathbf{T}(A) + \mathbf{b},$$

where

$$\mathbf{T} \;=\; \begin{bmatrix} s_1 & 0 \\ 0 & s_2 \end{bmatrix}, \tag{6.5}$$

and $\mathbf{b} = 0$. For $s_1 \neq s_2$, this is an anisotropic contraction or expansion in different directions. If Eq. 6.5 is applied to a self-similar fractal set, *e.g.*, a Koch snowflake or an isotropic Sierpinski gasket, the resulting figure is self-affine rather than self-similar. Through the generalized coverage formalism described in Eq. 6.2 and Eq. 6.4, the imposed anisotropy $\beta = s_1/s_2$ may be recovered. For this simple

case, the anisotropy is the same at all scales (*i.e.*, β is a constant), and a simple rescaling of the set by:

$$\mathbf{R} = \begin{bmatrix} 1 & 0 \\ 0 & \beta \end{bmatrix} \propto \mathbf{T}^{-1} \tag{6.6}$$

would return the set to isotropy. In general, for scale-dependent anisotropy, β is a (not-necessarily-single-valued) function of scale, *i.e.*, $\beta = \beta(\lambda)$, and a different renormalization for each scale transforms the anisotropic set to local isotropy. In this sense, $\beta(\lambda)$ is a scale-dependent measure of the anisotropy of the set being covered.

6.3 Example: Rectangular perimeter

Consider the outline shown in Fig. 6.1, a rectangular perimeter with sides of width a and height b in the aspect ratio $\pi : 1$. This simple figure serves as a useful example of generalized coverage counting by allowing analytic calculation of $N(\lambda_z, \lambda_y)$ and its partial derivatives. For a smooth curve, such as the rectangle, the figure can be drawn with a single stroke, and the location of a point on the curve can be specified with a single number. The topological dimension and the "fractal" dimension are equivalent and have the value 1, the number of degrees of freedom of the curve. The number of rectangular tiles of size $\lambda_z \times \lambda_y$ necessary to cover the line is seen to be:

$$N(\lambda_z, \lambda_y) \simeq 2\,(\frac{a}{\lambda_z} + \frac{b}{\lambda_y})\,. \tag{6.7}$$

The logarithmic partial derivatives of the generalized coverage count are

$$\frac{\partial \log N(\lambda_z, \lambda_y)}{\partial \log \lambda_z} = \frac{-a\lambda_y}{a\lambda_y + b\lambda_z} \tag{6.8a}$$

and

$$\frac{\partial \log N(\lambda_z, \lambda_y)}{\partial \log \lambda_y} = \frac{-b\lambda_z}{a\lambda_y + b\lambda_z}. \tag{6.8b}$$

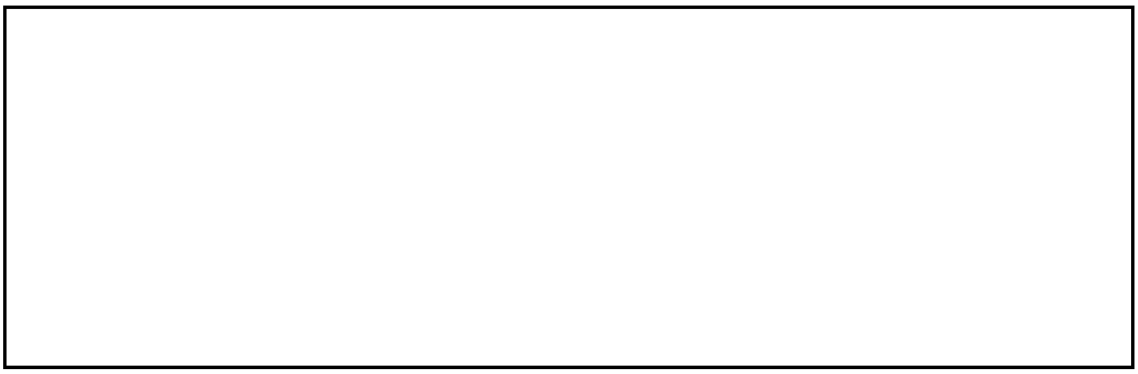

FIG. 6.1 Simple plane curve (rectangle) of width a and height b with aspect ratio $a : b = \pi$. Horizontal axis is z, vertical axis is y.

Equation 6.7 for the generalized coverage count is approximate because it allows for non-integer numbers of covering rectangles. The expression for $N(\lambda_z, \lambda_y)$, which is plotted in Fig. 6.2, is a poor approximation for large coverage tiles but becomes more accurate as the tile size tends to zero. The locus of points for which the gradient of $\log N(\lambda_z, \lambda_y)$ is directed along the line $\log \lambda_z = \log \lambda_y$ is found by equating the partial logarithmic derivatives in each direction,

$$D_{C,1} = D_{C,2} \;\Rightarrow\; \frac{a}{\lambda_z} = \frac{b}{\lambda_y}\,.$$

These points, for which $\nabla N(\lambda_z, \lambda_y) \parallel (\widehat{\log z} + \widehat{\log y})$, form a line given by $\log \lambda_z = \log \lambda_y + \beta$, where $\beta = \lambda_z/\lambda_y = a/b$ (Fig. 6.3). The ratio of horizontal to vertical scales, β, is the aspect ratio of the rectangular perimeter shown in Fig. 6.1. In this simple case, the anisotropy is identical for all length scales, so β has a constant value of π for all λ. A simple scaling of the vertical, y-axis by $\beta = \pi$, as in Eq. 6.6, would transform the rectangle into a square and return the set to isotropy.

The actual generalized coverage count of the rectangular curve shown in Fig. 6.1 is displayed in Fig. 6.4. The contour plot of coverage is shown in equal logarithmic increments of 0.2. A maximum of approximately 10^3 pixel-sized tiles are necessary to cover the rectangular perimeter. In "real" coverage counting (as opposed to the analytic expression plotted in Eq. 6.7), an integer number of tiles is guaranteed. Thus, for large coverage tiles (along the top and right-most edges of the contour plot), the coverage statistics do not match with Fig. 6.2. The difference

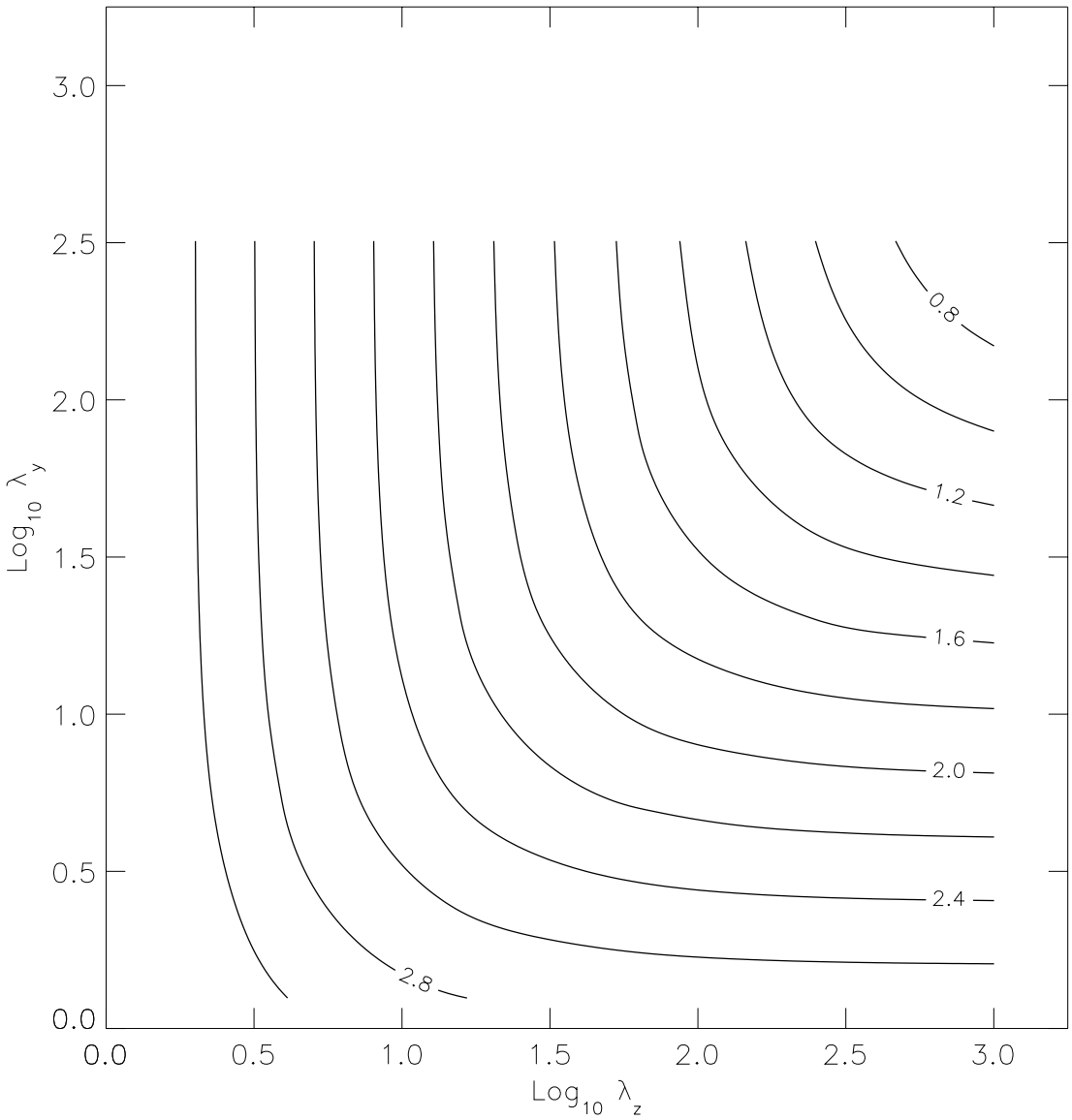

FIG. 6.2 Contour plot of analytic expression for $N(\lambda_z, \lambda_y)$ given in Eq. 6.7. The coverage is plotted in equal (base-10) logarithmic intervals. Anisotropy of set being covered is seen in the lack of reflective symmetry about the 45^o line bisecting the axes.

between Fig. 6.4 and Fig. 6.2 decreases as the coverage tiles shrink and the number, $N(\lambda_z, \lambda_y)$, of coverage tiles increases. Figure 6.5 shows the locus of points of $D_{C,1} = D_{C,2}$. The anisotropy of the rectangular perimeter can be computed from the ratio of horizontal to vertical scales at the points of equal partial logarithmic derivatives (Eq. 6.4). For the simple rectangle of aspect ratio $\pi : 1$, the anisotropy

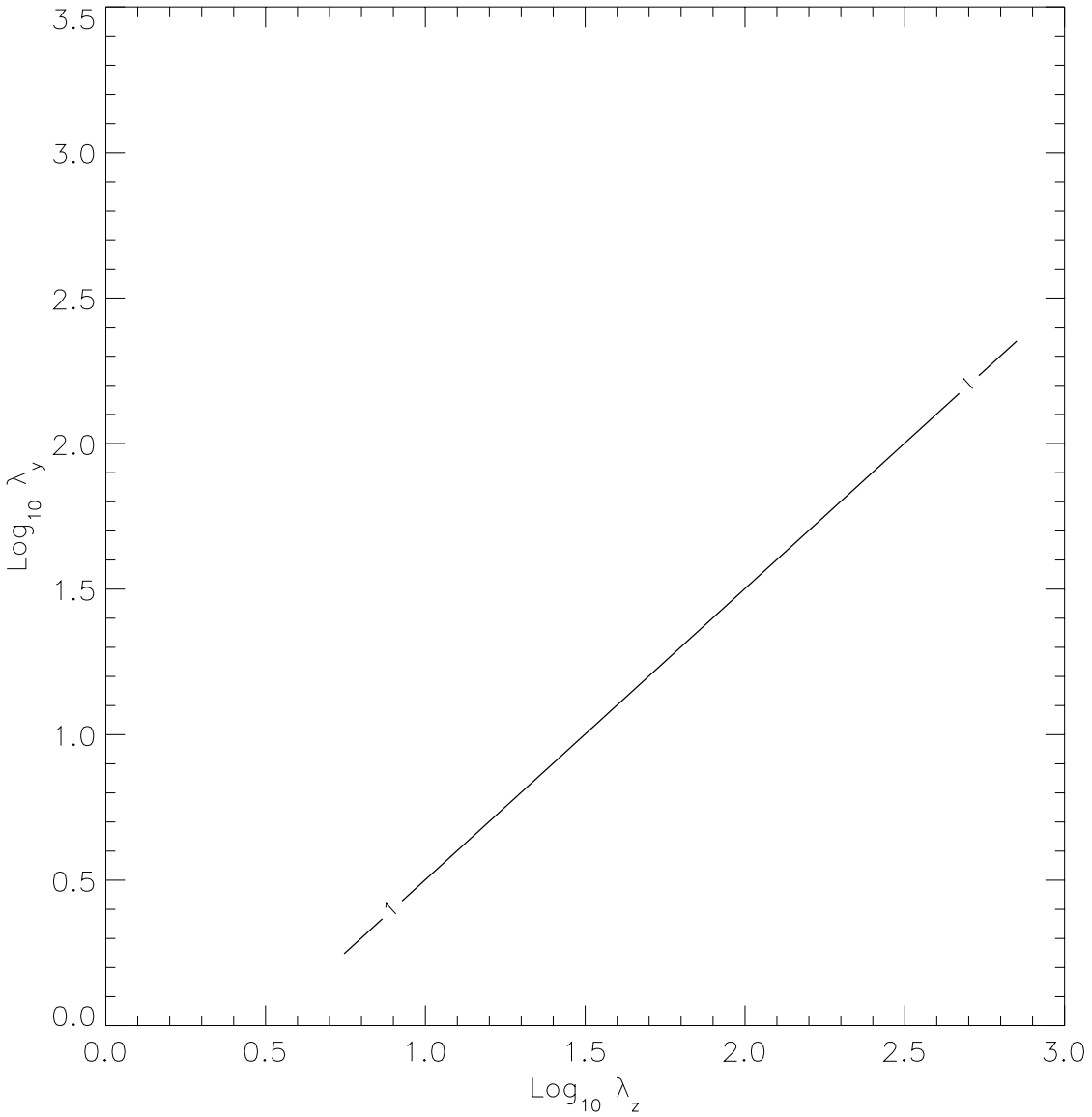

FIG. 6.3 Locus of points where partial logarithmic derivatives of analytical expression for $N(\lambda_z, \lambda_y)$ are equal, *i.e.*, where $\nabla N(\lambda_z, \lambda_y) \parallel (\widehat{\log z} + \widehat{\log y})$ in Fig. 6.2. These points are plotted as the line where $D_{C,1}/D_{C,2} = 1$.

is expected to be independent of scale, and to have the exact value $\beta = \pi$. This is confirmed by Fig. 6.6, which shows the anisotropy ratio computed from the coverage count shown in Fig. 6.4. The experimental value of $\beta = \lambda_z/\lambda_y \simeq 10^{0.497} = 3.14$ matches the imposed anisotropy of the rectangular perimeter being covered.

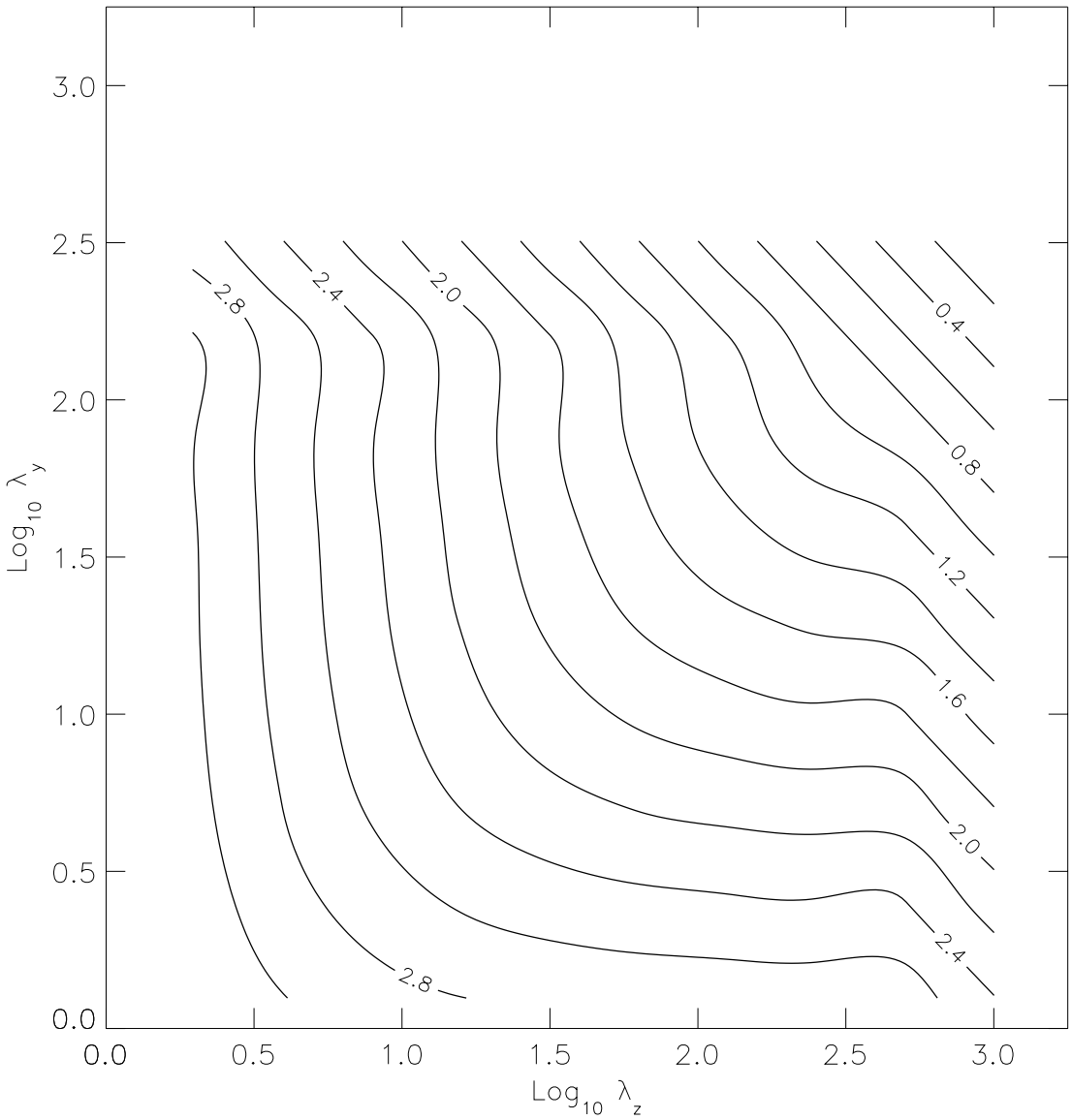

FIG. 6.4 Actual coverage $N(\lambda_z, \lambda_y)$ of Fig. 6.1, plotted in equal base-10 logarithmic contours. Anisotropy of rectangular perimeter being covered is seen in the lack of reflective symmetry about the 45^o line bisecting the axes.

6.4 Example: Sierpinski carpet

The Sierpinski carpet is a classical fractal which is a higher-dimensional generalization of the one-dimensional Cantor set (Peitgen *et al.* 1993). A vertical or horizontal transect of the Sierpinski carpet, taken through the center of the figure, is precisely the Cantor set. Beginning with a square, the Sierpinski carpet is iter-

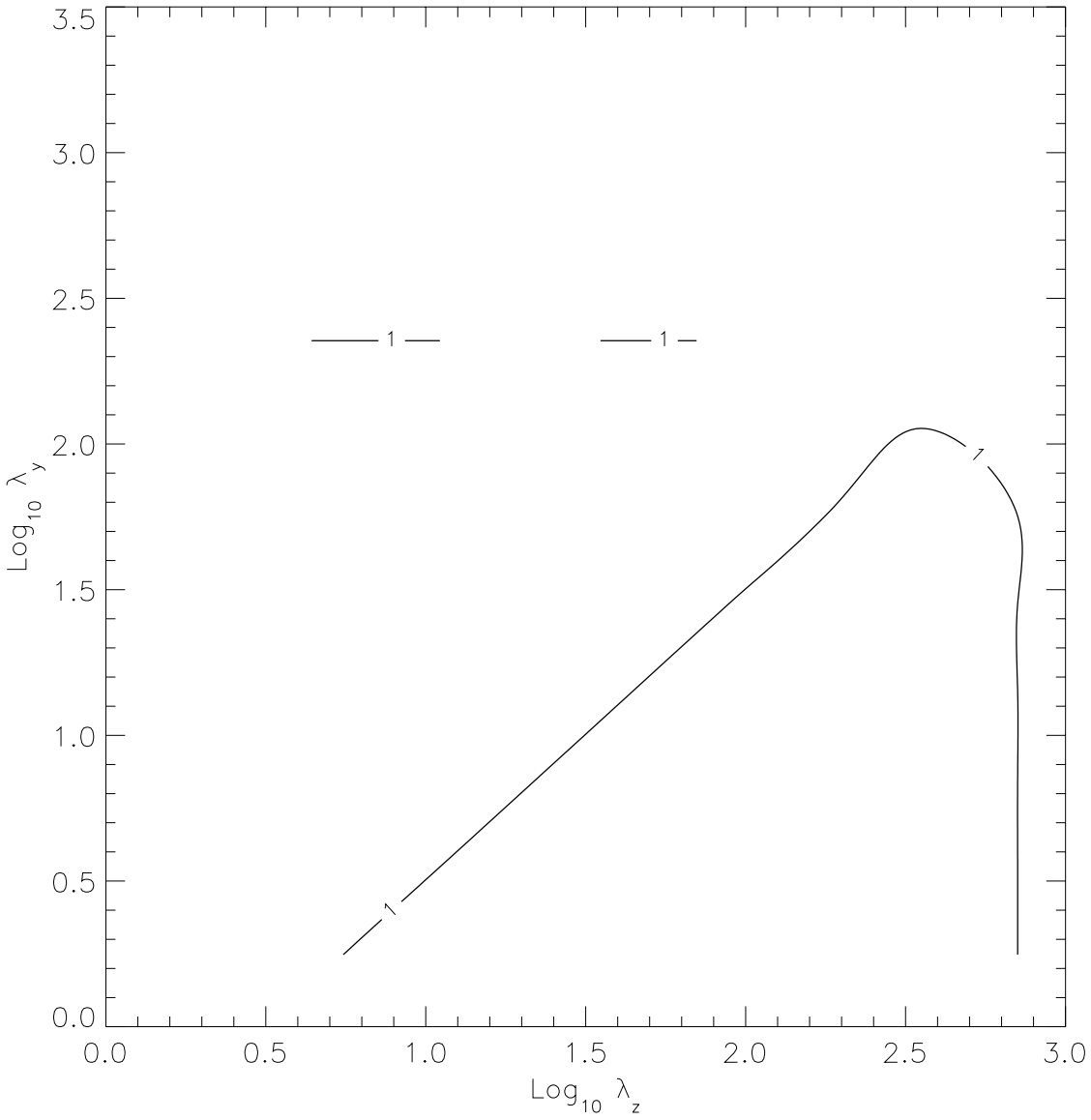

FIG. 6.5 Locus of points where $\nabla N(\lambda_z, \lambda_y) \parallel (\widehat{\log z} + \widehat{\log y})$ for the actual coverage count depicted in Fig. 6.4. The $\log \lambda_z$ intercept of the $D_{C,1} = D_{C,2}$ line gives the measured anisotropy of the rectangular perimeter, $\beta = \lambda_z/\lambda_y \simeq 10^{0.497} = 3.14$.

atively constructed by subdividing the initial square into nine, smaller, congruent squares, and deleting the middle square. The limiting set of this process is the Sierpinski carpet. An anisotropic variant of the Sierpinski carpet can be constructed in an analogous fashion by starting with a rectangle and removing the central "1/3" of the rectangle. The anisotropic initial conditions lead to a self-affine set, rather

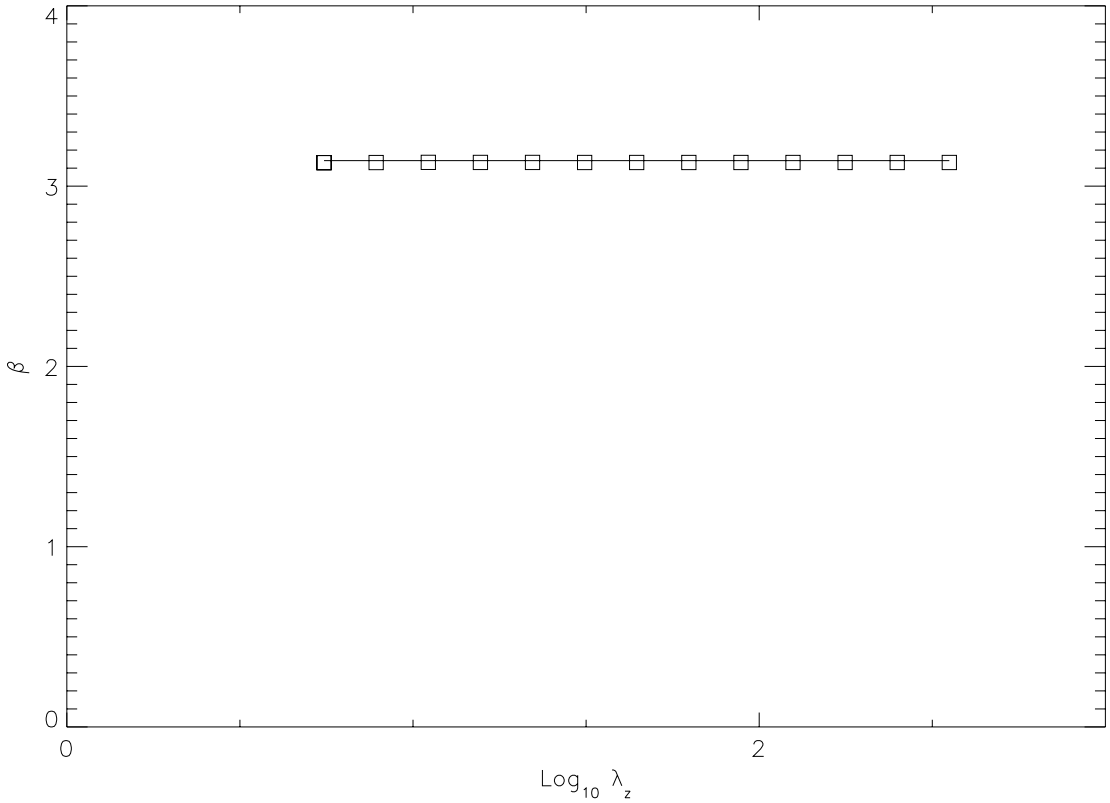

FIG. 6.6 Measured anisotropy of rectangular perimeter. The scale-dependent measure of anisotropy, $\beta(\lambda)$, is calculated using Eq. 6.4 from the coverage plot shown in Fig. 6.4. Comparison line of $\beta = \pi$ shows expected anisotropy, the original aspect ratio of the rectangle.

than an isotropic figure. The first few iterations of a self-affine Sierpinski carpet, constructed from an initial rectangle of aspect ratio 3 : 1, are shown in Figs. 6.7 and 6.8.

Although an analytic expression for the generalized coverage count is not available for the Sierpinski carpet, the count can still be computed. The coverage count for the self-affine Sierpinski carpet is displayed in Fig. 6.9 as a function of tile size, $\lambda_z \times \lambda_y$. The maximum level shown in the logarithmic contour plot is 5.6, hence approximately 4.0×10^5 pixel-size tiles are necessary to cover the Sierpinski carpet. The loci of points where partial logarithmic derivatives of $N(\lambda_z, \lambda_y)$ are equal is shown in Fig. 6.10 as lines of $D_{C,1}/D_{C,2} = 1$. Along the line of $D_{C,1} = D_{C,2}$ in Fig. 6.10, we find $\log \lambda_z \simeq \log \lambda_y + 0.477$. As measured by the generalized cov-

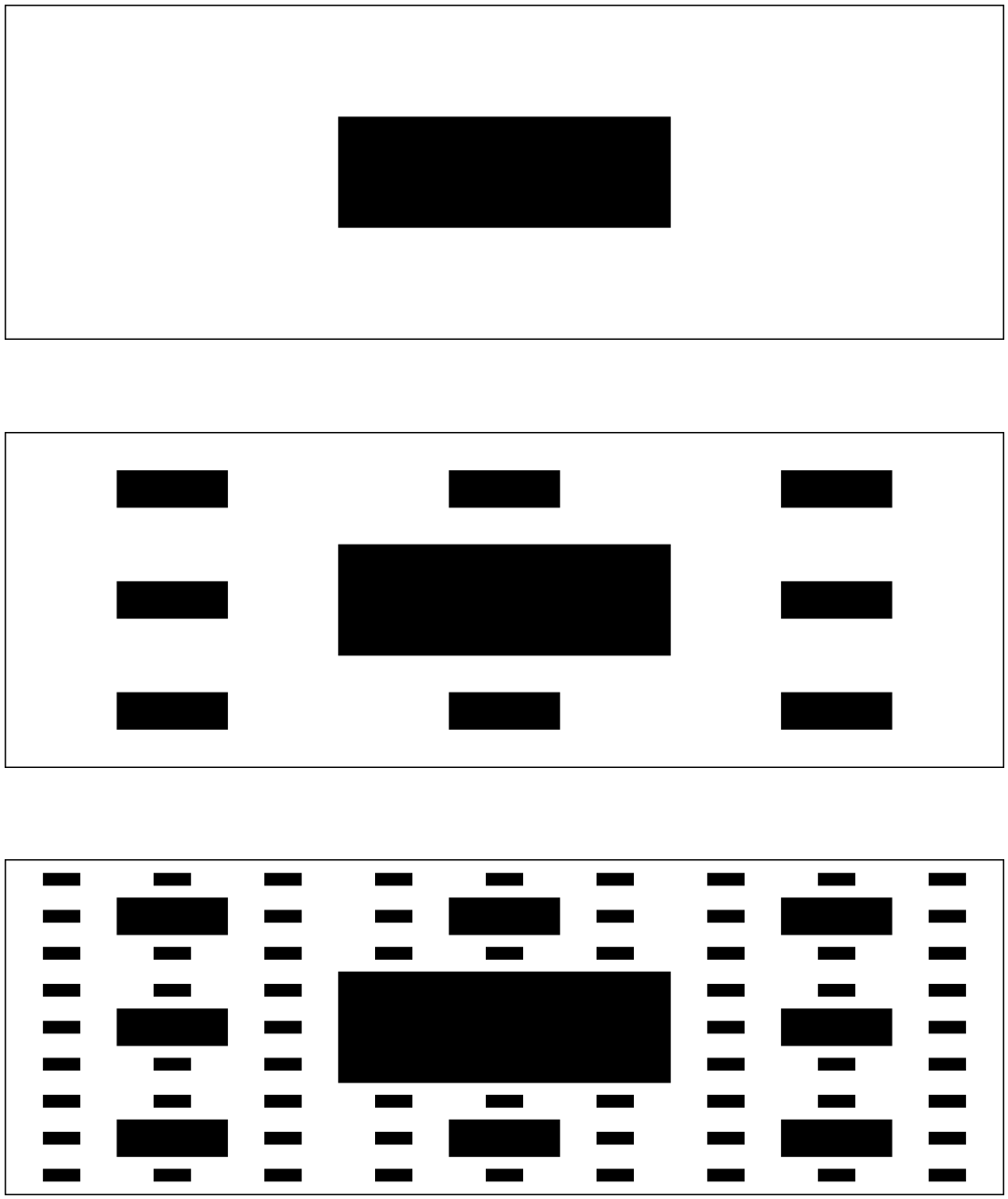

FIG. 6.7 First three iterations of the construction of a self-affine Sierpinski carpet embedded in two dimensions from a rectangle of aspect ratio 3 : 1. The central "1/3" is removed from each rectangle.

erage statistics, the anisotropy of the set is constant for all scales, and has value

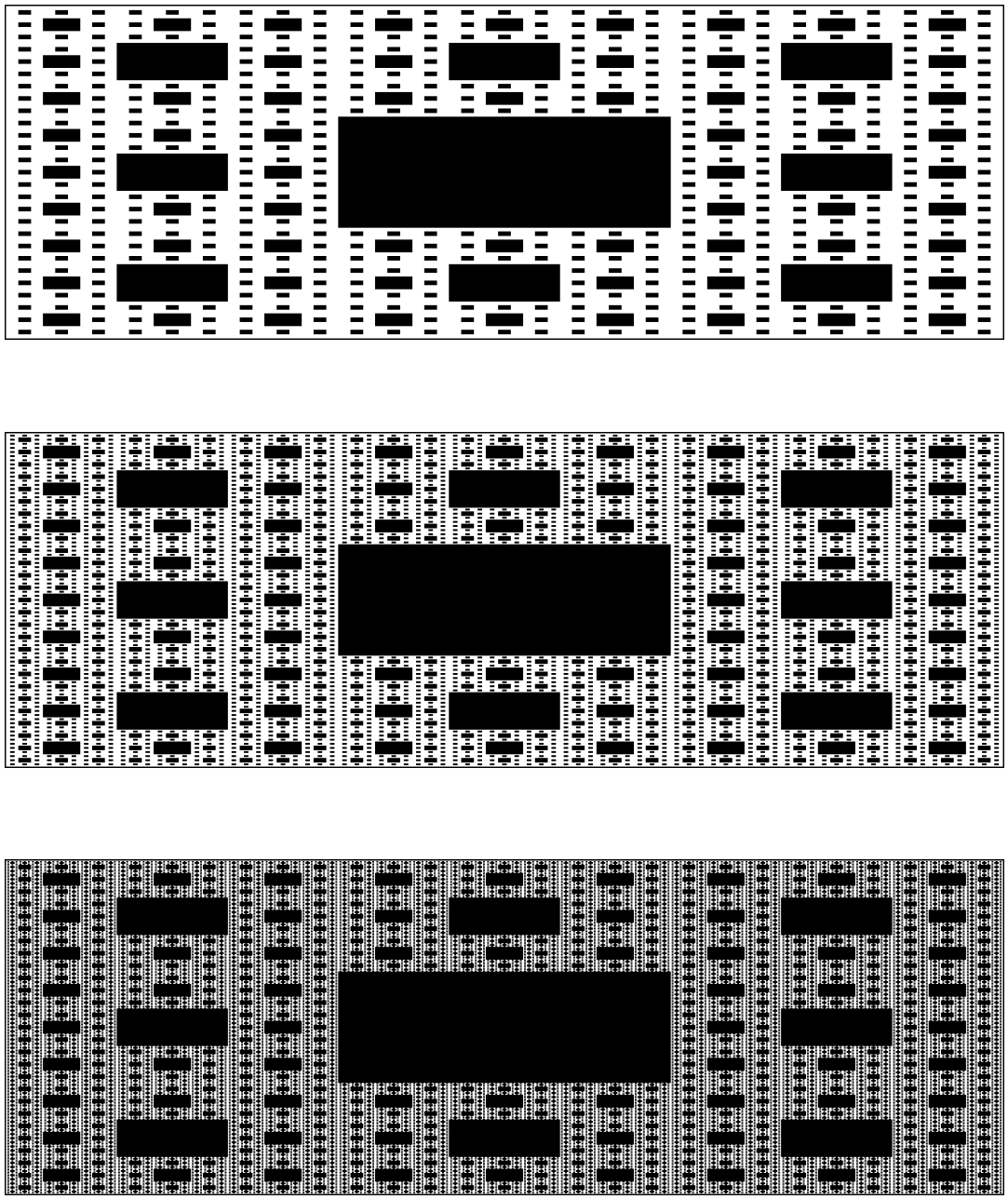

FIG. 6.8 Next three iterations.

$\beta = 10^{0.477} = 3.0$ (Fig. 6.11). This matches the 3 : 1 aspect ratio of the initial conditions used to construct the self-affine fractal. A linear transformation, **R**, of

the form

$$\mathbf{R} = \begin{bmatrix} 1 & 0 \\ 0 & \beta \end{bmatrix}$$

would rescale the anisotropic Sierpinski carpet to a self-similar fractal.

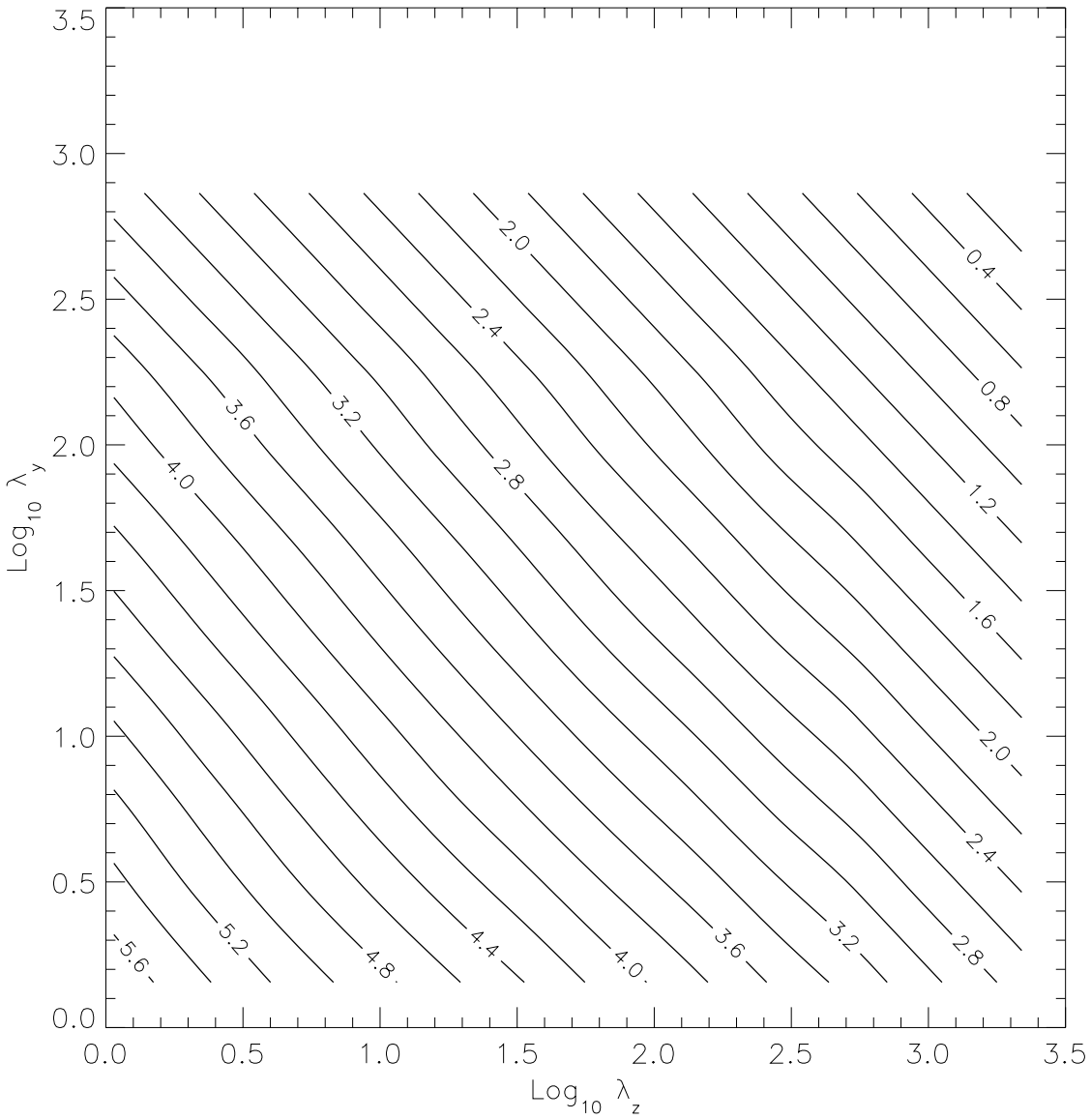

FIG. 6.9 Coverage $N(\lambda_z, \lambda_y)$ of self-affine Sierpinski carpet, shown in base-10 logarithmic contours. The final iteration of the construction shown in Fig. 6.8 is used. The set is anisotropic, and the coverage is not reflectively symmetric about the 45^o line bisecting the axes. This can be seen in the partial logarithmic derivatives of $N(\lambda_z, \lambda_y)$.

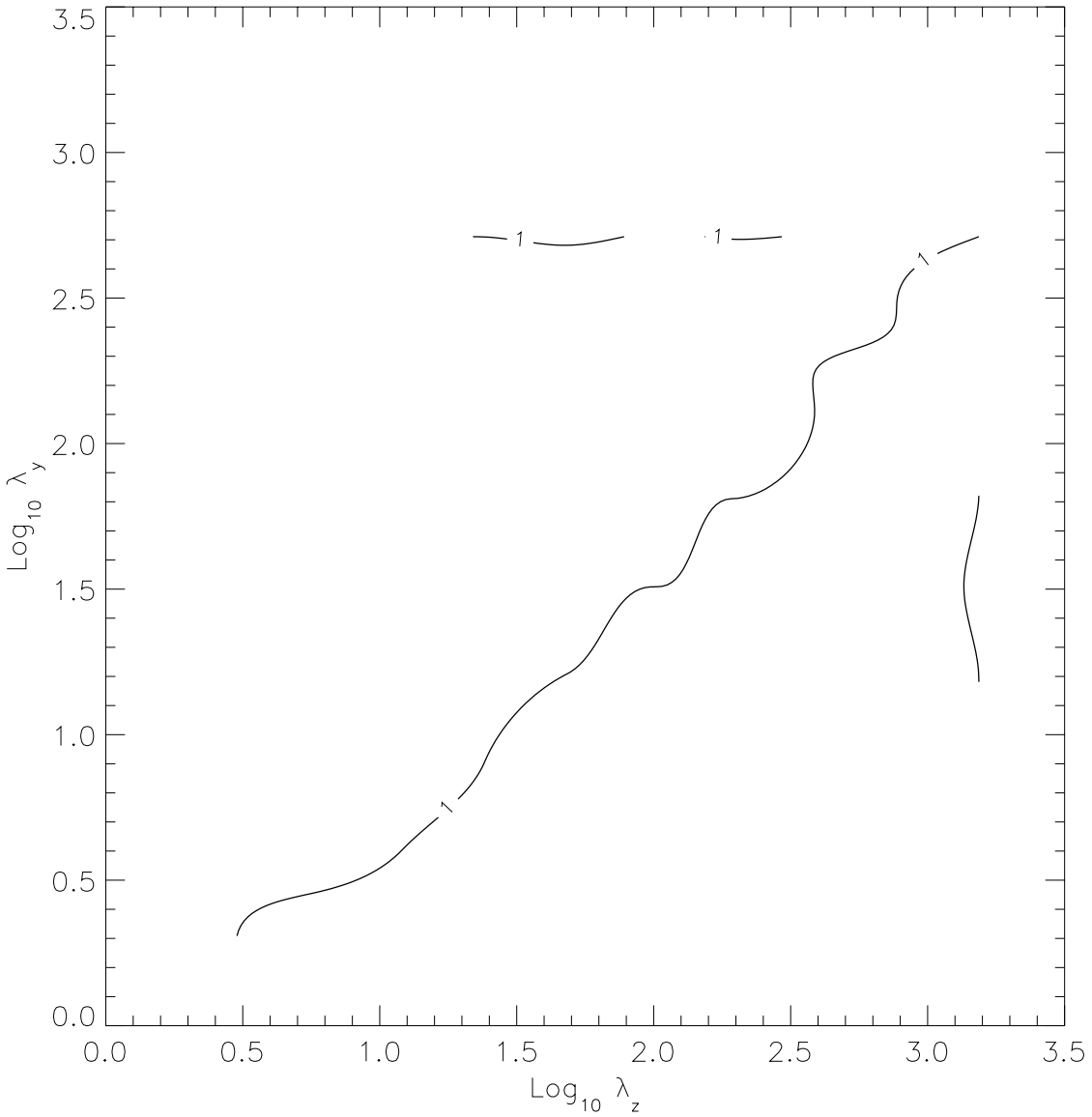

FIG. 6.10 Locus of points where $\nabla N(\lambda_z, \lambda_y) \parallel (\widehat{\log z} + \widehat{\log y})$ for the self-affine Sierpinski carpet. The $\log \lambda_z$ intercept of the $D_{C,1} = D_{C,2}$ line gives the measured anisotropy of the set, $\beta = \lambda_z/\lambda_y \simeq 10^{0.477} = 3.00$.

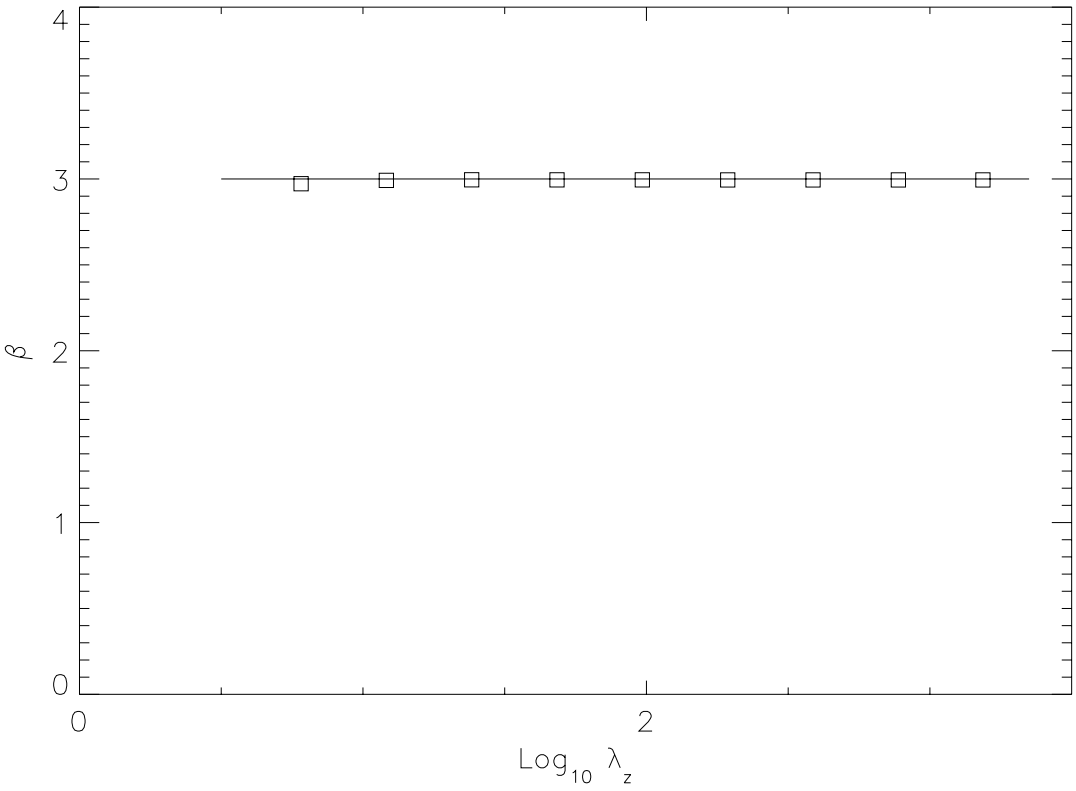

FIG. 6.11 Measured anisotropy of Sierpinski carpet. The scale-dependent measure of anisotropy, $\beta(\lambda)$, is calculated using Eq. 6.4 from the coverage plot shown in Fig. 6.9. Comparison line of $\beta = 3$ shows the expected anisotropy, the original aspect ratio of the Sierpinski carpet imposed by the initial conditions.

CHAPTER 7

Geometric complexity of transverse-jet isosurfaces

The geometric complexity of level sets of jet-fluid concentration in transverse jets is investigated for varying concentration thresholds. Two different Reynolds numbers, $Re_{\mathrm{j}} = 1.0 \times 10^3$ and 20×10^3, are investigated. Ensemble-averaged coverage counts, $N(\lambda_1, \lambda_2)$, are computed at each Reynolds number from coverage counts of six images of the jet-fluid concentration field. The anisotropy of the scalar isosurface is assessed in terms of the scale-dependent measure, $\beta(\lambda)$. The special case of ordinary (isotropic) box-counting is considered, and ensemble-averaged coverage counts, $N_2(\lambda)$, coverage lengths, $L_2(\lambda)$, coverage fraction, $F_2(\lambda)$, and coverage dimension, $D_2(\lambda)$, are calculated for the $Re_{\mathrm{j}} = 20 \times 10^3$ jet. Comparisons are made between the transverse jet, and the turbulent jet discharging into a quiescent reservoir.

7.1 Isoscalar bounding-box size

The geometric complexity of isoscalar surfaces in the transverse jet is described within the formalism of generalized coverage counts introduced in the previous chapter. Iso-concentration contours embedded in two-dimensional image data are covered with tiles of varying size and shape. This anisotropic coverage-counting begins by finding the bounding rectangle, of size $\delta_{\mathrm{b},z} \times \delta_{\mathrm{b},y}$, that encloses the isosurface defined by a chosen concentration level, C_{iso}. The bounding rectangle is successively subdivided, and coverage counts are computed as the number of partition tiles containing the level-set contour of jet-fluid concentration. The partition of the bounding rectangle takes place in two directions, so the coverage is found as a function of coverage-tile size, $\lambda_z \times \lambda_y$. In the first iteration of the coverage process, the bounding rectangle, $\delta_{\mathrm{b},z} \times \delta_{\mathrm{b},y}$, is subdivided into two rectangular coverage tiles, so $\lambda_z^{(1,0)} = \delta_{\mathrm{b},z}/2$ and $\lambda_y^{(1,0)} = \lambda_{\mathrm{b},y}$. The subdivision continues in both directions, so that upon the $(i,k)^{\mathrm{th}}$ iteration, the coverage tile has size $\lambda_z^{(i,k)} \times \lambda_y^{(i,k)}$, where:

$$\lambda_z^{(i,k)} = \frac{\delta_{\mathrm{b},z}}{2^i} \tag{7.1a}$$

$$\lambda_y^{(i,k)} = \frac{\delta_{\mathrm{b},y}}{2^k}\,. \tag{7.1b}$$

Bilinear interpolation is used to represent the isosurfaces for noninteger-sized coverage tiles. This anisotropic coverage-counting method produces counts over the entire range of scales, from (nearly) the image-pixel resolution to the outer spatial extent of the jet-fluid-concentration isosurface. The generalized coverage counts, $N(\lambda_z, \lambda_y)$, are functions of horizontal and vertical scales, λ_z and λ_y, and are suitable for the anisotropic, non-self-similar sets that are expected for transverse jets.

7.2 Generalized coverage for transverse-jet isosurfaces: $Re_j = 1.0 \times 10^3$

The level-set geometry of turbulent mixing in transverse jets was investigated using data from transverse sections at Reynolds number $Re_j = 1.0 \times 10^3$ and velocity ratio $V_r = 10$ (*e.g.*, Fig. 2.7). Contour plots of the ensemble-averaged coverage counts, $N(\lambda_z, \lambda_y)$, of the level sets of jet-fluid concentration for $C_{iso} = 0.01$, 0.03, and 0.05 are shown in Figs. 7.1, 7.3, and 7.5, respectively. Coverage counts are individually computed at each concentration level from six images of the cross-section of the transverse jet. The images were recorded 50 nozzle-diameters downstream from the jet-exit. Frames 0, 100, 200, 300, 400, and 500 were used from the sequence of 508 images of scalar concentration in the jet. The six individual coverage counts are then averaged with Gaussian interpolation functions to generate the ensemble-averaged coverage plots of $N(\lambda_z, \lambda_y)$. Horizontal scales, λ_z, and vertical scales, λ_y, are normalized by the overall, threshold-dependent bounding-box size for the image, $\delta_b(C; Re_j)$. This overall bounding-box size, δ_b, is defined as the root-mean-square of the individual bounding-box sizes:

$$\delta_b(C; Re_j) \equiv \sqrt{\frac{1}{N} \sum_{n=1}^{N} \delta_{z,b} \delta_{y,b}}. \tag{7.2a}$$

The above definition of the bounding box is based upon the mean area of the individual bounding-boxes. An alternative definition based on the geometric mean of the bounding-box size is possible,

$$\delta_b(C; Re_j) = \frac{1}{N} \sum_{n=1}^{N} \sqrt{\delta_{z,b} \delta_{y,b}}. \tag{7.2b}$$

The difference between Eq. 7.2a and Eq. 7.2b is small (as it is in this case) if the distribution of bounding-box sizes is small over the N images. For the results described here, the overall bounding box size defined in Eq. 7.2a is used to normalize length scales. Coverage counts, plotted in base-10 logarithmic increments as a function of normalized coverage-tile size, range from 1, for the bounding box, to greater than 10^4 for the smallest, pixel-sized, coverage tile.

The scale-dependent anisotropy of the level sets (isolines of jet-fluid concentration) is assessed by computing the points for which the partial derivatives of

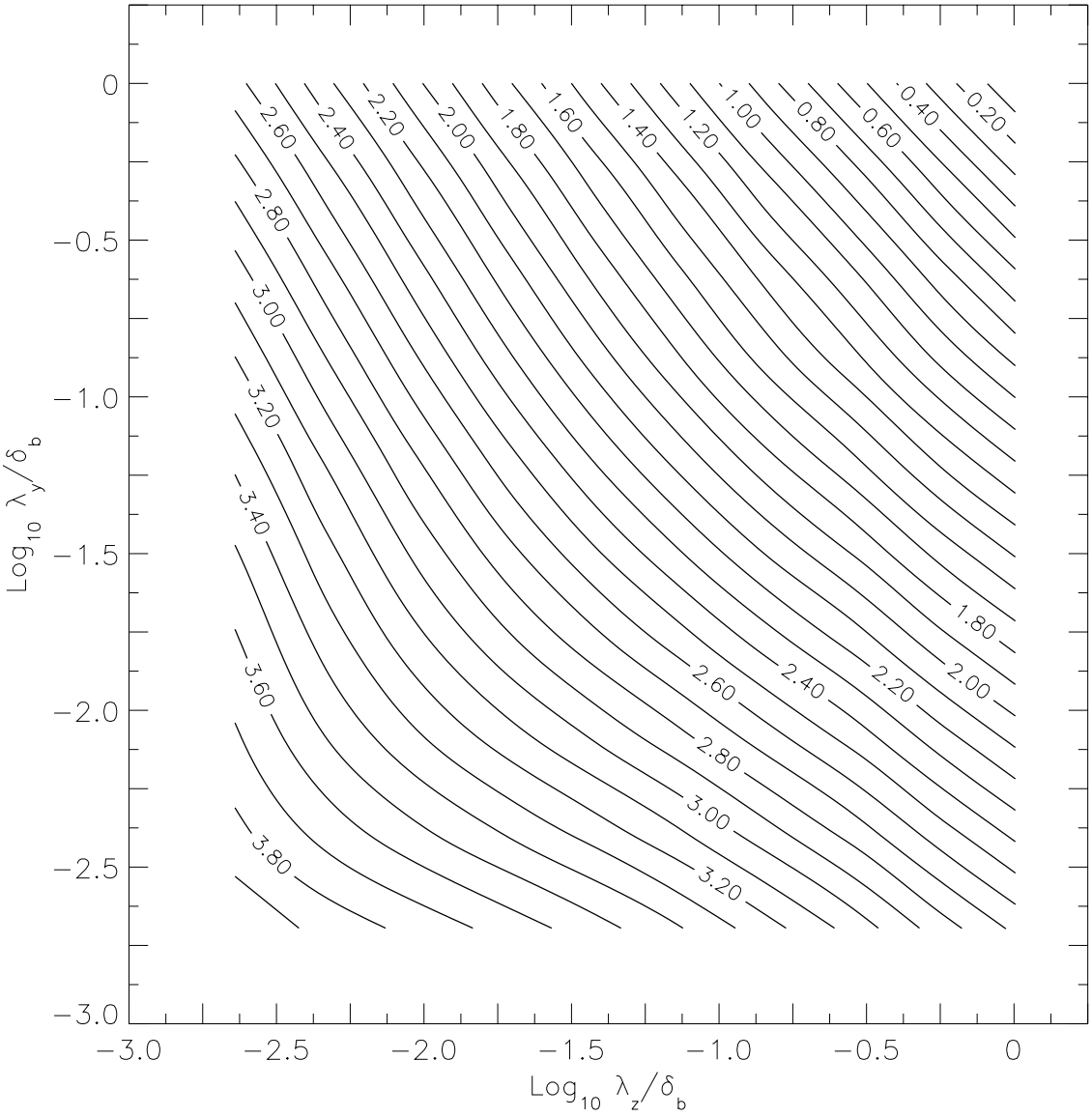

FIG. 7.1 Generalized coverage of level sets of jet-fluid concentration for $C_{\rm iso} = 0.01$ at $Re_{\rm j} = 1.0 \times 10^3$. Coverage count, $N(\lambda_z, \lambda_y)$, is plotted as (base-10) logarithmic contours. Length scales nondimensionalized by bounding-box size, $\delta_{\rm b}$, at this concentration level (Eq. 7.2a). Anisotropy of the level set is seen in the lack of reflective symmetry about the 45^o line bisecting the axes (see also Fig. 7.2).

the coverage $N(\lambda_z, \lambda_y)$ are equal. This is plotted in Fig. 7.2, Fig. 7.4, and Fig. 7.6 for the ensemble-averaged coverage counts for isosurfaces of $C_{\rm iso} = 0.01$, 0.03, and 0.05. The anisotropy measure, $\beta(\lambda)$, is shown in Fig. 7.7 for all three concentration

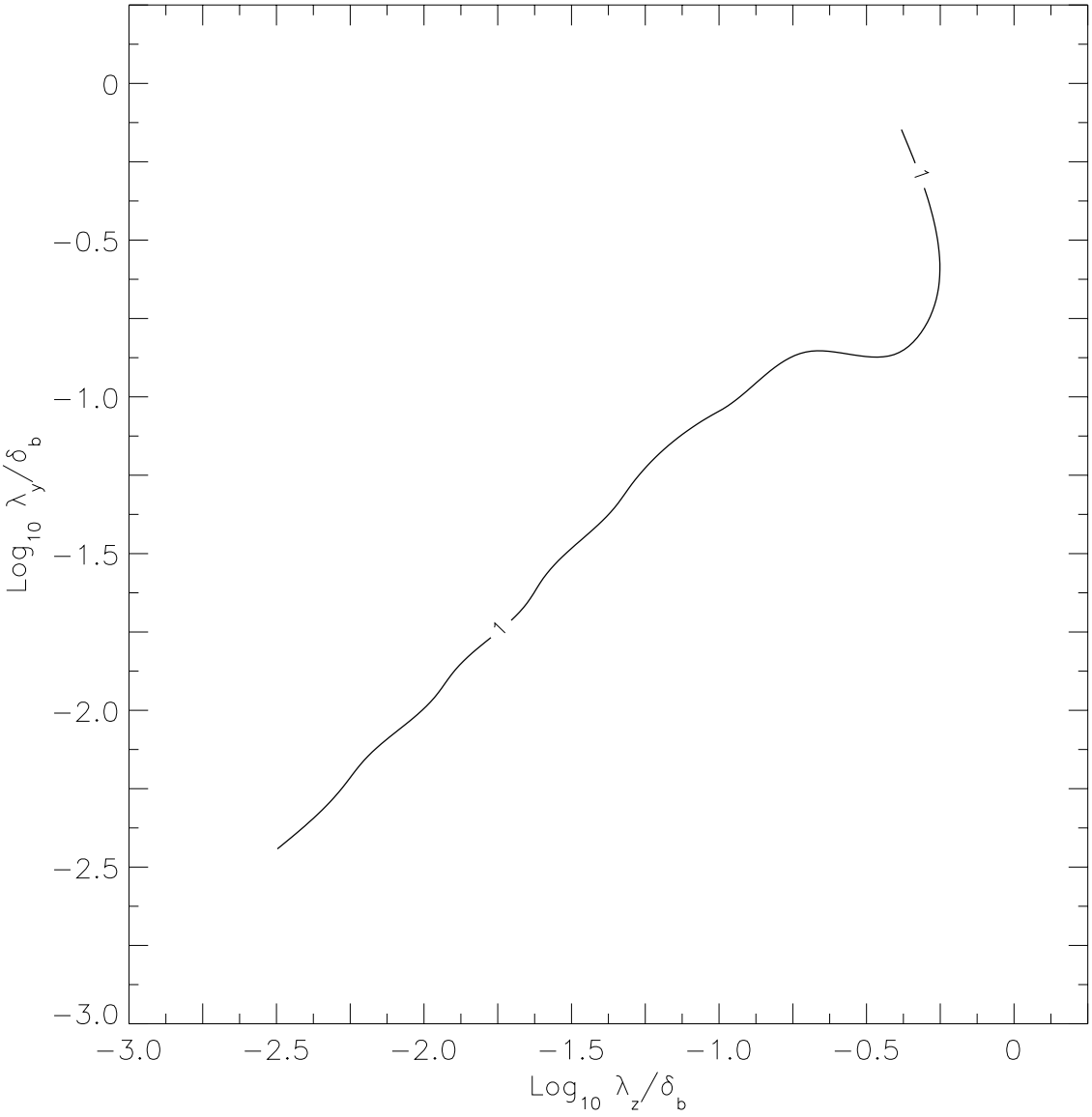

FIG. 7.2 $Re_{\rm j} = 1.0 \times 10^3$ and $C_{\rm iso} = 0.01$. Locus of points where partial logarithmic derivatives of coverage $N(\lambda_z, \lambda_y)$ are equal, *i.e.*, where $\nabla N(\lambda_z, \lambda_y) \parallel (\widehat{\log z} + \widehat{\log y})$. These points are plotted as the line where $D_{C,1}/D_{C,2} = 1$. Departure of this line from a 45^o bisector of the axes indicates anisotropy of isoscalar surface at this concentration, $C_{\rm iso}$.

levels. Values of $\beta(\lambda)$ greater than 1 indicate that a stretching of the vertical axes is required to transform the isosurface contour to local isotropy; conversely, $\beta(\lambda)$ less than 1 indicates a contraction of the vertical axes is necessary for isotropy. Thus, $\log \beta(\lambda) > 0$ suggests a statistical preference for horizontal structures in the

iso-concentration contour, and $\log \beta(\lambda) < 0$ a preference for vertical structures, at length scale λ. Figure 7.7 indicates that, for isosurfaces in cross-sections of the transverse jet at $Re_{\rm j} = 1.0 \times 10^3$, small scales are anisotropic and tend to be vertically oriented, while large scales are anisotropic but horizontally oriented. Slight variations are seen in $\beta(\lambda)$ with iso-concentration level, *e.g.*, there is a small increase in the measured anisotropy at small scales with increasing concentration level. However, the overall tendency for vertical structures at small scales, and horizontal structures at large scales, is consistent for all iso-concentration levels studied.

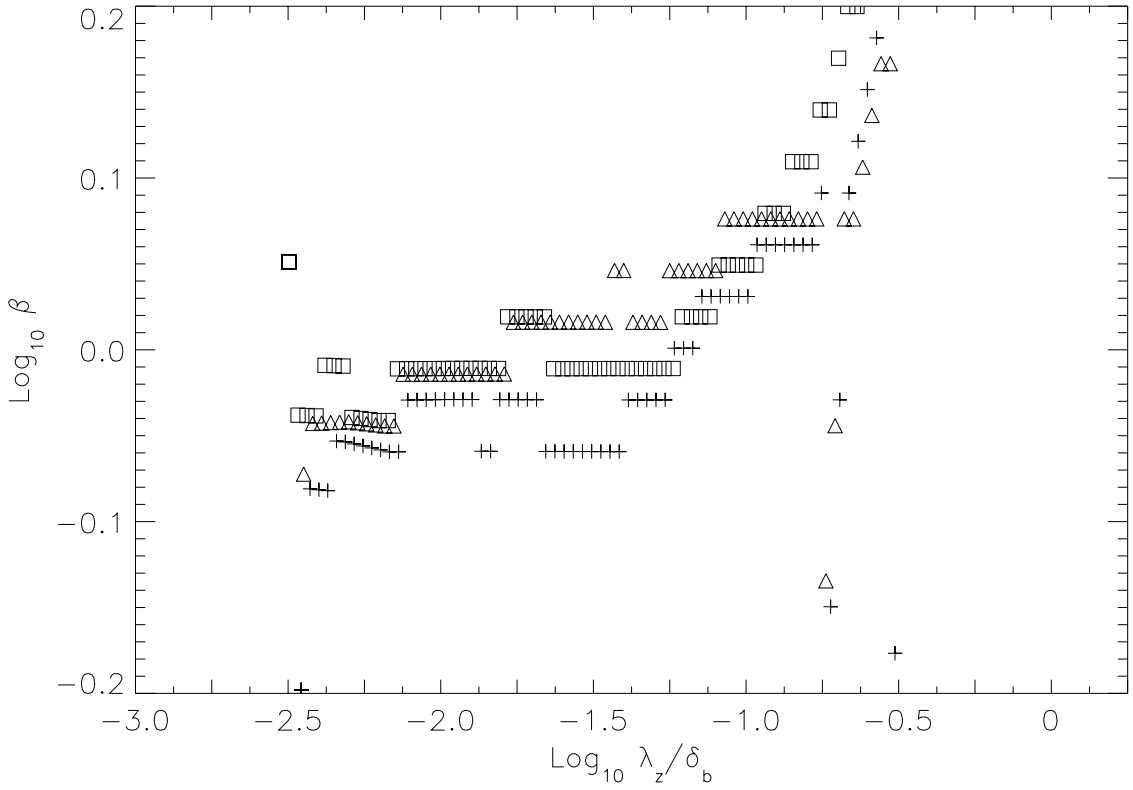

FIG. 7.7 Measured anisotropy of iso-concentration surface for $Re_{\rm j} = 1.0 \times 10^3$. Small scales of isosurface contour are preferentially stretched ($\beta(\lambda) < 1$) in the vertical direction, $\widehat{\mathbf{y}}$, while large scales are preferentially stretched ($\beta(\lambda) > 1$) in the horizontal direction, $\widehat{\mathbf{z}}$. Squares: $C_{\rm iso} = 0.01$. Triangles: $C_{\rm iso} = 0.03$. Crosses: $C_{\rm iso} = 0.05$.

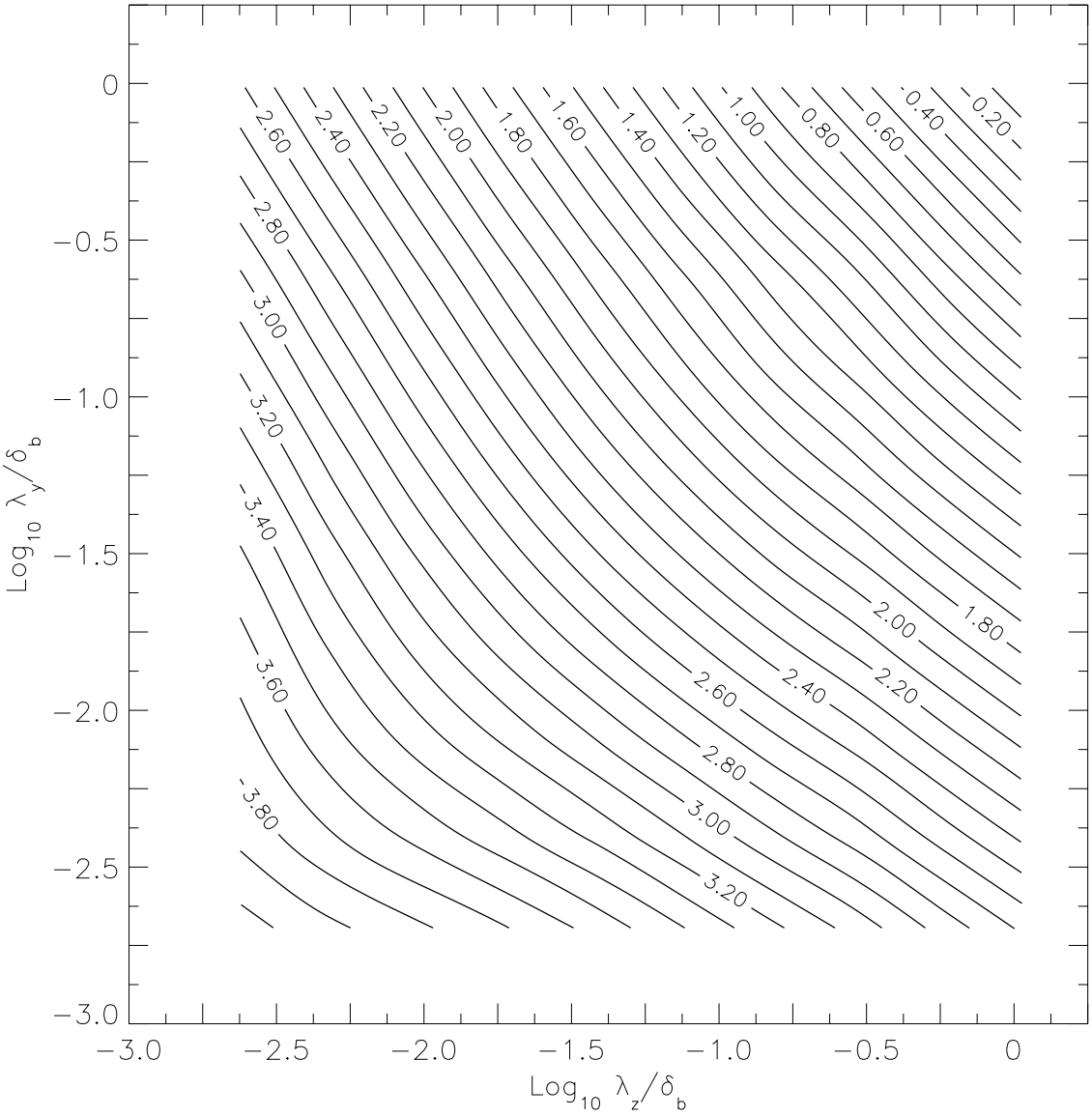

FIG. 7.3 Generalized coverage $N(\lambda_z, \lambda_y)$ of isoscalar surface for $C_{\rm iso} = 0.03$ at $Re_{\rm j} = 1.0 \times 10^3$.

7.3 Generalized coverage for transverse-jet isosurfaces: $Re_{\rm j} = 20 \times 10^3$

The level-set geometry of turbulent transverse jets was also investigated at Reynolds number $Re_{\rm j} = 20 \times 10^3$ and velocity ratio $V_{\rm r} = 10$. Figures 7.8, 7.10, and 7.12 show the coverage counts $N(\lambda_z, \lambda_y)$ for three isosurfaces of $C_{\rm iso} = 0.01$, $C_{\rm iso} = 0.03$, and $C_{\rm iso} = 0.05$. Six images are ensemble averaged to produce the coverage counts shown. Again, frames 000, 100, 200, 300, 400, and 500 are selected

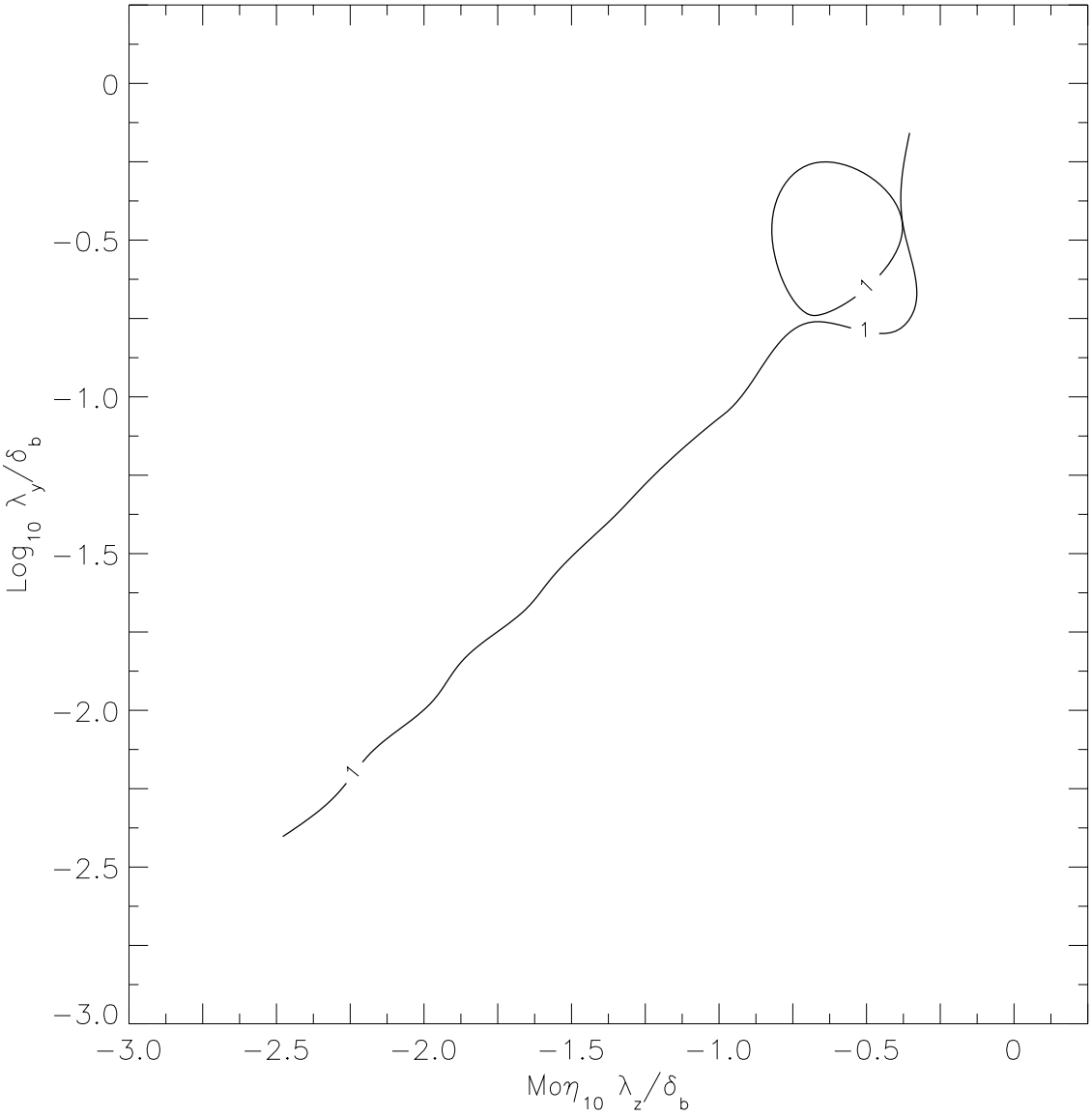

FIG. 7.4 $Re_{\rm j} = 1.0 \times 10^3$ and $C_{\rm iso} = 0.03$. Locus of points where partial derivatives of coverage $N(\lambda_z, \lambda_y)$ are equal. Departure of line from a 45^o line bisecting the axes indicates anisotropy of isoscalar surface at this concentration, $C_{\rm iso}$.

from the sequence of 508 images of the jet-fluid-concentration field. Anisotropy of the iso-concentration surface is measured by computing the points for which the partial logarithmic derivatives of the two-dimensional coverage are equal. These equal-partial-derivative points are plotted in Figs. 7.9, 7.11, and 7.13 for each concentration level. The scale-dependent anisotropy of the isosurface is measured by computing $\beta(\lambda)$ for all three concentrations, as seen in Fig. 7.14. The anisotropy

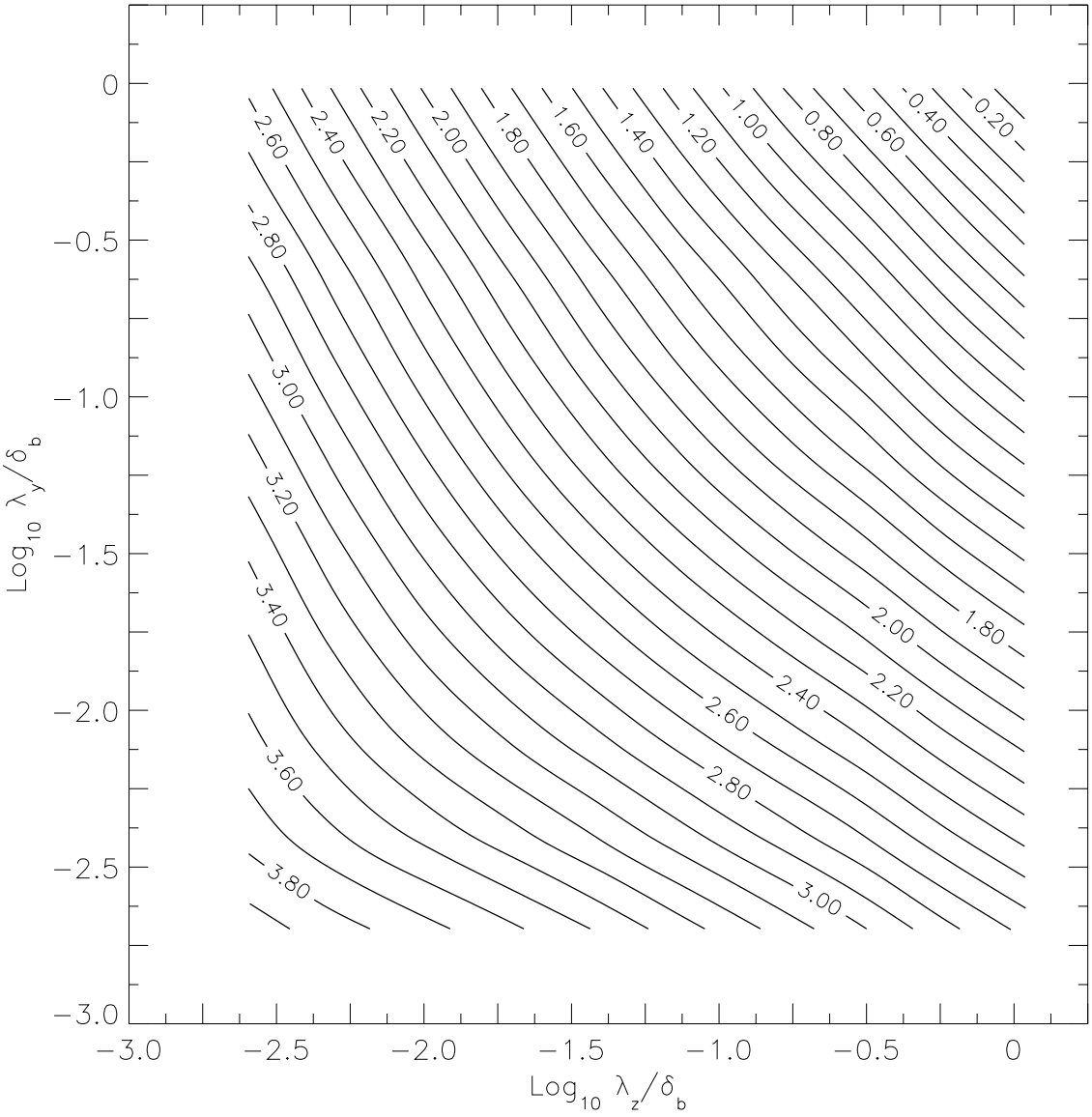

FIG. 7.5 Generalized coverage $N(\lambda_z, \lambda_y)$ of isoscalar surface for $C_{\rm iso} = 0.05$ at $Re_{\rm j} = 1.0 \times 10^3$.

measure, $\beta(\lambda)$, is found to be less than unity for small scales, indicating a preference for small, tall, narrow structures. At larger scales, the value of $\beta(\lambda)$ increases and becomes greater than unity, showing a preference for large, short, wide features in the isosurfaces. There is no clear variation of $\beta(\lambda)$ with concentration level at this high Reynolds number.

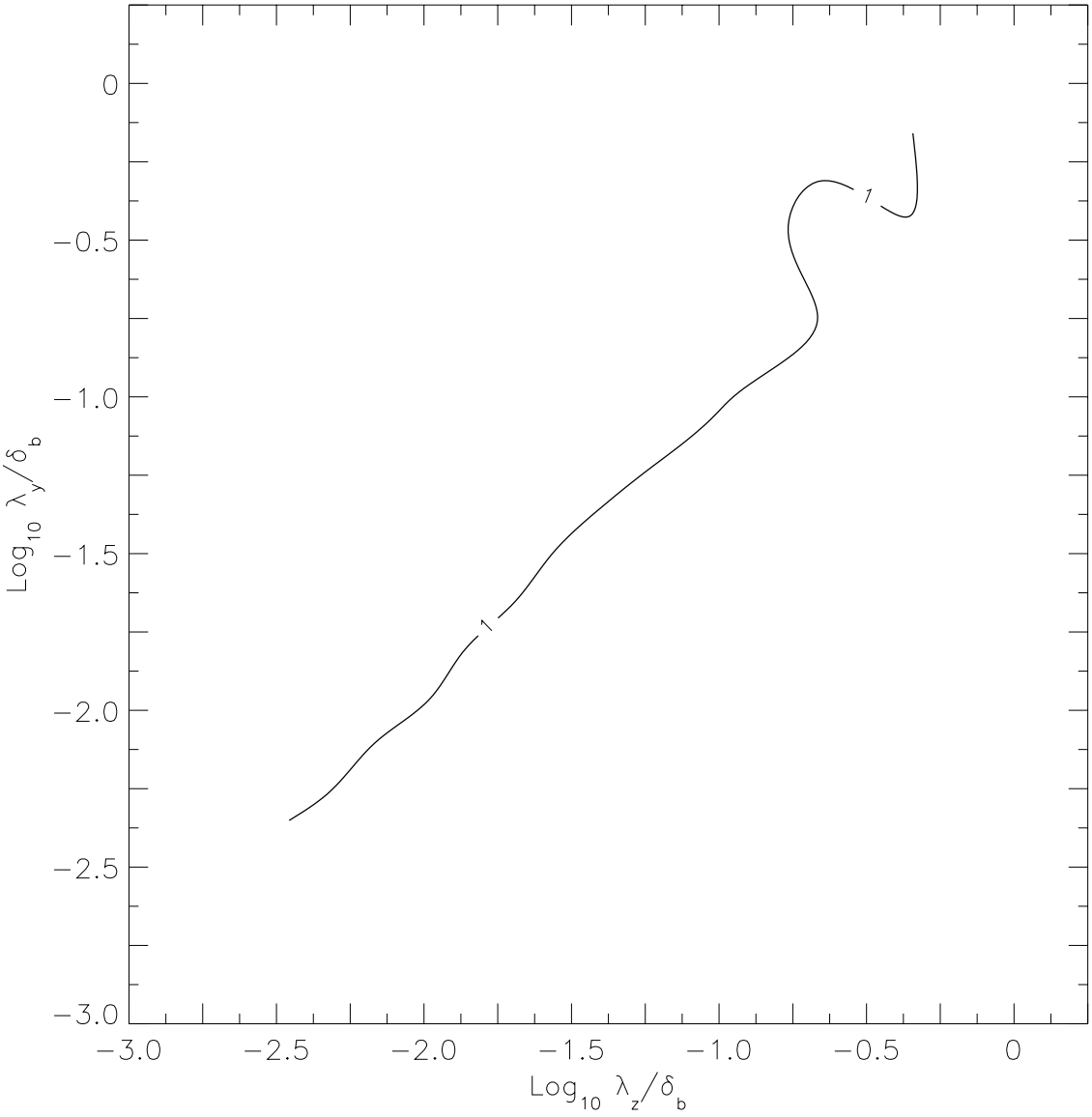

FIG. 7.6 $Re_{\rm j} = 1.0 \times 10^3$ and $C_{\rm iso} = 0.05$. Locus of points where partial derivatives of coverage $N(\lambda_z, \lambda_y)$ are equal. Departure of line from a 45^o line bisecting the axes indicates anisotropy of isoscalar surface at this concentration, $C_{\rm iso}$.

7.4 Anisotropy of transverse-jet isosurfaces

The iso-concentration surfaces of the transverse jet are anisotropic for the Reynolds numbers investigated, ranging from 1.0×10^3 to 20×10^3. The scale-dependent measure of anisotropy, $\beta(\lambda)$, is less than unity for small scales and crosses over to values larger than unity for large scales. This is an indication that, in the

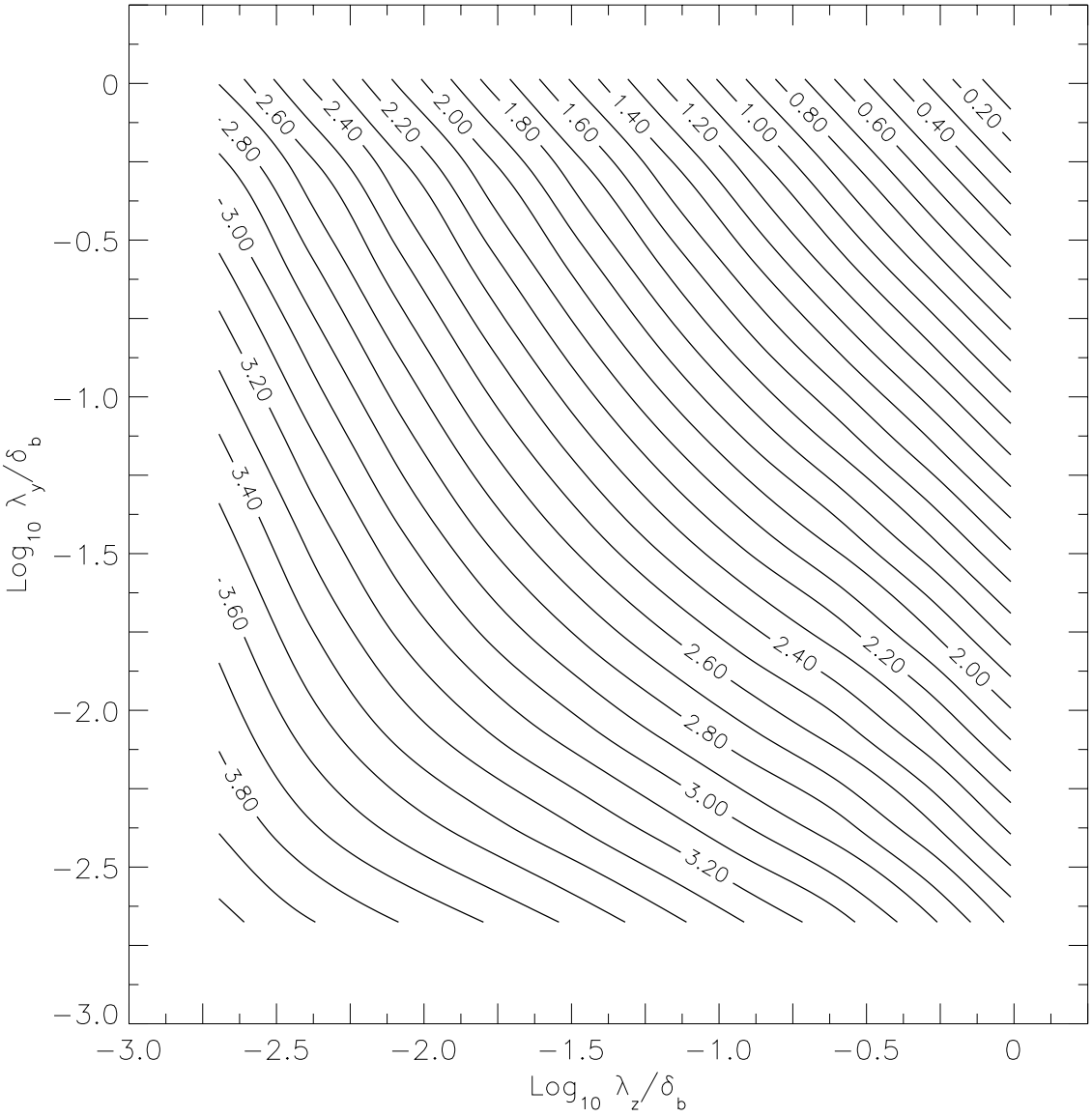

FIG. 7.8 Generalized coverage $N(\lambda_z, \lambda_y)$ of isoscalar surface for $C_{\rm iso} = 0.01$ at $Re_{\rm j} = 20 \times 10^3$, plotted as (base-10) logarithmic contours. Length scales nondimensionalized by bounding box size, δ_b, at this concentration level. Anisotropy of the set is seen in the lack of reflective symmetry about the 45^o line bisecting the axes.

isosurfaces produced by turbulent mixing in the transverse jet, vertically-stretched structure is found at small length scales, and horizontally-stretched structure at large scales. Essentially the same mechanism proposed in Ch. 5 is believed to be the cause of this anisotropy of the scalar isosurfaces. We offer some conjectures

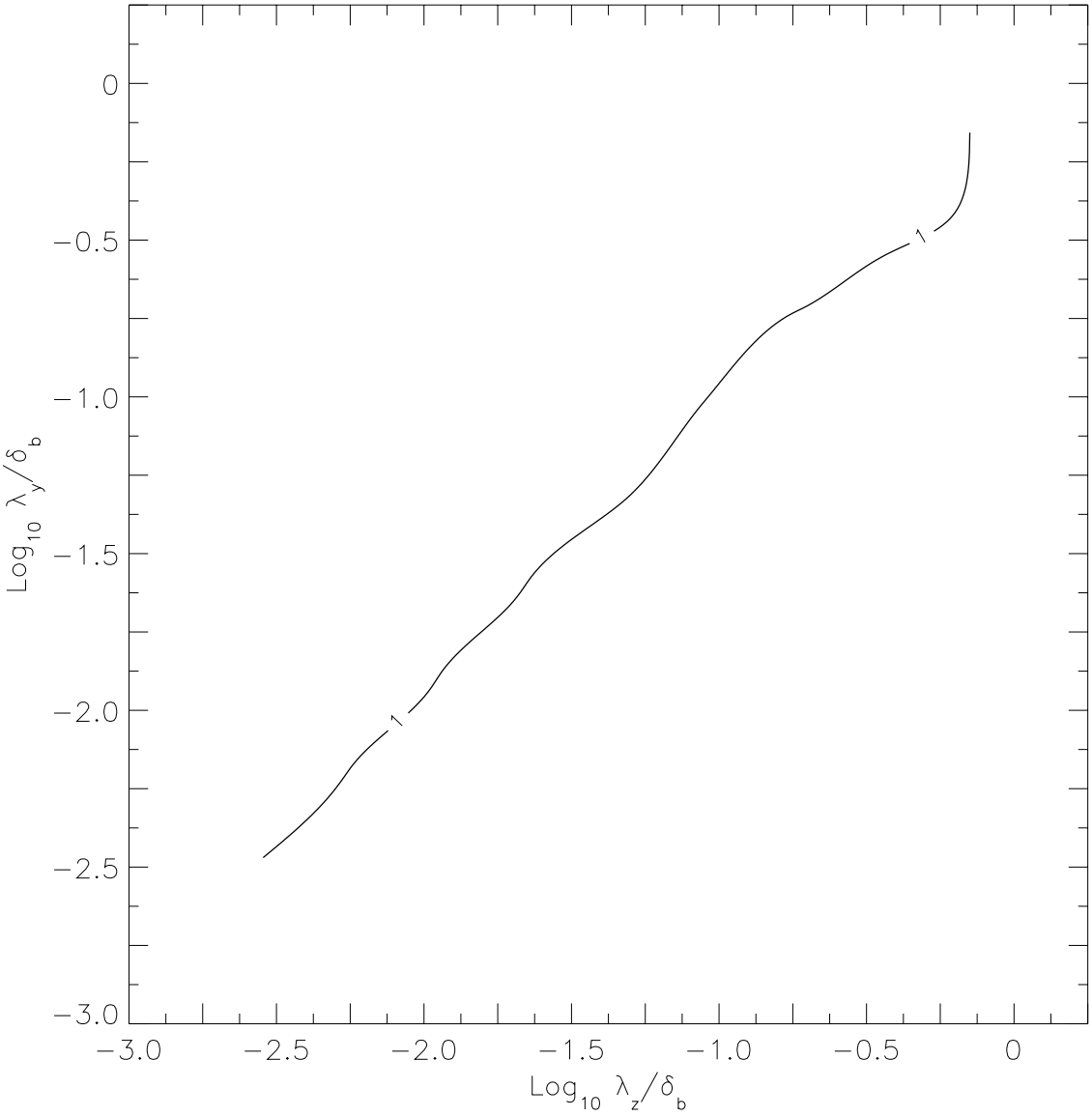

FIG. 7.9 $Re_{\rm j} = 20 \times 10^3$ and $C_{\rm iso} = 0.01$. Locus of points where partial derivatives of coverage $N(\lambda_z, \lambda_y)$ are equal, *i.e.*, where $\nabla N(\lambda_z, \lambda_y) \parallel (\widehat{\log z} + \widehat{\log y})$. These points are plotted as the line where $D_{C,1}/D_{C,2} = 1$. Departure of this line from a 45^o bisector of the axes indicates anisotropy of isoscalar surface at this concentration, $C_{\rm iso}$.

concerning the source of this anisotropy of the scalar isosurfaces. In the far field, the dynamics of the transverse jet are dominated by a counter-rotating vortex pair that defines the main body of the jet. The vortex pair also defines the large scales of the jet-fluid-concentration field, and its isosurface contours. The body of the jet

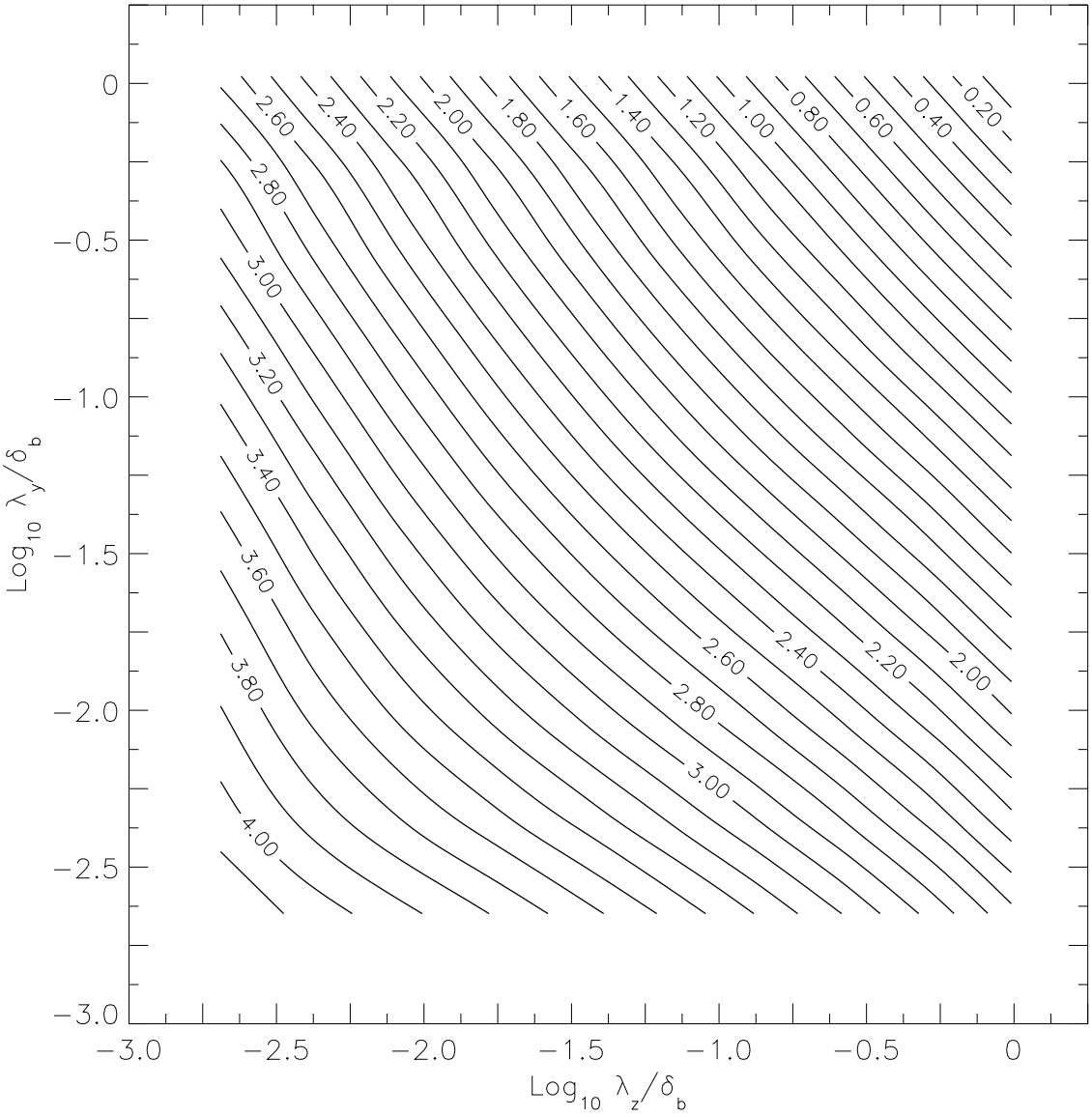

FIG. 7.10 Generalized coverage $N(\lambda_z, \lambda_y)$ of isoscalar surface for $C_{\rm iso} = 0.03$ at $Re_{\rm j} = 20 \times 10^3$.

is kidney-shaped and horizontally-elongated because of the side-by-side vortex pair, and thus produces isosurfaces that are horizontally stretched at large length scales. However, the counter-rotating vortex pair causes an extensional strain field, aligned vertically, which produces vertical "fingers" and other small-scale structures. This extensional strain is believed to be the source of the vertically-stretched structure of the scalar isosurface at small length scales.

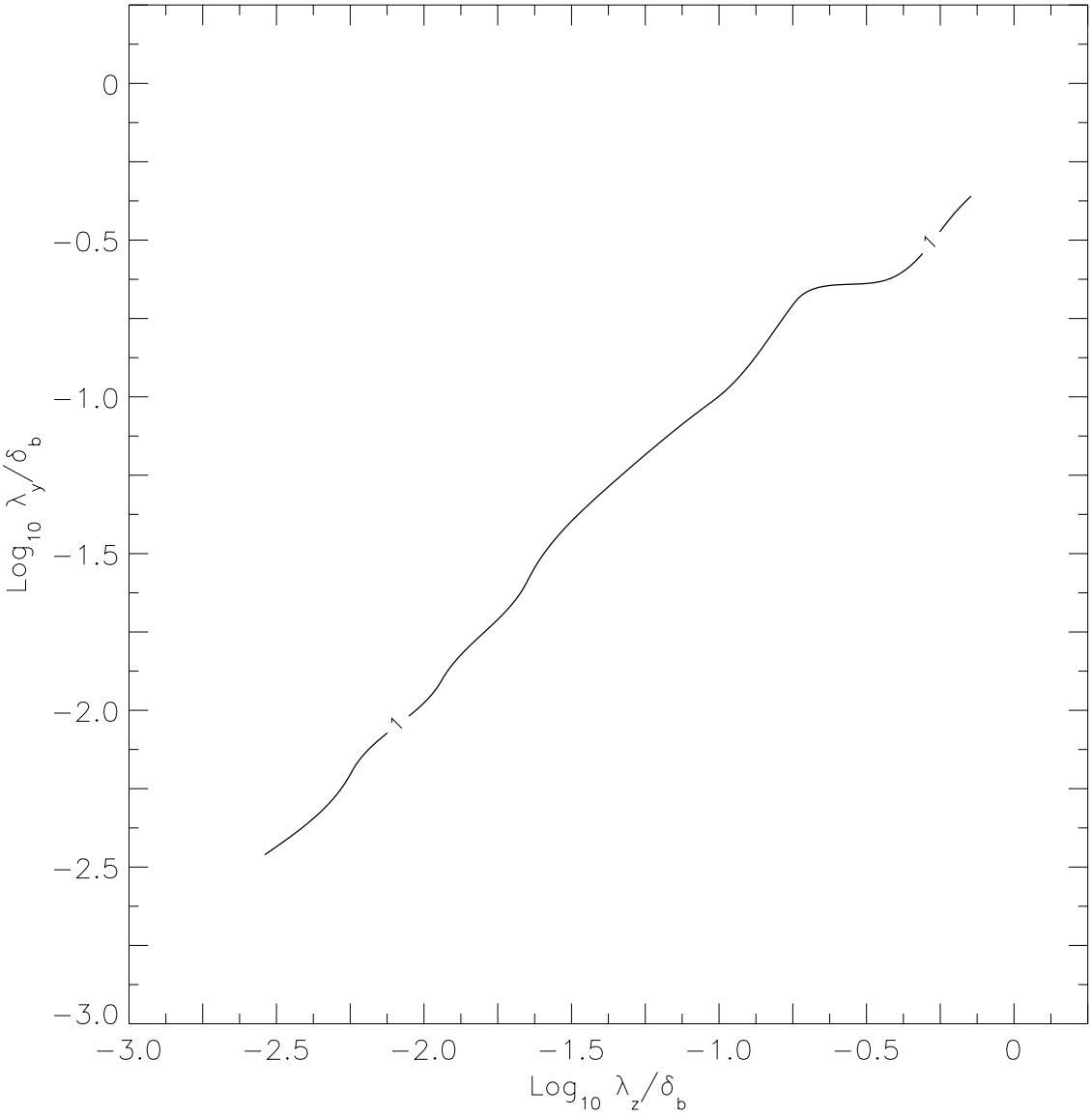

FIG. 7.11 $Re_{\rm j} = 20 \times 10^3$ and $C_{\rm iso} = 0.03$. Locus of points where partial derivatives of coverage $N(\lambda_z, \lambda_y)$ are equal. Departure of line from a 45^o line bisecting the axes indicates anisotropy of isoscalar surface at this concentration, $C_{\rm iso}$.

It should be borne in mind that anisotropy of level sets is distinct from anisotropy of the overall scalar field. In particular, $\beta(\lambda)$ is a measure of the anisotropy of the jet-fluid-concentration level set, $C(\mathbf{x}, t) = C_{\rm iso}$, while two-dimensional power spectra, directional PDFs of scalar increments, and scalar microscales are statistics of the entire scalar field, $C(\mathbf{x}, t)$. Although isosurfaces are level crossings of the scalar

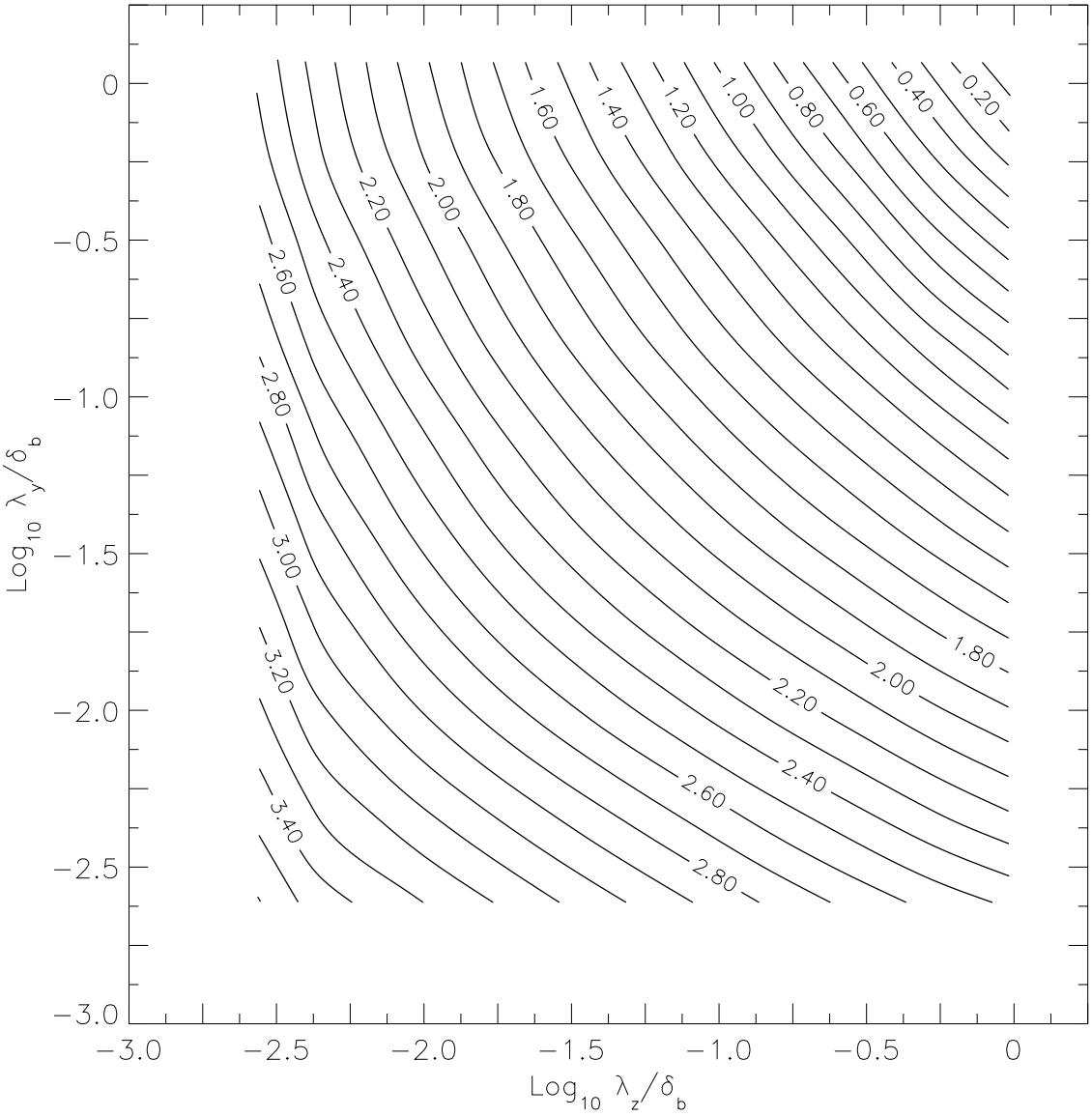

FIG. 7.12 Generalized coverage $N(\lambda_z, \lambda_y)$ of isoscalar surface for $C_{\rm iso} = 0.05$ at $Re_{\rm j} = 20 \times 10^3$.

field, direct connection can not be made between measures of the scalar field and measures of the geometric complexity of scalar isosurfaces. Information on the relative spacing of isosurfaces is lost when level sets are extracted from a scalar field.

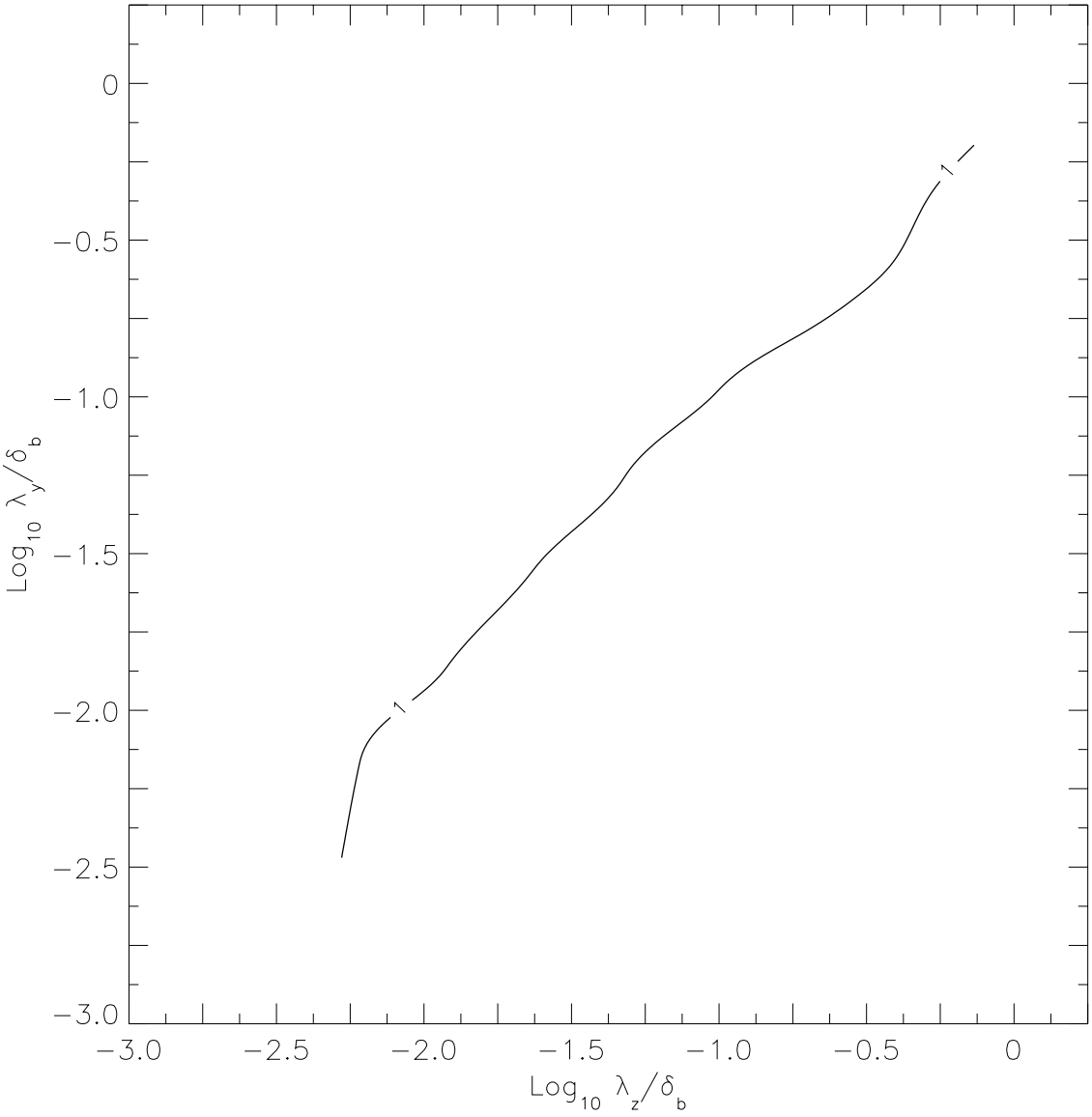

FIG. 7.13 $Re_{\rm j} = 20 \times 10^3$ and $C_{\rm iso} = 0.05$. Locus of points where partial derivatives of coverage $N(\lambda_z, \lambda_y)$ are equal. Departure of line from a 45^o line bisecting the axes indicates anisotropy of isoscalar surface at this concentration, $C_{\rm iso}$.

7.5 Special case: Isotropic coverage statistics

The special case of coverage with squares is considered. This is the usual box-counting approach, and allows comparison with the results of previous investigators (*e.g.*, Catrakis and Dimotakis 1996, larger review in Dimotakis and Catrakis 1996).

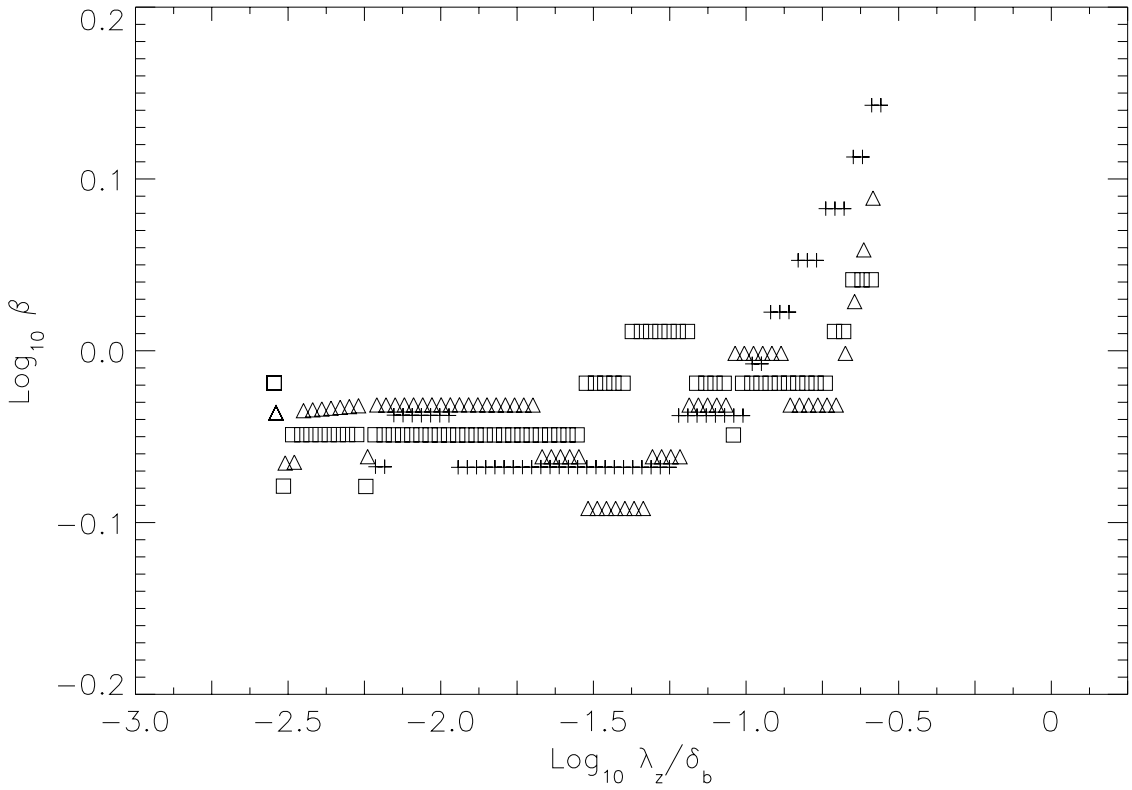

FIG. 7.14 Measured anisotropy of iso-concentration surface for $Re_{\rm j} = 20 \times 10^3$. Similar behavior to lower Reynolds case shown in Fig. 7.7. Small scales of isosurface contour are preferentially stretched ($\beta(\lambda) < 1$) in the vertical direction, $\widehat{\mathbf{y}}$, while large scales are preferentially stretched ($\beta(\lambda) > 1$) in the horizontal direction, $\widehat{\mathbf{z}}$. Squares: $C_{\rm iso} = 0.01$. Triangles: $C_{\rm iso} = 0.03$. Crosses: $C_{\rm iso} = 0.05$.

For the isotropic coverage statistics, (very-nearly) square coverage tiles are used to compute the coverage count as a function of scale, λ. Coverage length, $L_2(\lambda)$, coverage fraction, $F_2(\lambda)$, and the scale-dependent fractal dimension, $D_2(\lambda)$, are derived from the isotropic coverage count, $N_2(\lambda)$. These were investigated for scalar thresholds of $C_{\rm iso} = 0.01$, 0.03, and 0.05 for the transverse jet at $Re_{\rm j} = 20 \times 10^3$.

Figure 7.15 shows the ensemble-averaged coverage count, $N_2(\lambda)$, of isoscalar surfaces for three concentration values, with lines of increasing solidity denoting increasing scalar threshold. The coverage count is the ensemble average of six images of the jet-fluid concentration field at $x/d_{\rm j} = 50$. Spatial scales, λ, are normalized by $\delta_{\rm b}(C)$, the root-mean-square bounding-box size for each scalar threshold, defined

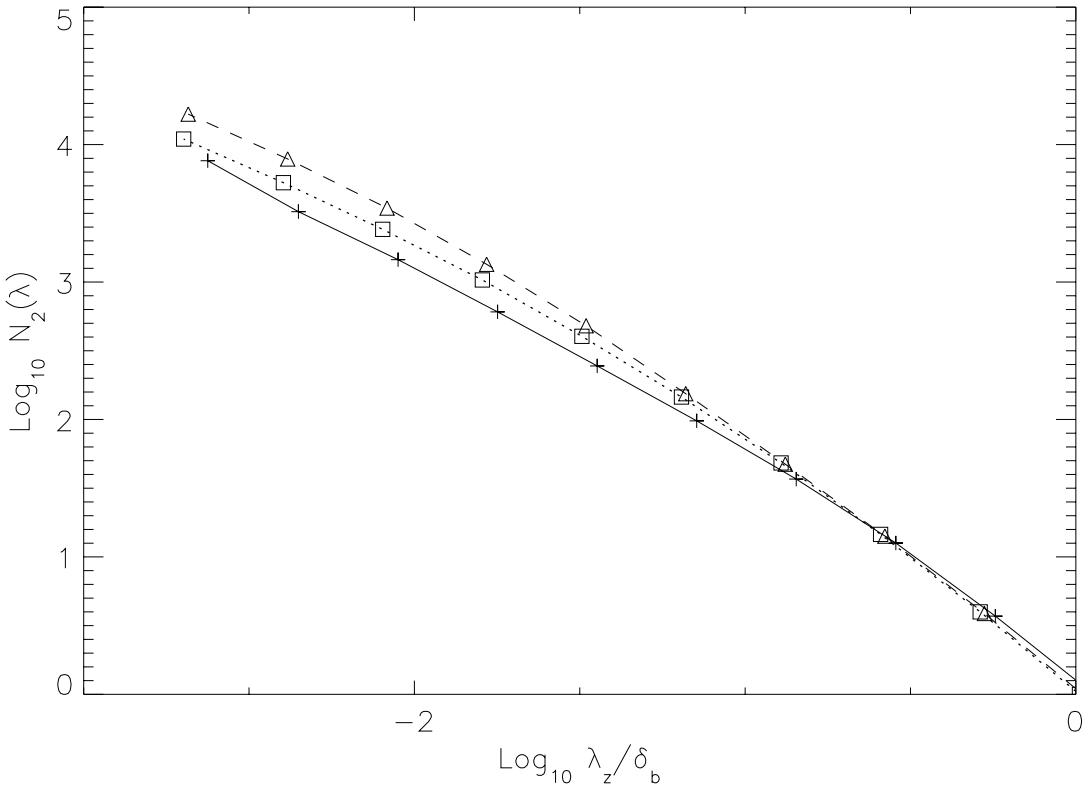

FIG. 7.15 Isotropic coverage count, $N_2(\lambda)$, for $Re_j = 20 \times 10^3$. Lines of increasing solidity indicate increasing isosurface concentration. Squares: $C_{iso} = 0.01$. Triangles: $C_{iso} = 0.03$. Crosses: $C_{iso} = 0.05$.

by Eq. 7.2. The coverage counts for the intermediate threshold, $C_{iso} = 0.03$, are seen to be larger than for $C_{iso} = 0.01$ or $C_{iso} = 0.05$. This corresponds to the peak in the scalar-field PDF near $C = 0.03$ (Fig. 4.1).

The scale-dependent coverage length, $L_2(\lambda)$, is shown in Fig. 7.16 for three jet-fluid concentrations, $C_{iso} = 0.01$, 0.03, and 0.05. Coverage length, defined as

$$L_2(\lambda) \equiv \lambda\, N_2(\lambda), \tag{7.3}$$

is a measure of the resolved isolength at scale λ. The intermediate concentration value is seen to have longer coverage lengths than the other concentration values. This corresponds to the peak in the scalar-field PDF at the same jet-fluid concentration, $C \simeq 0.03$. For the intermediate concentration threshold, the ratio of coverage length to bounding-box size reaches $L_2(\lambda)/\delta_b \simeq 10^{1.55} = 34.5$ in the limit of small

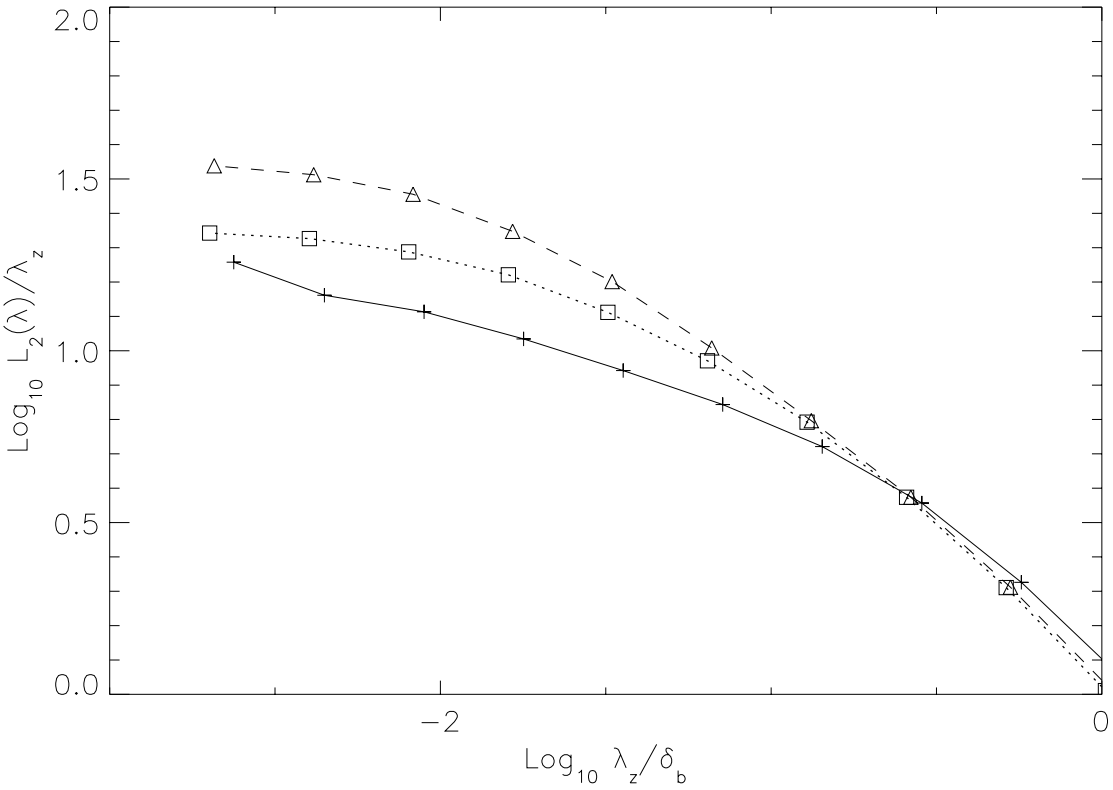

FIG. 7.16 Isotropic coverage length, $L_2(\lambda)$, for $Re_j = 20 \times 10^3$. Lines of increasing solidity indicate increasing isosurface concentration. Squares: $C_{iso} = 0.01$. Triangles: $C_{iso} = 0.03$. Crosses: $C_{iso} = 0.05$.

length scales, *i.e.*, $\lambda/\delta_b \to 0$. The asymptotic behavior of the coverage length is an indication that the measurements are spatially well-resolved. The perimeter of the bounding box is estimated to be $4\delta_b$, since the bounding box is nearly square. Thus, turbulent mixing in the high Schmidt-number transverse jet produces isoscalar contours with small-scale coverage lengths that are $34.5/4 \simeq 8.8$ times longer than the perimeter of the bounding box. For comparison, in the turbulent jet discharging into a quiescent reservoir, the asymptotic value of the ratio of coverage length to perimeter of bounding-box was found to be approximately 11 at an intermediate concentration (Catrakis and Dimotakis 1996).

The coverage fraction, $F_2(\lambda)$, is plotted in Fig. 7.17 for scalar thresholds of $C_{iso} = 0.01$, 0.03, and 0.05 for the transverse jet at $Re_j = 20 \times 10^3$. This statistic is again estimated from the ensemble average of six individual coverage counts.

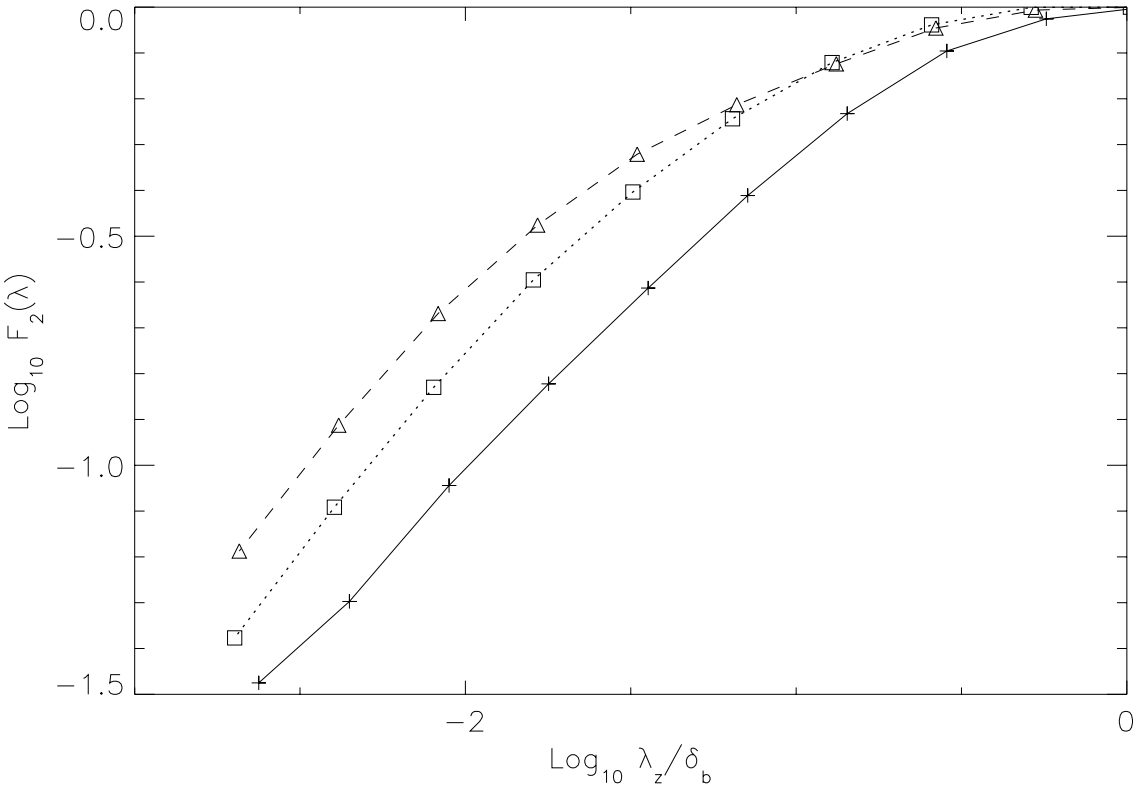

FIG. 7.17 Isotropic coverage fraction, $F_2(\lambda)$, for $Re_j = 20 \times 10^3$. Lines of increasing solidity indicate increasing isosurface concentration. Squares: $C_{\rm iso} = 0.01$. Triangles: $C_{\rm iso} = 0.03$. Crosses: $C_{\rm iso} = 0.05$.

Coverage fraction at a length-scale λ is defined from the coverage count, $N_2(\lambda)$, as

$$F_2(\lambda) \equiv \frac{N_2(\lambda)}{N_{2,\rm total}} = \left(\frac{\lambda}{\delta_{\rm b}}\right)^2 N_2(\lambda),$$

where $N_{2,\rm total}$ is the total number of two-dimensional boxes of size λ that can fit in the bounding box of size $\delta_{\rm b}$. It may be identified as the probability that a λ-sized box, randomly placed in the bounding box, will contain (*i.e.*, "cover") part of the set (Dimotakis 1991, Catrakis and Dimotakis 1996). The coverage fraction is seen to decrease monotonically from unity with decreasing scale. Coverage fraction is largest for the intermediate concentration, $C_{\rm iso} = 0.03$.

Finally, the scale-dependent coverage dimension, $D_2(\lambda)$, computed from the ensemble-averaged coverage counts, is shown in Fig. 7.18. Three concentration values, $C_{\rm iso} = 0.01$, 0.03, and 0.05, are considered, with lines of increasing solidity

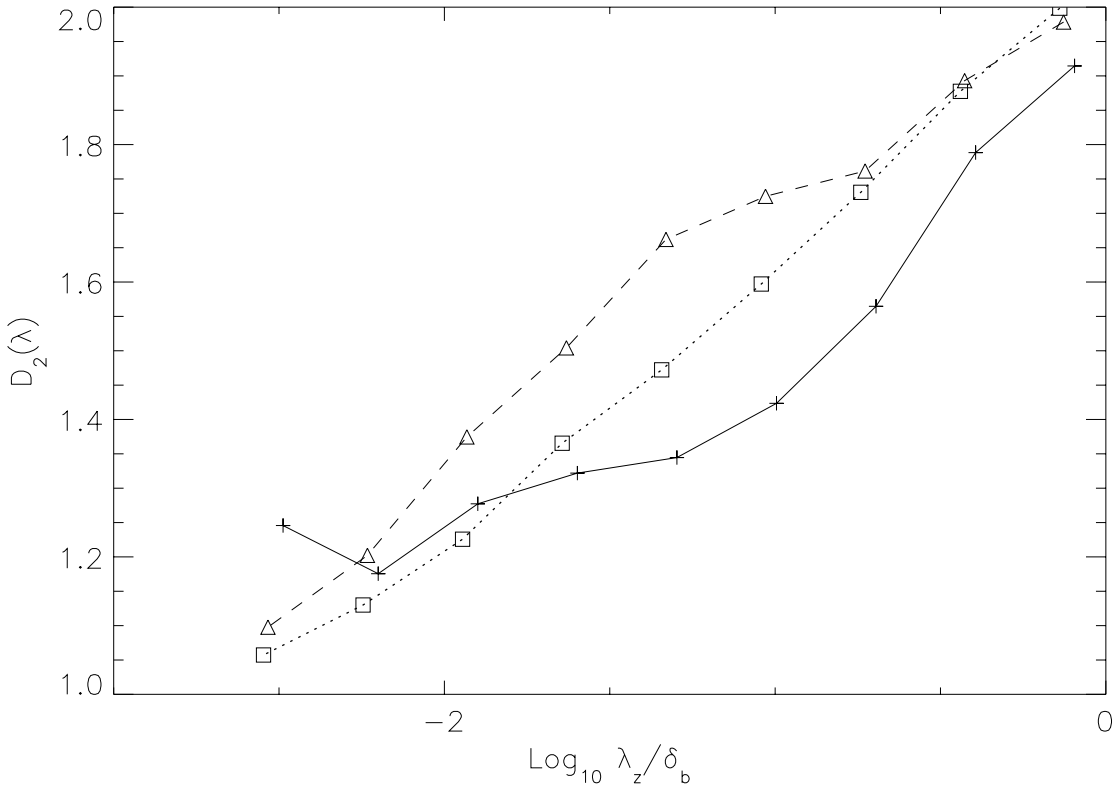

FIG. 7.18 Scale dependent fractal dimension, $D_2(\lambda)$, for $Re_j = 20 \times 10^3$ computed from isotropic coverage counts. Lines of increasing solidity indicate increasing isosurface concentration. Squares: $C_{\mathrm{iso}} = 0.01$. Triangles: $C_{\mathrm{iso}} = 0.03$. Crosses: $C_{\mathrm{iso}} = 0.05$.

denoting increasing scalar threshold. The coverage dimension, defined in Eq. 6.1, is seen to vary smoothly between unity, at the smallest scales, to 2 at the largest scales. These bounds are the topological dimension, and the embedding dimension, respectively. The variation of coverage dimension with length scale is consistent with the results of Miller and Dimotakis (1991), and Catrakis and Dimotakis (1996), indicating that isosurfaces produced by turbulent mixing are more complicated than can be described by a power-law fractal description.

CHAPTER 8

Conclusions

Reynolds number effects and flow dependence of PDF of scalar concentration — Enhanced scalar mixing, *i.e.*, better spatial homogenization, with increasing Reynolds number is found in experimental investigations of liquid-phase transverse jets in the range $1.0\times10^3 \leq Re_{\mathrm{j}} \leq 20\times10^3$. Classical measures of the jet, such as scalar trajectory and maximum mean-concentration decay, are seen to be independent of Reynolds number. However, the probability density function of jet-fluid-concentration evolves with Reynolds number. In the far field of the transverse jet, the scalar PDF evolves from a monotonically-decreasing function to a strongly-peaked distribution with increasing Reynolds number. The behavior of the PDF is explained as a consequence of the competition between entrainment, stirring, and molecular mixing. Turbulent mixing is seen to be flow dependent, based on the difference between the trends with increasing Reynolds number for the transverse jet, and the jet discharging into a quiescent reservoir.

Scalar increment PDF — A technique for whole-field computation of scalar differences is introduced and applied to experimentally-measured scalar fields in the transverse jet. The PDFs of scalar differences are found to tend toward long-tailed distributions with decreasing separation distance. These exponential, or stretched-exponential, PDFs of scalar differences are found despite the inhomogeneity, anisotropy, and non-Gaussian distribution of the scalar field in the transverse jet. This result is consistent with investigations in grid-turbulence, Rayleigh-Benard convection, and other turbulent flows.

Anisotropy of scalar field — The scalar field is seen to be inhomogeneous and anisotropic with decreasing scale. Two-dimensional power spectra of jet-fluid concentration in the far field of the jet are found to be isotropic for low wavenumbers, and increasingly anisotropic for higher wavenumbers. This anisotropy at small

scales is also reflected in the directional dependence of the PDF of scalar increments. PDFs of scalar increments are narrower for small, vertical increments than for small, horizontal increments. The scalar field has less variation (in terms of PDFs of scalar increments, and scalar structure functions) in the vertical direction than in the horizontal direction. The small-scale anisotropy of the scalar field persists from the lowest Reynolds numbers investigated, $Re_{\mathrm{j}} = 1.0 \times 10^3$, to the highest Reynolds numbers studied, $Re_{\mathrm{j}} = 20 \times 10^3$. Further evidence for the anisotropy of the scalar field is also seen in the directional dependence of the scalar microscales. The observed, small-scale, anisotropy of the scalar field is believed to be a consequence of extensional strain in the vertical direction caused by the dominant, kidney-shaped vortex pair in the transverse jet. The anisotropic, large-scale flow imposes itself on even the smallest features of the scalar field.

Generalized coverage for anisotropic geometries — We introduce coverage statistics suitable for describing complex, anisotropic sets. The ordinary (isotropic, fractal) coverage count is generalized to consider coverings with anisotropic, d-dimensional parallelepipeds. A scale-dependent measure of anisotropy is defined by the normalization required to transform the anisotropic set to local coverage isotropy. The generalized coverage and scale-dependent anisotropy are derived and computed for simple examples of an ordinary figure (rectangular perimeter), and an anisotropic fractal (Sierpinski carpet).

Complexity and anisotropy of isosurfaces in transverse jets — Level sets of jet-fluid concentration in the turbulent transverse jet are found to be anisotropic at both small and large scales. The scale-dependent measure of anisotropy, $\beta(\lambda)$, is less than unity for small scales, and crosses over to values larger than unity for large scales, indicating a preference for vertically-stretched structures at small length scales, and horizontally-stretched structures at large length scales. The small-scale anisotropy is attributed to the extensional strain caused by the vortex pair, and large-scale anisotropy is associated with the kidney-shaped, horizontally-elongated cross-section of the transverse jet. For the special case of isotropic box-counting, the scale-dependent coverage dimension is found to vary from unity, at the smallest length scales, to 2, at the largest length scales. The isosurfaces produced by turbulent mixing are more complicated than can be described by power-law fractals.

APPENDIX A

Probability density functions in d-dimensional space

The PDF for a distribution, $C(\mathbf{r})$, in d-dimensional space is the differential d-dimensional volume, $\mathrm{d}V_d(C)$, associated with a differential concentration, $\mathrm{d}C$,

$$f_d(C) \;=\; \frac{1}{V_{d,\mathrm{tot}}} \left| \frac{\mathrm{d}V_d(C)}{\mathrm{d}C} \right| \;.$$

Normalization by the total volume, $V_{d,\mathrm{tot}}$, is necessary so that the PDF has the properties discussed in Ch. 4, and proper dimensions, $1/C$.

Consider, for instance, the Gaussian scalar distribution,

$$C(r,t) \;=\; \frac{1}{2^d(\pi\mathcal{D}t)^{d/2}}\, e^{-r^2/4\mathcal{D}T} \;=\; \frac{1}{(2\pi)^{d/2}\sigma^d}\, e^{-r^2/2\sigma^2} \;. \tag{A.1}$$

This is the solution to the d-dimensional initial-value problem for the diffusion equation on an infinite domain with initial conditions of a delta function at the origin, $C(\mathbf{r}, t=0) = \delta(\mathbf{r})$. Here, $\sigma^2 = 2\mathcal{D}t$. The differential length, $\mathrm{d}r$, at any given time (*i.e.*, σ =constant) is related to $\mathrm{d}C$ by

$$\frac{\mathrm{d}r}{\mathrm{d}C} \;=\; -\,\frac{(2\pi)^{d/2}\sigma^d}{2r}\, e^{r^2/2\sigma^2} \;. \tag{A.2a}$$

Using (A.1), $\mathrm{d}r/\mathrm{d}C$ can be written as a function of C alone:

$$\frac{\mathrm{d}r}{\mathrm{d}C} \;=\; \frac{1}{2\,C\,r} \;=\; \frac{1}{2\sigma C \left\{ -2\ln\left[(2\pi)^{d/2}\sigma^d C \right] \right\}^{1/2}} \;. \tag{A.2b}$$

The differential d-dimensional volume $\mathrm{d}V_d(C)$ may then be expressed as a function of C using (A.1) and (A.2) to yield the form of the PDF for a d-dimensional Gaussian distribution:

$$f_d(C) \;\propto\; \frac{\left[\ln(1/C)\right]^{d/2-1}}{C} \;. \tag{A.3}$$

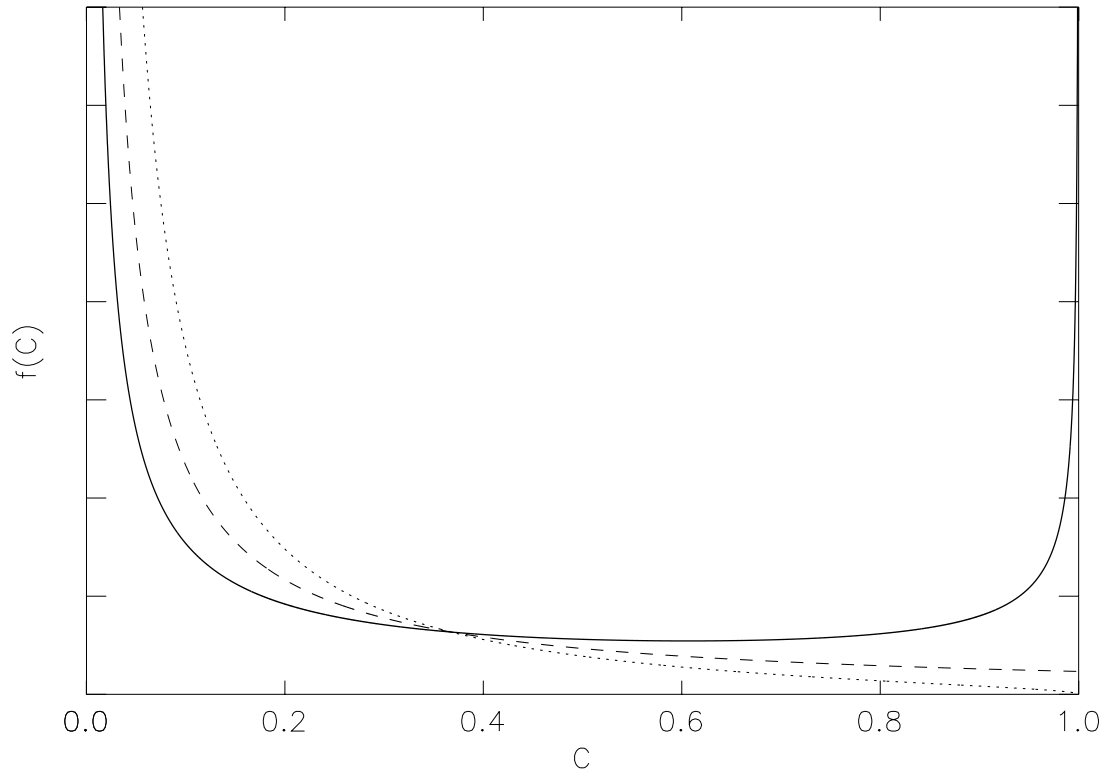

FIG. A.1 PDFs of diffusive (Gaussian) distributions $C(r)$. Solid line: one-dimensional. Dashed line: two-dimensional. Dotted line: three-dimensional.

The PDF for a one-dimensional Gaussian-concentration distribution is then:

$$f_1(C) \;\propto\; \frac{1}{C\,[\,\ln(1/C)\,]^{1/2}} \;. \tag{A.3a}$$

This function, which is shown in Fig. A.1, peaks at $C = 0$ and $C = 1$.

For a two-dimensional Gaussian distribution, $\mathrm{d}A = 2\pi r \mathrm{d}r = \pi/C$, and the PDF is proportional to $1/C$,

$$f_2(C) \;\propto\; \frac{1}{C} \;. \tag{A.3b}$$

The PDF peaks at $C = 0$ and decreases monotonically to a (non-zero) minimum at $C = 1$ (Fig. A.1).

Similarly, for a three-dimensional Gaussian, $\mathrm{d}V = 4\pi r^2 \mathrm{d}r$, and the PDF is proportional to $[\ln(1/C)]^{1/2}/C$,

$$f_3(C) \;\propto\; \frac{[\,\ln(1/C)\,]^{1/2}}{C} \;. \tag{A.3c}$$

This function peaks at $C = 0$ and decreases monotonically to $f(1) = 0$ (Fig. A.1).

D-dimensional transects of a higher-dimensional Gaussian are themselves d-dimensional Gaussians. For this reason, the PDFs discussed above can be viewed as PDFs of concentration distributions in d-dimensional space, or as d-dimensional measurements of a higher-dimensional distribution. The shape of a PDF can depend on the dimensionality of the space (or measurement), as well as the distribution, $C(\mathbf{r})$.

APPENDIX B

Three-dimensional isosurface visualization

The streamwise velocity deficit of the transverse jet, relative to the freestream velocity, decays rapidly with downstream distance (*e.g.*, Yuan and Street 1998). Far downstream from the jet exit ($x/d_{\rm j} \gg 1$), the streamwise velocity of the jet is approximately the freestream velocity, $U_x \simeq U_\infty$. Taylor's frozen flow hypothesis may then be used to approximate spatial coordinates with scaled time coordinates,

$$x \;=\; \frac{U_x}{t} \;\simeq\; \frac{U_\infty}{t}. \tag{B.1}$$

The transverse jet is in this sense a flow geometry that is well-suited for three-dimensional measurements of the scalar field. A three-dimensional, pseudo-spatial measurement of the scalar field can be assembled by recording a time sequence of transverse slices of the jet-fluid concentration field at fixed $x/d_{\rm j} \gg 1$. The temporal sampling requirement for assembling three-dimensional spatial concentration fields is that the sample period be less than advection time of diffusion scales in the streamwise direction:

$$t_{\rm sample} \;\leq\; \frac{\lambda_{\mathcal{D}}}{U_\infty}. \tag{B.2}$$

The diffusion scale, $\lambda_{\mathcal{D}}$, is estimated in Ch. 2 to be 4.6 pixels, translating to 0.11 cm, for the $Re_{\rm j} \simeq 1.0 \times 10^3$ jet. For velocity ratio $V_{\rm r} = 10.1$, the freestream velocity is $U_\infty = 1.3$ cm/s. The advection time of diffusion scales is estimated to be $\lambda_{\mathcal{D}}/U_\infty \simeq 0.08$ seconds using Eq. B.1. Thus, the 10 Hz framing rate of the Cassini camera is close to resolving the diffusion scale in streamwise direction for $Re_{\rm j} \simeq 1.0 \times 10^3$ (Eq. B.2). The corresponding advection time for diffusion scales in the $Re_{\rm j} \simeq 2.0 \times 10^3$ jet is 0.04 seconds. In particular, the streamwise direction is resolved to 1.25 times the scalar-diffusion scales at $Re_{\rm j} \simeq 1.0 \times 10^3$. The framing rate is only sufficient to resolve 2.5 times the scalar-diffusion scales in the streamwise direction at $Re_{\rm j} \simeq 2.0 \times 10^3$.

APPENDIX C

Vorticity generation and dynamics

The primary vortical structures of the transverse jet are summarized in Fig. C.1: the dominant counter-rotating vortex pair, jet shear-layer vortices, horseshoe vortices, and wake vortices. The wake vortices, which extend from the jet toward the injection plane, are similar in appearance to the vortices shed by circular cylinders above a critical Reynolds number. Although periodic motions in the wake of the transverse jet were noted by several early investigators (Gordier 1959, McAllister 1968, Reilly 1968, McMahon *et al.* 1971, Moussa *et al.* 1977), Kuzo and Roshko (1984) were the first to directly visualize the wake vortices. Fric and Roshko (1994) subsequently noted that the sources of vorticity for the transverse jet are distinct from those of the circular cylinder. In particular, vorticity cannot be generated within an incompressible, Newtonian flow, in the absence of body forces, and must originate from boundaries. Flow visualizations suggested that the wake vorticity in the transverse jet originated in the cross-flow wall boundary layer, rather than in jet shear layer. This led Fric and Roshko to conclude that separation events occurred periodically on the crossflow wall to redirect wall-parallel boundary-layer vorticity into wall-normal wake vortices.

Although the primary focus of this thesis is on mixing and isosurface geometry, some flow visualization experiments were conducted on vortical structures in the wake of a transverse jet. In order to study the influence of cross-flow boundary conditions on the wake vortices, the jet was injected through a free surface and compared to the jet injected through a surface plate. Laser-induced fluorescence was used to visualize the wake structure of the transverse jet for velocity ratio $V_{\mathrm{r}} = 10.1$ and $Re_{\mathrm{j}} = 10 \times 10^3$. Fluorescent dye was introduced with a fine needle upstream of the jet nozzle and entrained into the wake vortices. The wake region of the transverse jet was visualized by spreading the beam from a Nd:YAG laser into a 3-D volume, and recording images with the Cassini camera.

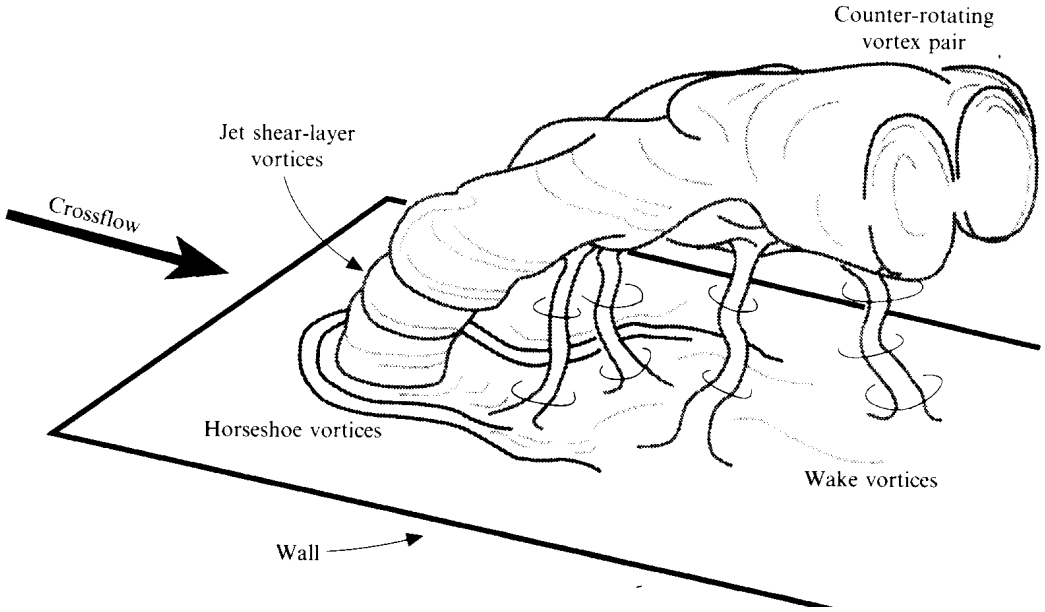

FIG. C.1 Vortical structures in the transverse jet, from Fric and Roshko (1994).

The jet was first discharged through the laminar boundary layer of a surface plate. A flat plate with a 4:1 elliptical leading edge was installed in the test section, and the tunnel water level was adjusted to graze the surface plate. The jet exited through a flush-fitting, convex-contoured nozzle with a 44:1 area contraction ratio (Fig. C.2). The boundary layer on the surface plate was laminar ($Re_x = U_\infty x/\nu < 20 \times 10^3$) and thin ($\delta \simeq O(d_\mathrm{j})$) at the jet exit. This was verified with hydrogen-bubble visualizations of the boundary layer, shown in Fig. C.3.

A frame from a sequence of volume-illuminated LIF images is shown in Fig. C.4. The dye enters the field of view from the left, passes around the jet core, and is entrained by the wake vortices. The sequence of images shows axial flow in the core of the wake vortices, pulling dye from the wall, toward the body of the jet. Vorticity in the newly-formed wake vortices (close to jet exit) is rapidly amplified by vertical straining along the vortex axis as the jet body penetrates deeper into the freestream. The wake vortices are counter-rotating, and sometimes cut and reconnect to form upside-down U-shaped vortices, as seen in Fig. C.4.

After it was demonstrated that wake vortices could be visualized with LIF volume illumination in the case of the jet issuing through a wall boundary layer, the

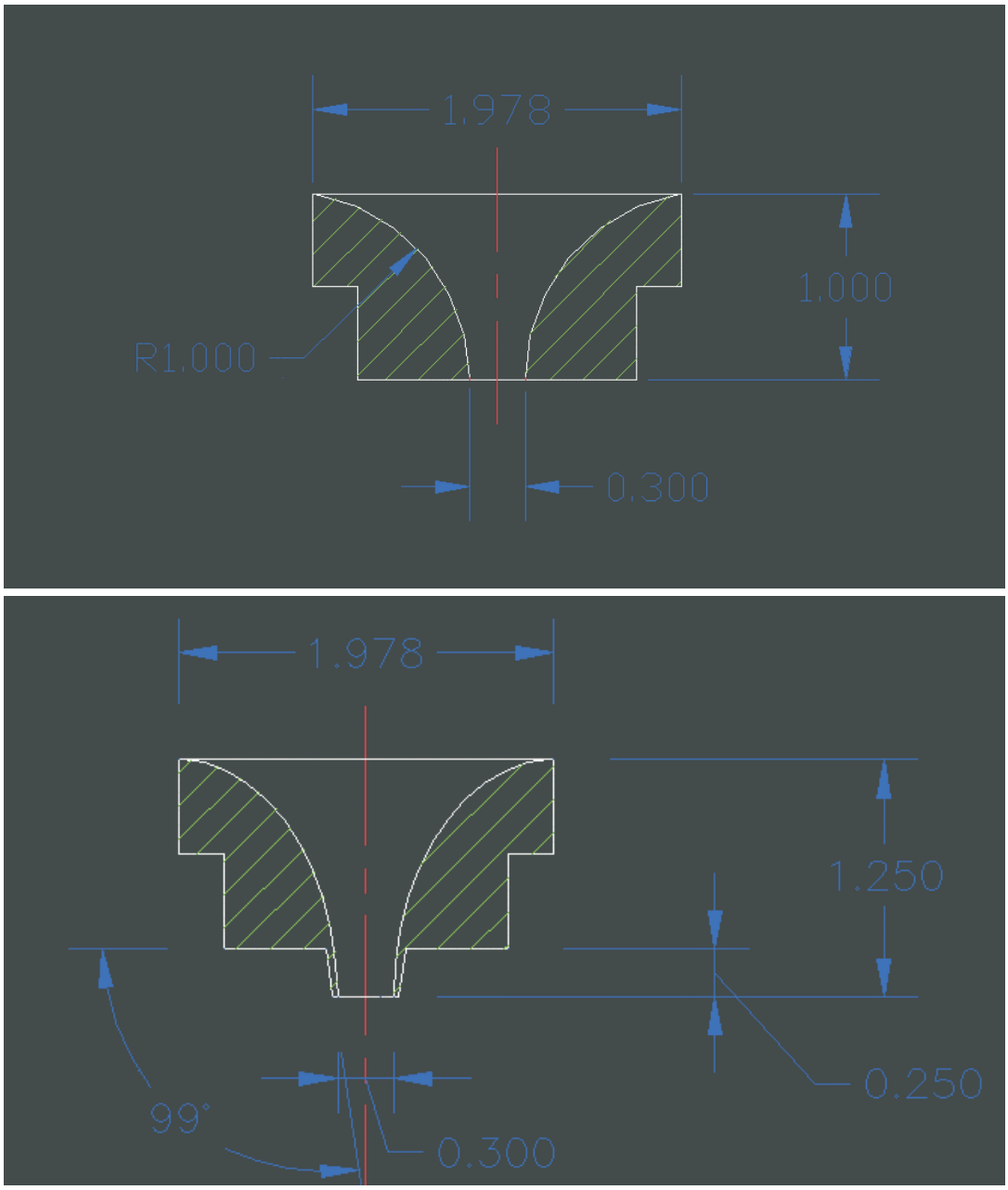

FIG. C.2 Nozzles used to create jets. Both nozzles are convex-contoured (to suppress Gortler vortices) and have 44:1 area contraction ratio. Left: Nozzle that fitted flush to surface plate. Right: Nozzle used to inject jet through free surface.

transverse jet was injected through a free surface. The water level in the tunnel was lowered to a height below the surface plate and the jet was injected with a surface-

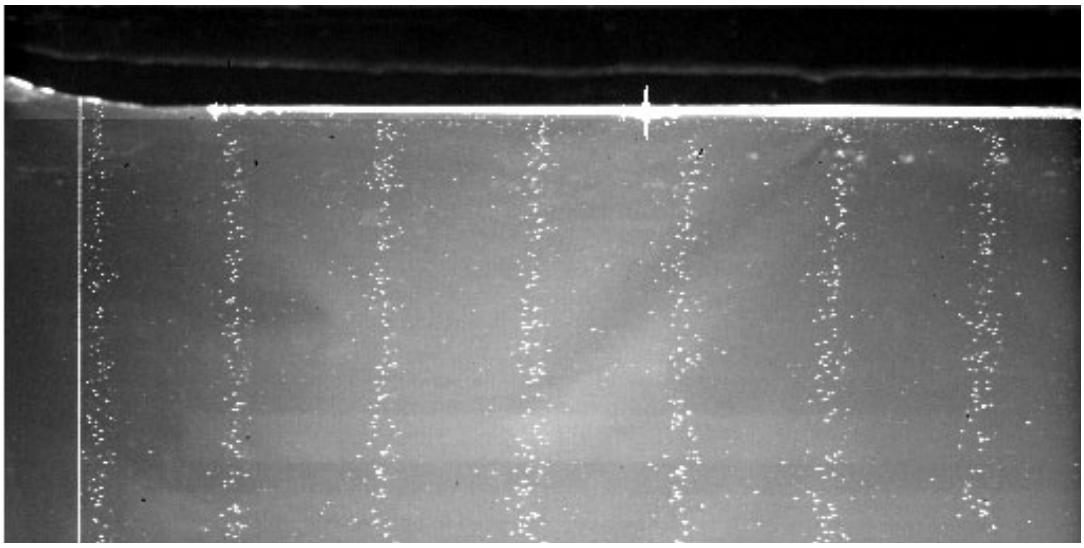

FIG. C.3 Hydrogen-bubble visualization of the thin, laminar boundary layer on surface plate. $Re_x < 20 \times 10^3$ at jet exit, and $\delta \simeq O(d_j)$. Flare in the shape of a "cross" is approximate location of nozzle.

piercing nozzle (Fig. C.2). Free-surface curvature and surface tension gradients were negligible, and hydrogen bubble visualization showed no evidence of a boundary layer at the free surface (Fig. C.5).

A volume-illuminated LIF image of the jet injected through the free surface is shown in Fig. C.6. Despite the absence of wall boundary-layer vorticity upstream of the jet exit, wake vortices are seen. In a fashion similar to the wall-bounded transverse jet, the counter-rotating wake vortices are amplified by the overall jet trajectory, and exhibit axial flow from the free-surface to the jet body. Unlike the wall-bounded jet, however, the wake vortices of the free-surface jet can connect to the surface.

Our experiments with free-surface transverse jets demonstrate that wall-boundary-layer vorticity is not necessary for the formation of wake vortices in transverse jets. Since no vorticity generation is possible within an incompressible, Newtonian fluid in the absence of body forces, vorticity in the transverse jet wake (as well as in the main body of the jet) must enter through imposed boundary and initial conditions. There are several possibilities for the source of vorticity for wake vortices in free-surface jets:

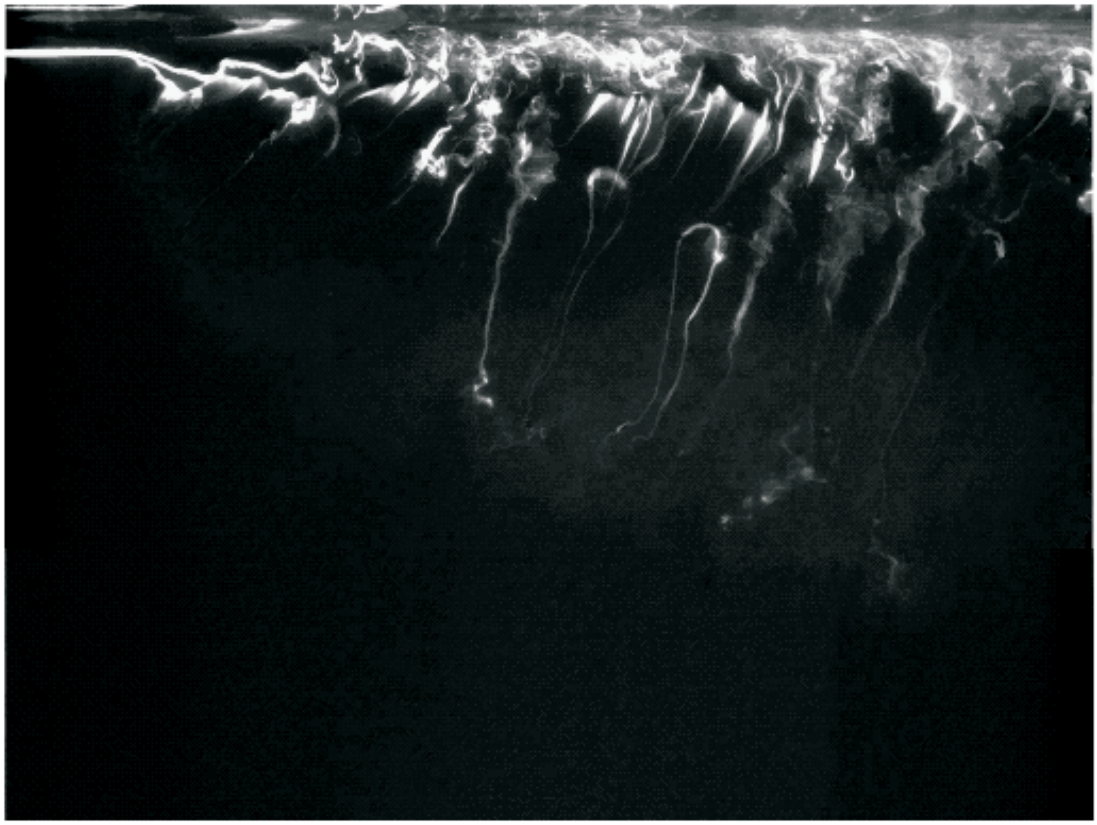

FIG. C.4 Wake vortices for transverse jet injected through laminar boundary layer of surface plate. $Re_{\rm j} = 10 \times 10^3$ and $V_{\rm r} = 10.1$.

Vorticity could be generated because of free-surface unsteadiness, or flow along a curved free surface (*e.g.*, Sarpkaya 1996). To motivate this, consider two-dimensional, free-surface flow. The vorticity at a free surface may be expressed in terms of the local and tangential components of the velocity field (Lugt 1987, Longuet-Higgins 1992, Wu 1995, Lundgren and Koumoutsakos 1999):

$$\omega \;=\; -2\frac{\partial \mathbf{u}}{\partial s}\cdot\widehat{\mathbf{n}} \;=\; -2\frac{\partial \mathbf{u}\cdot\widehat{\mathbf{n}}}{\partial s} + 2\mathbf{u}\cdot\frac{\partial \widehat{\mathbf{n}}}{\partial s}\,. \tag{C.1}$$

The first term on the right is relevant for unsteady free surfaces, and the second term for flows along a curved free surface. This equation, which is a kinematic consequence of the zero shear stress condition at a free surface, is also derived for three-dimensional flow by Lundgren (1989). Regardless of how it is generated (*e.g.*, by flow along a curved free-surface, or by surface-tension gradients), the vorticity at an unsteady free-surface, as given by Eq. C.1, can then diffuse into the bulk flow, or

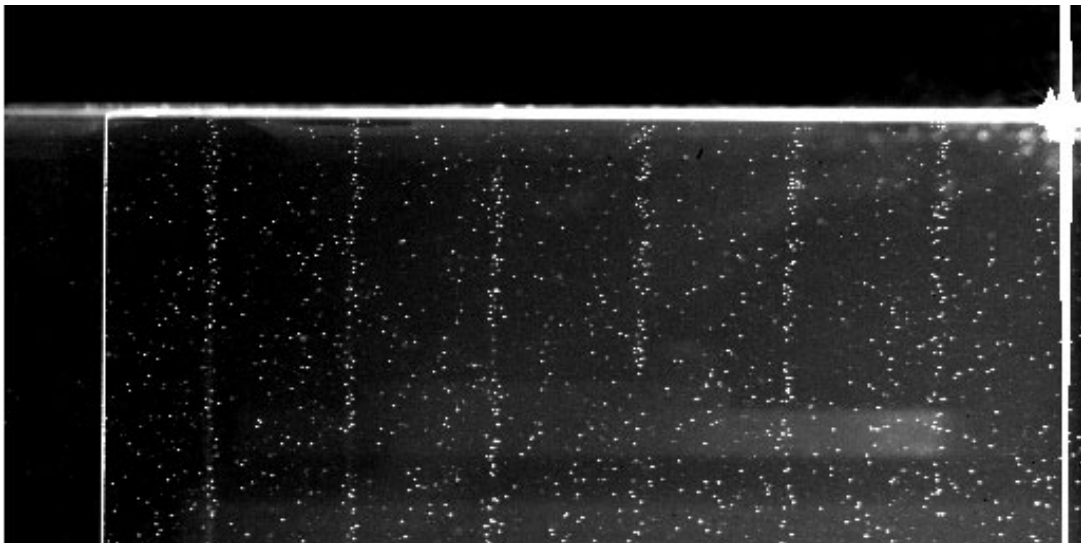

FIG. C.5 Hydrogen bubble visualization of free-surface. No free-surface curvature, and negligible surface-tension gradients (Reynolds ridge is downstream of test section at these conditions). Hence, no boundary-layer vorticity is evident.

be transported by surface-normal flow. Our visualizations show that the transverse jet does indeed induce free-surface curvature in the form of two depressions, or "dimples", on the downstream lateral sides of the jet (Fig. C.7). These dimples are unsteady, with a period that are not dissimilar to the period of alternating-signed wake vortices. It is likely that unsteadiness of the free surface, and/or flow along a curved free surface, produces vorticity on the free surface through which the transverse jet is injected. What is not understood, however, why this would produce a pattern of wake vortices so similar to that of the wall-bounded transverse jet.

It also possible that vorticity originating from within the jet nozzle could be turned and amplified by vertical straining in the wake of the transverse jet. This process would be initiated by local tilting and turning of jet shear layer as the jet exits the nozzle and transitions to turbulence. This hypothesis could be tested by reducing or eliminating the boundary layer within the jet nozzle of the transverse jet. The boundary layer could be sucked away in an experiment, or, perhaps, a slip boundary condition could be implemented in a numerical simulation. We believe

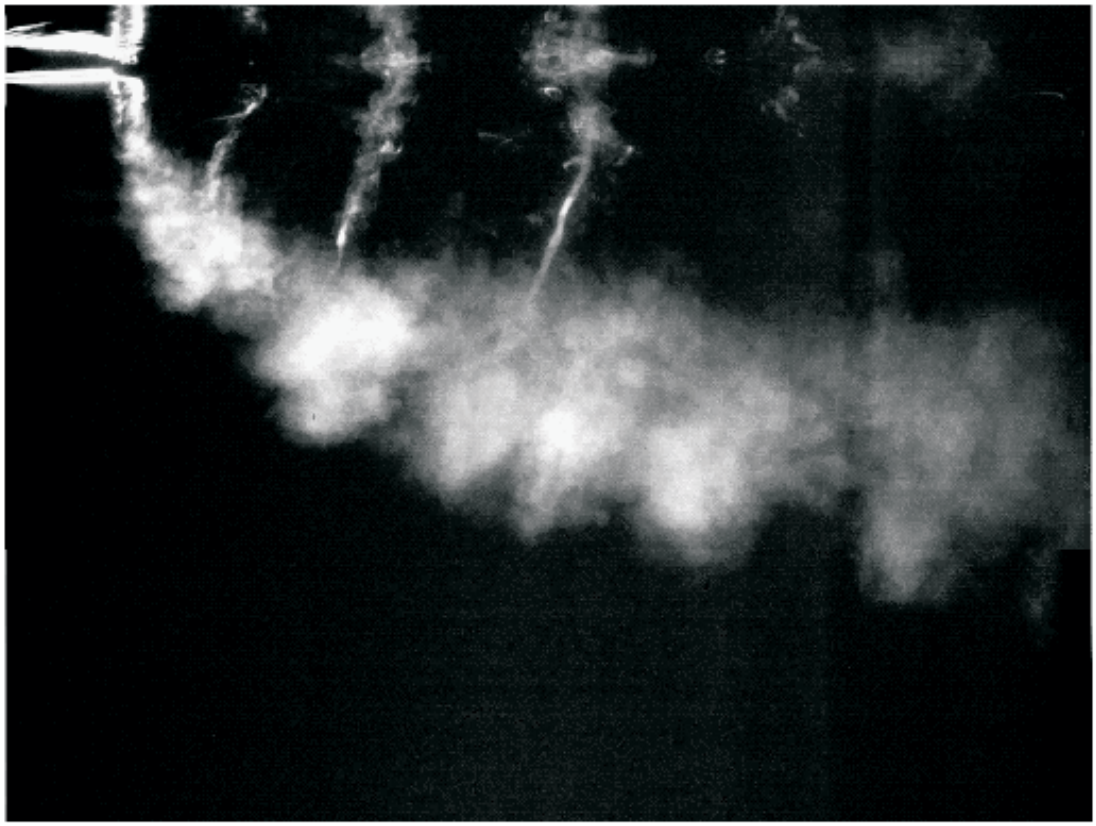

FIG. C.6 Wake vortices for transverse jet injected through free surface. $Re_{\mathrm{j}} = 10 \times 10^3$ and $V_{\mathrm{r}} = 10.1$.

that eliminating the jet-nozzle boundary layer, if that is even possible, is unlikely to eliminate the wake vortices, however.

There appear to be kinematic constraints on the circulation of a jet in crossflow. These constraints are entirely a result of the imposed geometry of the transverse-jet. If this is the case, the circulation would be independent of wall and jet-nozzle boundary layers. LIF visualizations of transverse jets for high velocity ratios suggest that the jet core is initially shielded from the crossflowing freestream. Thus, the velocity in the freestream direction changes from zero inside the jet core to U_∞ outside the jet core. A constant, nonzero circulation $\Gamma \approx U_\infty L$ would be computed along a closed circuit of dimension $L \times \delta$ around one side of the jet (Fig. C.8). The mean vertical vorticity inside that contour would be $< \omega_z > \approx \ U_\infty/\delta$, where δ is the thickness of the jet shear layer.

Similarly, the vertical velocity changes from U_j inside the jet core to zero in the freestream. A circulation of $\Gamma \approx U_\mathrm{j} H$ would be computed for a contour of height H and width δ around the front half of the jet (Fig. C.8). The mean cross-stream vorticity within this contour would be $< \omega_y > \approx \ U_\mathrm{j}/\delta$, where δ is the thickness of the jet shear layer.

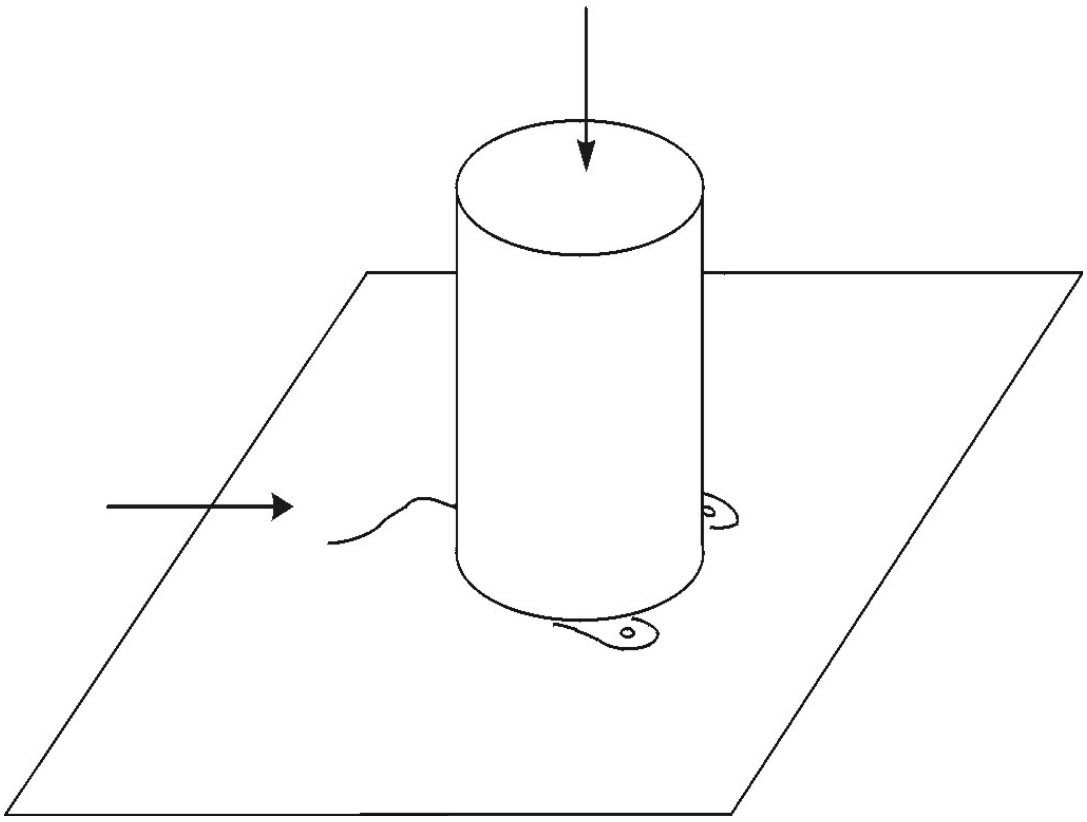

FIG. C.7 Free-surface curvature induced by transverse jet. Jet is injected from above into the free-surface, with freestream flow from left to right. Free surface rises up in a "hill" at the front of the jet, where streamwise velocities go to zero. Two "dimples", or depressions, are formed on opposite downstream sides of the jet core.

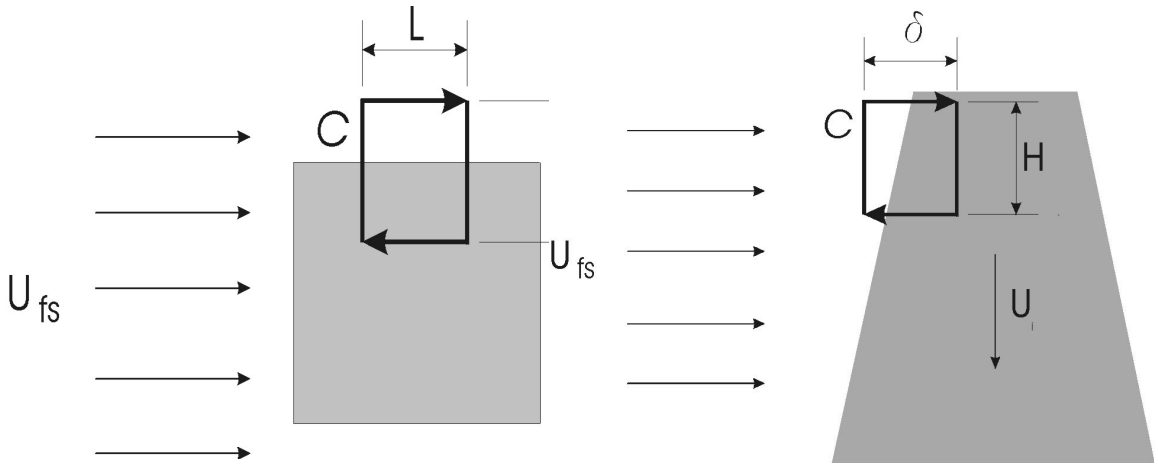

FIG. C.8 Kinematic constraints on circulation at free surface. Jet fluid is shown as shaded areas. Left: Horizontal plane taken at jet exit. Right: Vertical plane taken through jet axis, close to jet exit.

References

Alisse, J. R. & Sidi, C. 2000 Experimental probability density functions of small-scale fluctuations in the stably stratified atmosphere. *J. Fluid Mech.* **402**, 137–162.

Andreopoulos, J. & Rodi, W. 1984 An experimental investigation of jets in a crossflow. *J. Fluid Mech.* **138**, 93–127.

Antonia, R. A., Browne, L. W. B., Britz, D. & Chambers, A. J. 1984 A comparison of properties of temporal and spatial temperature increments in a turbulent plane jet. *Phys. Fluids* **27**(1), 87–93.

Axelrod, D., Koppel, D. E., Schlessinger, J., Elson, E. & Webb, W. W. 1976 Mobility measurement by analysis of fluorescence photobleaching recovery kinetics. *Appl. Phys. Lett* **16**, 1055–1069.

Broadwell, J. E. & Breidenthal, R. E. 1984 Structure and mixing of a transverse jet in incompressible flow. *J. Fluid Mech.* **148**, 405–412.

Catrakis, H. J. & Dimotakis, P. E. 1996 Mixing in turbulent jets: scalar measures and isosurface geometry. *J. Fluid Mech.* **317**, 369–406.

Chassaing, P., George, J., Claria, A. & Sananes, F. 1974 Physical characteristics of subsonic jets in a cross-stream. *J. Fluid Mech.* **62**, 41–64.

Ching, E. S. C. 1991 Probabilities for temperature differences in Rayleigh-Benard convection. *Phys. Rev.* A **44**, 3622–3629.

Cook, A. W. & Dimotakis, P. E. 2000 Transition stages of Rayleigh-Taylor instability between miscible fluids. Submitted to *J. Fluid Mech.* .

Cortelezzi, L. & Karagozian, A. R. 2001 On the formation of the counter-rotating vortex pair. Submitted to *J. Fluid Mech.* .

Cross, M. C. 2000 Notes from Ph161. California Institute of Technology, Pasadena, CA.

Dimotakis, P. E. 1991 Fractals, dimensional analysis and similarity, and turbulence. *Nonlinear Sci. Today* #2/91, pp. 1, 27–31.

Dimotakis, P. E. 2000 The mixing transition in turbulence. *J. Fluid Mech.* **409**, 69–98.

Dimotakis, P. E. & Catrakis, H. J. 1996 Turbulence, fractals, and mixing. NATO Advanced Studies Institute series, *Mixing: Chaos and Turbulence*, GALCIT Report FM97–1.

Drazer, G. & Koplik, J. 2000 Transport properties of self-affine two-dimensional rough fracture. *Bull. Am. Phys. Soc.* **45**.

Eckart, C. 1948 An Analysis of the Stirring and Mixing Processes in Incompressible Fluids. *J. Marine Research* **VII**, 265–275.

Falconer, K. 1990 *Fractal Geometry: Mathematical Foundations and Applications*. Wiley, Chichester, England.

Fearn, R. & Weston, R. P. 1974 Vorticity associated with a jet in a cross flow. *AIAA J.* **12**, 1666–1671.

Fric, T. F. & Roshko, A. 1994 Vortical structure in the wake of a transverse jet. *J. Fluid Mech.* **279**, 1–47.

Goldin, G. M. & Menon, S. 1997 A scalar PDF construction model for turbulent non-premixed combustion. *Combust. Sci. and Technol.* **125**, 47–72.

Gordier, R. L. 1959 Studies on fluid jets discharging normally into moving liquid. St. Anthony Falls Hyd. Lab., University of Minnesota, *Tech. Paper*, no. 28, Series B.

Guilkey, J. E., Kerstein, A. R., McMurtry, P. A. & Klewicki, J. C. 1997 Long-tailed probability distributions in turbulent-pipe-flow mixing. *Phys. Rev.* E, **56**(2), 1753–1758.

Jayesh & Warhaft, Z. 1992 Probability distributions, conditional dissipation, and transport of passive temperature fluctuations in grid-generated turbulence. *Phys. Fluids* **4**(10), 2292–2307.

Kailasnath, P., Sreenivasan, K. R. & Saylor, J. R. 1993 Conditional scalar dissipation rates in turbulent wakes, jets, and boundary layers. *Phys. Fluids* A, **5**(12), 3207–3215.

Kamotani, Y. & Greber, I. 1972 Experiments on a turbulent jet in a cross flow. *AIAA J.* **10**(11), 1425–1429.

Karagozian, A. R. 1986 An analytical model for the vorticity associated with a transverse jet. *AIAA J.* **24**(3), 429–436.

Keffer, J. F. & Baines, W. D. 1963 The round turbulent jet in a cross-wind. *J. Fluid Mech.* , **15**, 481–496.

Kelso, R. M., Lim, T. T. & Perry, A. E. 1996 An experimental study of round jets in cross-flow. *J. Fluid Mech.* **306**, 111–144.

Kelso, R. M. & Smits, A. J. 1995 Horseshoe vortex systems resulting from the interaction between a laminar boundary layer and a transverse jet. *Phys. Fluids* **7**(1), 153–158.

Kuznetsov, V. R. & Sabel'nikov, V. A. 1990 *Turbulence and Combustion*. Hemisphere Publishing, New York.

Kuzo, D. M. 1995 *An Experimental Study of the Turbulent Transverse Jet*. Ph.D. Thesis, California Institute of Technology, Pasadena, CA.

Kuzo, D. M. & Roshko, A. 1984 Observations on the wake region of the transverse jet. *Bull. Am. Phys. Soc.* **29**, 1536.

Leonard, A. & Hornung, H. 2001 Personal communication. California Institute of Technology, Pasadena, CA.

Longuet-Higgins, M. S. 1992 Capillary rollers and bores. *J. Fluid Mech.* **240**, 659–679.

Lugt, H. J. 1987 Local flow properties at a viscous free surface. *Phys. Fluids* **30**(12), 3647-3652.

Lundgren, T. 1989 *A free surface vortex method with weak viscous effects*. In *Mathematical Aspects of Vortex Dynamics*, 68–79.

Lundgren, T. & Koumoutsakos, P. 1999 On the generation of vorticity at a free surface. *J. Fluid Mech.* **382**, 351–366.

Mandelbrot, B. B. 1975 On the geometry of homogeneous turbulence, with stress on the fractal dimension of the iso-surfaces of scalars. *J. Fluid Mech.* **72**, 401–416.

Mandelbrot, B. B. 1975 *Les objets fractals: forme, hasard et dimension*. Flammarion, Paris.

Margason, R. J. 1993 Fifty Years of Jet in Cross Flow Research. AGARD Meeting on Computational and Experimental Assessment of Jets in Cross Flow, April, 1993.

Mathur, T., Billig, F., Streby, G., Gruber, M., Jackson, K., Donbar, J., Donaldson, W., Jackson, T. & Smith, C. 1999 Supersonic combustion experiments with a cavity-based fuel injector. 35^{th} *AIAA/ASME/SAE/ASEE Joint Propulsion Conference and Exhibit* (20–24 June 1999, Los Angeles, California).

McAllister, J. D. 1968 *A momentum theory for the effects of cross flow on incompressible jets*. Ph.D. thesis, University of Tennessee.

McMahon, H. M., Hester, D. D. & Palfery, J. G. 1971 Vortex Shedding from a Turbulent Jet in a Cross-Wind. *J. Fluid Mech.* **48**, 73–80.

Miller, P. L. & Dimotakis, P. E. 1991 Stochastic geometric properties of scalar interfaces in turbulent jets. *Phys. Fluids A* **3**, 168–177.

Morton, B. R. & Ibbetson, A. 1996 Jets Deflected in a Crossflow. *Exp. Thermal and Fluid Sc.* **12**, 112–133.

Moussam Z. M., Trischka, J. W. & Eskinazi, S. 1977 The near field in the mixing of a round jet with a cross-stream. *J. Fluid Mech.* **80**, 49–80.

Mydlarski, L. & Warhaft, Z. 1998 Three-point statistics and the anisotropy of a turbulent passive scalar. *Phys. Fluids* **10**(11), 2885–2894.

Niederhaus, C. E., Champagne, F. H. & Jacobs, J. W. 1997 Scalar Transport in a Swirling Transverse Jet. *AIAA J.* **35**, 1697–1704.

Ould-Rouis, M., Anselmet, F., Le Gal, P. & Vaienti, S. 1995 Statistics of temperature increments in fully developed turbulence Part II. Experiments. *Physica* D **85**, 405–424.

Peitgen, H.-O., Jurgens, H. & Saupe, D. 1993 *Fractals for the Classroom*. Springer-Verlag.

Pfeifer, P., Wu, Y. J., Cole, M. W. & Krim, J. 1989 Multilayer adsorption on a fractally rough surface. *Phys. Rev. Lett*. **62**, 1997–2000.

Pope, S. B. 1985 PDF Methods for Turbulent Reactive Flows. *Prog. Energy Comb. Sc.* **11**, 119–192.

Pratte, B. D. & Baines, M. 1967 Profiles of the round turbulent jet in a crossflow. *J. Hydronaut. Div. ASCE* **92**, 53–64 .

Pringsheim, P. 1949 *Fluorescence and phosphorescence*. Interscience Publishers, Inc.

Reilly, R. S. 1968 *Investigation of the deformation and penetration of a turbulent subsonic jet issuing transversely into a uniform, subsonic main stream*. Ph.D. thesis, University of Maryland.

Richardson, L. F. 1961 The problem of contiguity: an appendix of statistics of deadly quarrels. *General Systems Yearbook* **6**, 139–187.

Sarpkaya, T. 1999 Vorticity, free surface, and surfactants. *Ann. Rev. Fluid Mech.* **28**, 83–128.

Shraiman, B. & Siggia, E. 2000 Scalar turbulence. *Nature* **405**, 639–646.

Smith, S. H. & Mungal, M. G. 1998 Mixing, structure and scaling of the jet in crossflow. *J. Fluid Mech.* **357**, 83–122.

Sreenivasan, K. R. 1991 On local isotropy of passive scalars in turbulent shear flows. *Proc. Roy. Soc. London* A **434**, 165–182.

Takayasu, H. 1982 Differential Fractal Dimension of Random Walk and Its Applications to Physical Systems. *J. Phys. Soc. Japan* **51**, 3057–3064.

Tennekes, H. & Lumley, J. L. 1972 *A First Course in Turbulence*. MIT Press.

Tong, C. & Warhaft, Z. 1994 On passive scalar derivative statistics in grid turbulence. *Phys. Fluids* **6**(6), 2165–2176.

Vicsek, T., Cserzo, M. & Horvath, V. K. 1990 Self-affine growth of bacterial colonies. *Physica* A **167**, 315–321.

Walker, D. A. 1987 A fluorescence technique for measurement of concentration in mixing liquids. *J. Psys. E.: Sci. Instrum.* **20**, 217–224.

Wu, J.-Z. 1995 A theory of three-dimensional interfacial vorticity dynamics. *Phys. Fluids* **7**, 2375–2395.

Yuan, L. L., Street, R. L. & Ferziger, J. H. 1999 Large-eddy simulations of a round jet in crossflow. *J. Fluid Mech.* **379**, 71–104.